eXPRESS Polymer Letters Vol.5, No.6 (2011) 479
Available online at www.expresspolymlett.com
DOI: 10.3144/expresspolymlett.2011.46

Editorial corner – a personal view
From bulk to nano-sized polymers with controlled nano-morphology

S. Fakirov[*]

Centre for Advanced Composite Materials (CACM) at the Department of Mechanical Engineering of The University of Auckland, Auckland, Private Bag 92019, New Zealand

There are enough evidences nowadays for the failure of the concept of nanocomposites – the expectations for drastic improvement of mechanical properties using extremely low filler concentrations (around 1%) were not realized. To the main reasons for this situation belong: poor dispersion, poor interfacial load transfer, process-related deficiencies, poor alignment, poor load transfer to the interior of filler bundles, the fractal nature of filler clusters.

Due to a generic property of nano-sized materials they agglomerate strongly, and the problem of poor dispersion seems to be practically non-soluble. For this reason it was suggested to convert polymers themselves into nano-sized materials, instead of blending them with nano-fillers. This idea seems to be realistic having in mind the characteristic features of polymers as materials: (i) a large and flexible variety of processing techniques (in melt, in solution, during polymerization), (ii) they can be blended with other polymer(s), (iii) due to presence of variety of functional groups they are capable to establish chemical bonds of different strength (covalent, hydrogen bonding, ionic), (iv) due to the chain character of macromolecules it is possible to realize different spatial conformations resulting in different properties. This set of 'tools' can be used for modification of polymers towards creation materials with new or improved properties instead of a simple blending.

After converting the bulk polymer into nanofibrils there are many opportunities for their further application: (i) as nanofibrillar polymer-polymer composites (via compression molding of the drawn blend before removing the second polymer), and after removing of the second blend component, (ii) using the neat nanofibrils as starting material for nanofibrillar single polymer composites, (iii) or as materials for biomedical applications (scaffolds in the regenerative medicine, or carriers for controlled drug delivery), particularly if the second polymer is water soluble, (iv) as well as for technical purposes (as nanofilters or electroconductive nanowires), a.o.

Recent findings demonstrated that the final nanomorphology can be controlled via *hydrogen bonding* between the blend partners: individual, not mutually connected 'endless' nanofibrils in case of no H-bonding, or a 3-D nanofibrillar nanoporous network if H-bonding is possible.

What the science and technology of polymer nanocomposites concerns, the new results allows us to formulate and realize the *concept of converting instead of adding*.

Prof. Dr. Stoyko Fakirov
Member of International Advisory Board

[*]Corresponding author, e-mail: s.fakirov@auckland.ac.nz

eXPRESS Polymer Letters Vol.5, No.6 (2011) 480–492
Available online at www.expresspolymlett.com
DOI: 10.3144/expresspolymlett.2011.47

Thermal properties, curing characteristics and water absorption of soybean oil-based thermoset

*S. G. Tan, W. S. Chow**

School of Materials and Mineral Resources Engineering, Engineering Campus, Universiti Sains Malaysia, Nibong Tebal 14300 Penang, Malaysia

Received 20 October 2010; accepted in revised form 10 December 2010

Abstract. Epoxidized soybean oil (ESO) was successfully thermal-cured by using methylhexahydrophthalic anhydride (MHHPA) curing agent, in the presence of tetraethylammonium bromide (TEAB) catalyst of varied concentration (0.3–0.8 phr). The polyesterification process of ESO thermoset was proven and supported by Fourier transforms infrared spectroscopy (FTIR) and gas chromatography-mass spectroscopy analysis (GC-MS). A possible chemical reaction of the MHHPA, TEAB and ESO was proposed based on the experimental work. Differential scanning calorimetry (DSC) and dynamic mechanical analysis (DMA) revealed that there is a positive relationship between the degree of conversion and crosslink density of ESO thermoset with TEAB concentration. The kinetics of water absorption of the ESO thermoset were found to conform to Fickian law behavior.

Keywords: *biopolymers, epoxidized soybean oil, thermosetting resin, thermal properties, water absorption*

1. Introduction

Traditionally, epoxidized vegetable oils (EVO) are used as poly(vinyl chloride) plasticizers, stabilizers and lubricants. Recently, modified vegetable oils could be used to synthesize segmented polyurethane [1], thermoplastic polyurethanes [2], poly (methyl methacrylate)-multigraft copolymers [3], novel thermosets and rubbers [4–5] and 'green' composites [6]. In recent years, there has been substantial growth in biopolymers from EVO. These EVO from biological origin substrates could bring along numerous advantages and new beneficial properties, which may not be able to gain from petroleum-based epoxy resins. For example, EVO have been evaluated as ecological and environmental friendly alternative for petroleum-based epoxy resins since they are neutral in the carbon dioxide cycle and are readily biodegradable. Other advantages of the EVO include cost effectiveness, renewability and availability.

In general, epoxidized soybean oil (ESO) is a triglyceride made up of a complex multi-component mixture of functionalized oleic, linoleic and linolenic acid methyl esters as well as saturated fatty acids (i.e. palmitic and stearic acids). It has been recognized in the literature that these functionalized fatty acids in ESO could be thermally cured with a thermal latent initiator [7], thermally cured with acid anhydride under the catalytic reaction of tertiary amines catalyst [8] and ultraviolet (UV) cured in the presence of photo-initiators [9]. However, saturated fatty acids in ESO do not take part in the polymer network formation. This is due to the fact that they do not possess any epoxy functional groups in their saturated backbone structures.

Specifically, in the open literature, there exist numerous models to explain the curing mechanisms for

*Corresponding author, e-mail: chowwenshyang@yahoo.com

ESO. Jin and Park [7] proposed thermally induced ring opening polymerization route for ESO thermoset initiated by N-benzylquinoxalinium hexafluoroantimonate thermal latent initiator. Ortiz *et al.* [9] reported that radical induced cationic photopolymerization of ESO thermoset in the presence of diarylinodonium salt photo-initiator follows conventional cationic polymerization mechanism and chain reaction mechanism. Gao [10] proposed that the curing mechanism of catalytic ESO-anhydride thermosets involves reaction of the tertiary amine with ESO monomer followed by the ring opening of the anhydride functional group with the alkoxide.

Although the EVO based thermosetting materials are more environmental friendly, they tend to suffer from shortcomings in terms of long curing schedule, high curing temperature, poor thermo-physical properties and high degree of water uptake. In order to overcome some of these limitations, our work aims to chemically synthesize a thermally curable ESO thermosetting resin in the presence of the tetraethylammonium bromide (TEAB) catalyst. It is hypothesized that the TEAB-catalyzed ESO thermosetting resin can be prepared using shorter curing schedules and lower curing temperature due to the fast cure rate of the TEAB catalyst. Accordingly, the primary objective of this present study is to investigate the effect of TEAB catalyst concentration on the curing characteristics, thermal properties and kinetics of water absorption of ESO thermoset. A plausible curing mechanism of the thermal curable ESO thermoset under the catalytic reaction of TEAB catalyst will also be proposed.

2. Experimental

2.1. Materials

Epoxidized soybean oil (ESO; trade name Mingchen ESO-1) resin with 6.1 wt% epoxy oxirane content and molecular weight of about 950 g/mol was purchased from Shangdong Longkou Longda Chemical Industry Co., Ltd., China. Industrial grade methylhexahydropthalic anhydride (MHHPA) curing agent was purchased from CAPE Technology Sdn. Bhd., Malaysia. Tetraethylammonium bromide (TEAB: code T7012) catalyst was supplied by Sigma-Aldrich, Malaysia. The materials designation and composition of the ESO thermoset were summarized in Table 1.

Table 1. Materials designation and composition of ESO thermoset

Materials designation	Concentration of TEAB catalyst [phr]
ES_0.3A	0.3
ES_0.4A	0.4
ES_0.5A	0.5
ES_0.6A	0.6
ES_0.7A	0.7
ES_0.8A	0.8

2.2. Preparation of thermal curable ESO thermoset

MHHPA curing agent was pre-mixed with TEAB catalyst at a predetermined ratio. ESO resin and MHHPA/TEAB mixture were then mixed at room temperature and stirred mechanically. The mixture was then poured into the cavities of mould and subjected to thermal curing process in an oven at 140°C for 3 hours. The dimension of the mould used to prepare the ESO thermoset is 300 mm × 100 mm × 3 mm (length × width × thickness).

2.3. Curing characteristics of ESO thermoset

The curing characteristics of the TEAB-catalyzed ESO thermoset were characterized using Fourier transform infrared spectroscopy (Spectrum 100 FTIR, Perkin Elmer, USA), gas chromatography-mass spectroscopy (GC-MS, Perkin Elmer Clarus 600T, USA), DSC Diamond Analyzer (Perkin Elmer, USA) and DMA 8000 (Perkin Elmer, USA).

The curing characteristics of ESO thermoset which thermally cured for 1, 2 and 3 hours were determined with FTIR. The FTIR spectra of the thermal curable ESO thermoset from the wavelength of 4000 to 550 cm^{-1} were recorded as the infrared radiation transmitted through the sample. The carbonyl index (*C.I.*) values of the samples were calculated based on the ratio of absorbance (*A*) at two different wave-numbers as shown in Equation (1):

$$C.I. = \frac{A_{1700}}{A_{1456}} \tag{1}$$

where A_{1700} represents the absorbance band at 1700 cm^{-1} due to the presence of carbonyl stretch of the aromatic acid whereas A_{1456} represents the band at 1456 cm^{-1} corresponding to the absorbance from the presence of methyl group in MHHPA curing agent, which is taken as a reference band.

The pure ESO and extracted molecular fragments of the ESO thermoset were analyzed by gas chro-

matography mass spectroscopy (GC-MS). One μl injection volume using splitless mode was performed on capillary column (30 m × 250 μm) with helium flows at constant pressure. The initial temperature, injection temperature and transfer temperature of the GC-MS test were set at 65, 250 and 180°C, respectively. The holding time was set for 10 minutes at a ramp rate of 8°C/min. The molecular fragments of the ESO were determined using TurboMass™ software.

The degree of conversion of ESO thermoset was determined using DSC and calculated based on Equation (2). The crosslink density (v_c) and molecular weight between cross-linking (M_c) of the ESO thermoset were determined using DMA and calculated based on Equations (3) and (4) respectively [11–12]:

$$\alpha = \frac{\Delta H_c - \Delta H_r}{\Delta H_c} \tag{2}$$

$$v_c = \frac{E'}{3RT} \tag{3}$$

$$M_c = \frac{d}{v_c} \tag{4}$$

where α is the degree of conversion, ΔH_c is the total exothermic heat generated for a fully cured system and ΔH_r is the total residual exothermic heat generated during a specified period of time. v_c is the crosslink density for the epoxy network, E' is the storage modulus of the thermoset in the rubbery plateau region at T_g + 40°C, R is the gas constant, T is the absolute temperature, d is the density (1.1 g/cm^3) and M_c is the molecular weight between crosslink.

2.4. Thermal characterization of ESO thermoset

The curing profile of ESO thermoset was examined using DSC Diamond Analyzer (Perkin Elmer, USA). Approximately 20 mg of the sample was placed into the DSC aluminium pans, followed by thermal scanning from 30 to 300°C at a heating rate of 10°C/min, in nitrogen gas atmosphere. The onset curing temperature (T_{onset}), the temperature where maximum cross-linking reaction takes place (T_{peak}) and the total heat released during curing reaction (ΔH) of ESO thermoset were determined. The dynamic mechanical properties of ESO thermoset were determined using DMA 8000 (Perkin Elmer, USA). The specimen with the dimension of 25 mm × 10 mm × 2 mm was heated from –100 to 200°C at a heating rate of 2°C/min in nitrogen atmosphere. Specimen held in a single cantilever mode was fixed at one end and the other end was vibrated by the bending stress at the frequency of 1 Hz with the displacement of 0.05 mm. The glass transition temperature (T_g), storage modulus (E') and damping properties (tanδ) of ESO thermoset were examined with DMA. The thermal stability of ESO thermoset was characterized using TGA Pyris 6 (Perkin Elmer, USA). Approximately 5 mg of the specimen was heated from room temperature to 600°C at a heating rate of 10°C/min under nitrogen gas atmosphere.

2.5. Water absorption of ESO thermoset

Water absorption test according to the ASTM D570 was conducted on ESO thermoset by immersing the specimens in distilled water at room temperature for three months. The weight gained of the ESO thermoset at any time t, M_t as a result of water absorption was determined using Equation (5). The water diffusion coefficient (D) of ESO thermoset was determined using Equation (6) [13]:

$$M_t = \frac{W_w - W_d}{W_d} \cdot 100 \tag{5}$$

$$\frac{M_t}{M_m} = 1 - \frac{8}{\pi^2}\exp\left[- \frac{Dt}{h^2}\pi^2 \right] \tag{6}$$

where W_d and W_w represent the material dry weight and weight of materials after being exposed to the water absorption at a period of time t respectively. M_m is the percentage equilibrium or the maximum water absorption of ESO thermoset, t is the time taken for the ESO thermoset to reach the saturated stage, and h is the thickness of the ESO specimen.

3. Results and discussion

3.1. Curing characteristics of ESO thermoset

3.1.1. FTIR characterization

Figure 1 shows the FTIR spectra of TEAB catalyst, MHHPA curing agent and the mixture of MHHPA/TEAB. One may observe that FTIR spectrum of the MHHPA/TEAB mixture consists of a new 1700 cm^{-1} shoulder peak. The appearance of this peak is associated to the carbonyl stretch (C=O) of the aromatic acid, which indicates the asymmetric cleavage of

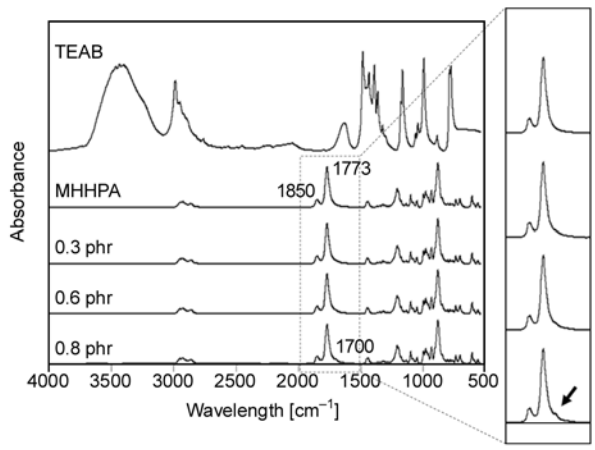

Figure 1. FTIR spectra representing the ring opening of MHHPA with TEAB (Note: Arrow shows the 1700 cm^{-1} shoulder peak)

the MHHPA functional group by TEAB catalyst to form the zwitterions. The amount of carbonyl groups present and the extent of MHHPA ring opening are estimated based on the carbonyl index value obtained from the FTIR study (c.f. Table 2). It is proposed that the ring opening of MHHPA curing agent by the TEAB catalyst involves S_N2 reaction. The triethylamine formed as a result of the dequaternization reaction of TEAB catalyst, serves as a nucleophile and attacks the MHHPA curing agent to yield zwitterions. Although the exact absorbance band representing the zwitterions is undetected from FTIR spectra, the intensity reduction of the infrared absorbance bands that appear at 1856, 1775 and 887 cm^{-1} in the FTIR spectra is a good indicator to support the phenomenon of MHHPA ring opening by the TEAB catalyst. This is due to the fact that these absorbance bands are the characteristic bands for the conjugated cyclic anhydride which could be assigned to the C=O and C–O stretches. Considering these phenomena, a plausible assumption that the zwitterions are generated during the pre-mixed reaction could be made.

Table 2. Curing characteristics of TEAB-catalyzed ESO thermoset

Characteristics			ES_0.3A	ES_0.6A	ES_0.8A
Carbonyl index[a]	MHHPA/TEAB mixture		0.62	0.64	0.79
	Curing	1 h	1.03	1.69	1.68
		2 h	2.39	2.96	3.55
		3 h	2.96	3.79	3.95
Degree of conversion[b] [%]			95.6	98.6	99.8
Crosslink density[c] [10^{-3} mol/cm^3]			0.215	0.260	0.446
M_c[c] [g/mol]			5116	4230	2471

[a]calculated from FTIR analysis
[b]calculated from DSC analysis
[c]calculated from DMA analysis

It is noticed that the intensity of the 1700 cm^{-1} shoulder peak increases with increasing the TEAB catalyst concentration in MHHPA/TEAB mixture. This incident could be evidenced by the increment in the carbonyl index calculated as reported in Table 2. While, the absorbance assignable to the C=O and C–O stretches of MHHPA curing agent show a decreasing trend. These findings suggest the increased anhydride ring opening reaction between the TEAB catalyst and MHHPA curing agent as the TEAB catalyst concentration increases from 0.3 to 0.8 phr. This may be due to the increased potential of TEAB catalyst to facilitate the MHHPA ring opening forming more zwitterions species at higher TEAB concentration. However, it is noted that only low conversion of zwitterions is achieved during the pre-mixed reaction. The lower efficiency of the TEAB catalyst to cleavage the anhydride ring during pre-mix reaction is strongly believed to be attributed to the relatively stable and low reactivity of these quaternary ammonium salts. It is also experimentally determined in this study that no MHHPA ring opening is detected at low level of TEAB concentration (< 0.3 phr).

During the heating reaction of ESO/MHHPA/TEAB mixture at 140°C in the oven, the zwitterions formed would eventually react with the epoxy rings on the ESO backbone chains and subsequently generate the alkoxide intermediates. The alkoxide intermediates would then cleave another MHHPA curing agent to yield carboxylate anions during the propagation stage. These carboxylate anions would chemically react with another ESO resins to yield the reaction intermediates product and propagate the cycles. The polyesterification reaction in ESO/MHHPA/TEAB mixture is completed after 3 hours of curing reaction. This evidently results in the formation of ESO thermoset with 3-dimensional polyester-type of linkages. To support the curing transformations proposed, the curing characteristics of ESO thermoset at three different curing times (i.e. 1, 2 and 3 hours) were evaluated using FTIR study as shown in Figure 2.

As observed in Figure 2, the intensities of absorbance bands corresponding to the C–O and C=O stretches of MHHPA curing agent show a progressive decrease as a function of curing reaction time for the ESO/

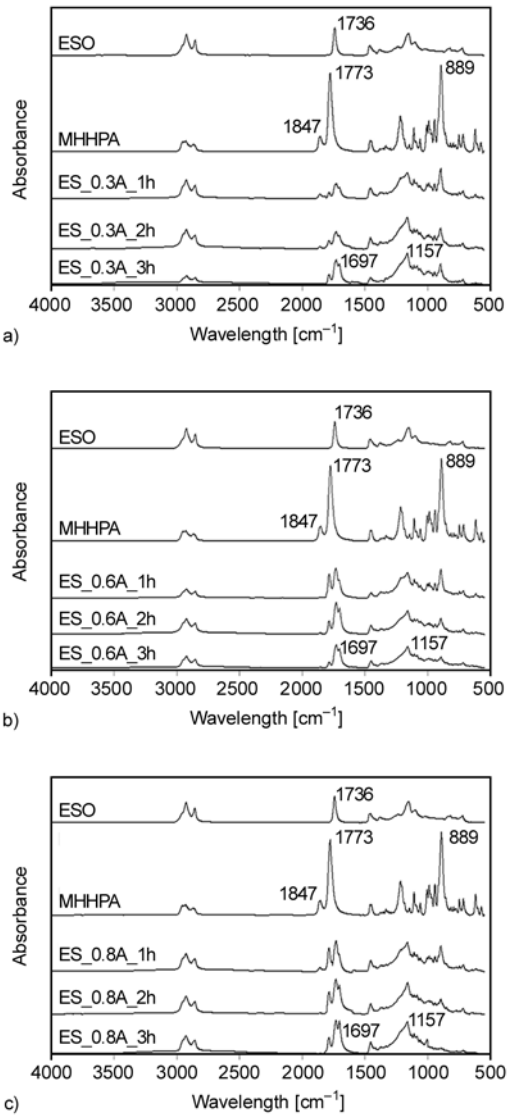

Figure 2. (a) FTIR spectra representing the curing characteristics of ES_0.3A thermoset, (b) FTIR spectra representing the curing characteristics of ES_0.6A thermoset, (c) FTIR spectra representing the curing characteristics of ES_0.8A thermoset

MHHPA/TEAB mixture. Additionally, it is clearly noticeable that the stretching vibrations of the C–O–C and C–C–O functional groups in MHHPA curing agent which in the range of 1300–1100 cm^{-1} disappear gradually with curing time. The reduction in intensities of these absorbance bands suggest the ring opening reaction of MHHPA curing agent and the polyesterification reaction of MHHPA curing agent with alkoxide. Furthermore, it is discovered that the absorbance bands at 1695 and 1161 cm^{-1} which corresponding to the C=O and O–C–C vibrations of ester groups increasingly emerge with curing time. This finding further signifies that the polyesterification process has taken place in the ESO/MHHPA/TEAB mixture as these absorbance bands are the representative bands for esters. Chemical reactions of epoxy groups in ESO with carboxylate anions followed by reacting with anhydrides during the propagation cycle give rise to the formation of polyester-type linkages between ESO and MHHPA curing agents. The polyesterification reaction of ESO/MHHPA/TEAB mixture forming the polyester-type of linkages is also verified with the aid of gas chromatography-mass spectroscopy analysis (c.f. Figure 3).

From Figure 2, it is noted that the peaks which are corresponding to epoxy groups in ESO disappeared and are substituted by the peaks assignable to C=O and C–O functional groups of the conjugated cyclic anhydride and the C=O and O–C–C of the ester groups after curing process for 3 hours. As shown in Figure 3, it is noted that the peak (i.e. 7.63 min) corresponding to the epoxy group in ESO resin disappear after being thermally cured for 3 hours. However, the peaks (i.e. 15.81 and 20.82 min) corresponding to the ester functional groups are detected in the cured ESO thermoset. Furthermore, the peak (i.e. 16.18 min) representing the molecular fragments of MHHPA curing agent with ring-opened structures are also being detected in thermally cured ESO thermoset. One possible explanation to these findings could be linked to the polyesterification process of ESO/MHHPA/TEAB. Based on the information obtained from the FTIR spectra and GC-MS, the curing mechanism of ESO thermoset is proposed. Figure 4 shows the proposed mechanism for the thermally cured ESO thermoset.

Furthermore, as shown in Figure 2, it is determined that the polyesterification reaction of the ESO/MHHPA/TEAB mixture proceeds at relatively fast manner at the beginning stage during thermal curing compared to that of at the pre-mix stage. This is owing to the fact that TEAB catalyst tends to experience the chemical reaction of dequaternization at the temperature range of 100–200°C to generate trialkylamine. The tertiary amines formed during the internal displacement reaction will eventually boost the polyesterification rate of ESO/MHHPA/TEAB mixture. However, it is determined that the polyesterification reaction of the mixture proceeds at relatively slow manner after 2 hours of thermal curing. This event occurs as the overall catalytic reac-

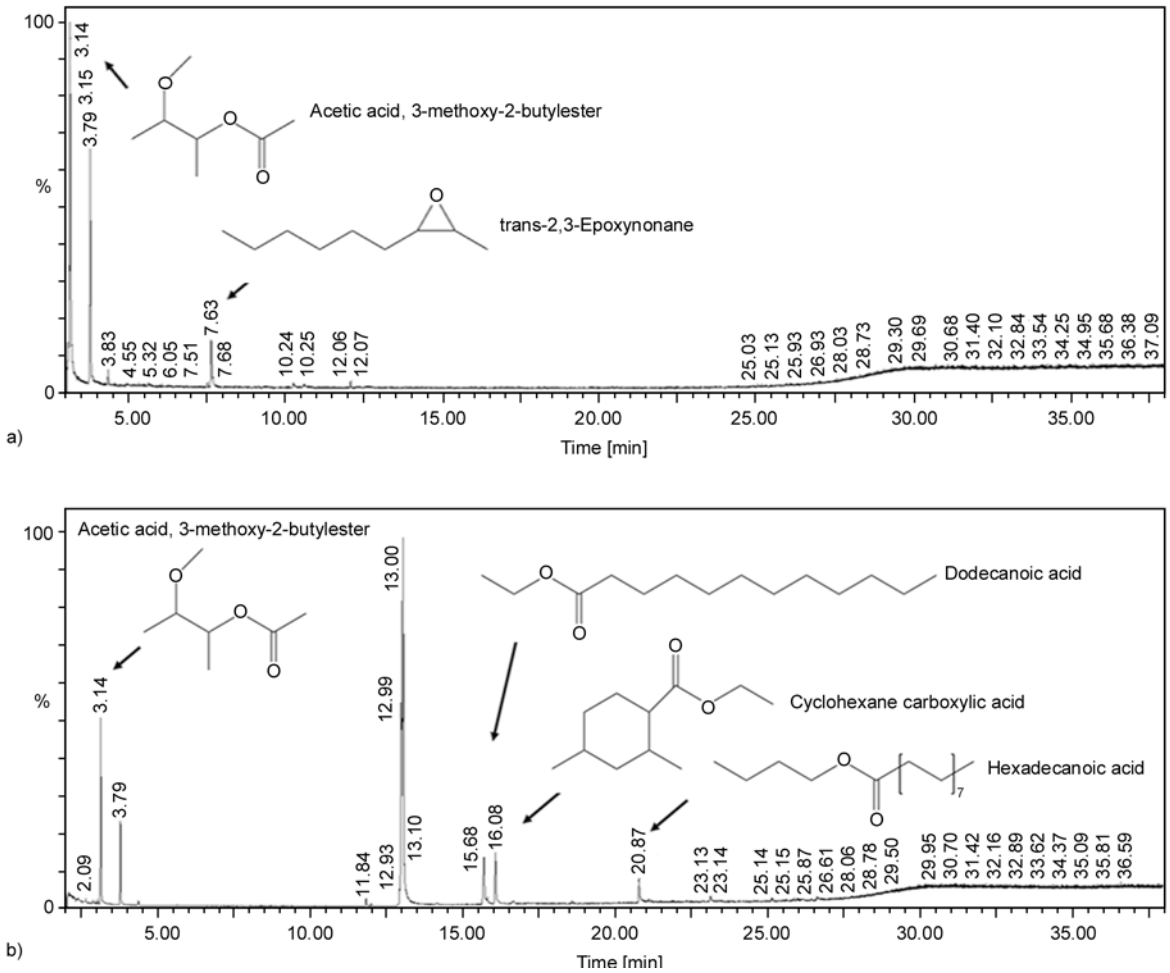

Figure 3. (a) GC-MS chromatogram of ESO, (b) GC-MS chromatogram of ES_0.6A thermoset

tion in the mixture begins to change from kinetic to diffusion-controlled. The curing process in bisphenol-S epoxy resin/phthalic anhydride epoxy system changing from kinetically controlled to diffusion controlled was also reported by Li *et al.* [14].

Apart from that, the effects of the TEAB concentration on the ESO thermoset are also being displayed in Figure 2. An intensity reduction in representative bands for the MHHPA curing agent and an increment in absorbance bands intensities for esters are observed when increasing the TEAB concentration from 0.3 to 0.8 phr. These results indicate the polyesterification rate is higher in thermally cured ESO containing higher TEAB concentration. Lower levels of TEAB concentration (<0.3 phr) are also studied in this work, perhaps even a 0-level catalyst experiment. However, it is found that the polyesterification reactions of the ESO mixture are highly unfavourable. The mixture is unable to be thermally cured at low level of TEAB concentration. One possible explanation could be linked to the very limited or even no chemical reaction between the ESO resin and MHHPA curing agent without the presence of a catalyst.

3.1.2. DSC characterization

The DSC heating thermograms showing the non-isothermal curing profiles of TEAB-catalyzed ESO thermoset are demonstrated in Figure 5. An exothermic peak representing the epoxy curing reactions is detected on the DSC heating curves. The enthalpy of ESO/MHHPA/TEAB polymerization can be examined by integrating the exothermic peak. It is experimentally proven that the ESO thermoset catalyzed with higher TEAB catalyst concentration shows higher ΔH value. The differences in the ΔH values obtained are mainly due to the different extent of conversion of the liquid ESO monomers to ESO thermosets during the thermal heating process in DSC. These findings show that the higher the TEAB concentration, the greater the extent of conversion in ESO thermoset, and the higher the cross-

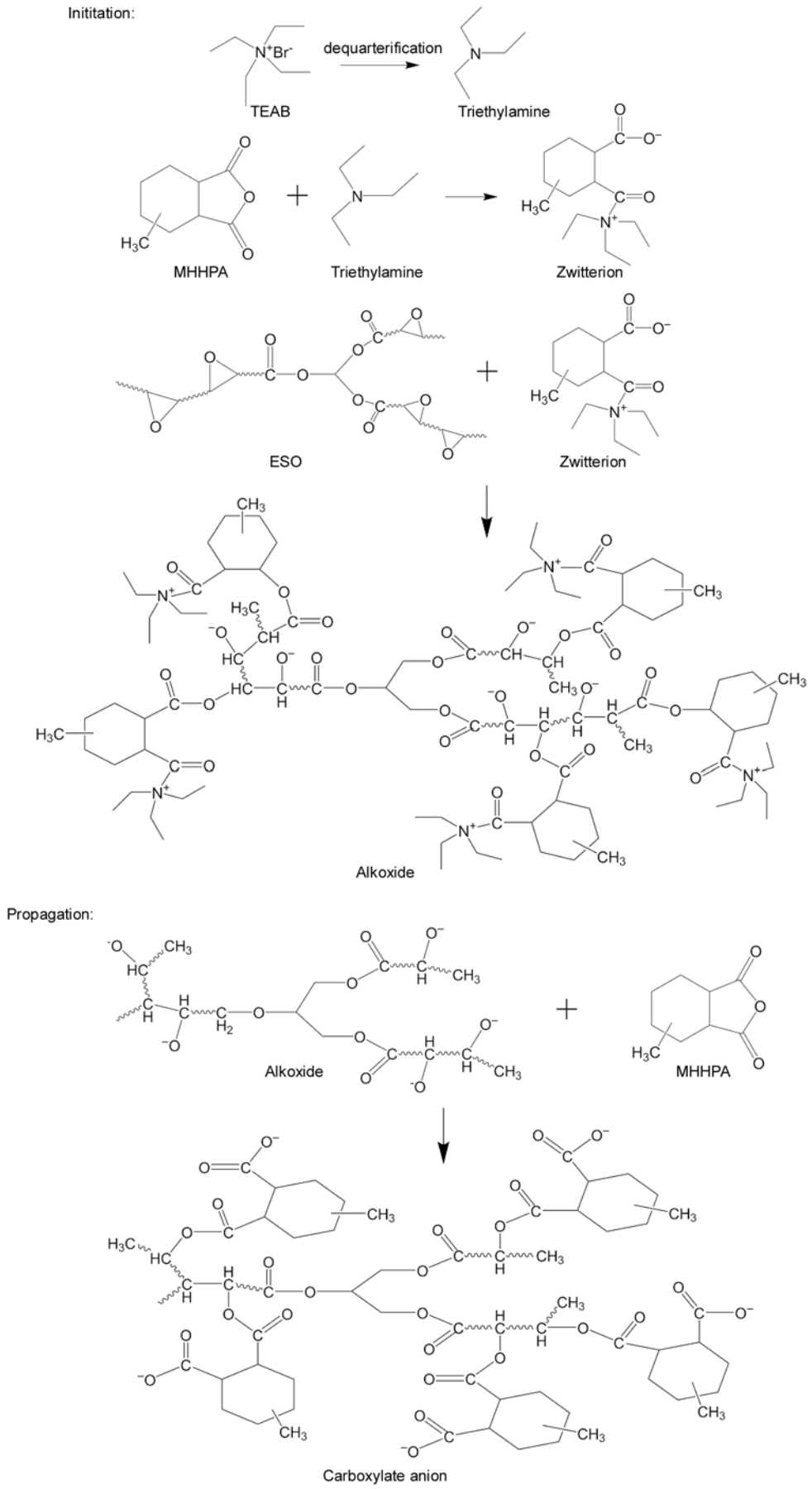

Figure 4. Curing mechanism of TEAB-catalyzed ESO thermoset

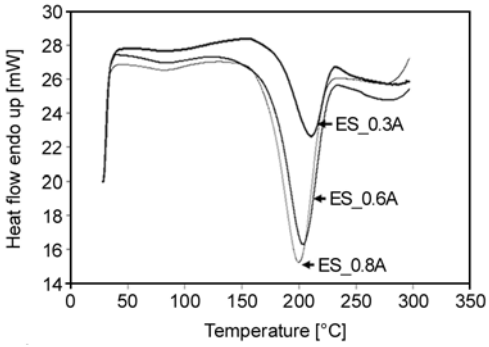

Figure 5. DSC heating thermograms of TEAB-catalyzed ESO thermoset

Table 3. Thermal properties of TEAB-catalyzed ESO thermoset

Thermal characteristics	ESO thermosetting resins		
	ES_0.3A	ES_0.6A	ES_0.8A
T_{onset}[a] [°C]	183.0	162.1	150.7
T_{peak}[a] [°C]	211.9	203.8	200.8
T_{o1}[b] [°C]	200.0	206.0	210.0
T_{o2}[b] [°C]	351.0	342.0	347.0
T_d[b] [°C]	458.0	454.0	456.0
T_g[c] [°C]	53.0	59.0	69.8

[a]detected from DSC
[b]detected from TGA
[c]detected from DMA

linking formation seems to be. One possible explanation is that the higher conversion of zwitterions is achieved during the pre-mix reaction to initiate the thermal curing reaction of ESO thermoset catalyzed with higher TEAB concentration.

From the DSC thermograms, second exotherm peak or shoulder after the T_{peak} is not observable. This may give us a hint that homo-polymerizations of ESO resin do not take place. According to Boquillon and Fringant [12] who studied on the thermal curing of epoxidized linseed oil under the influence of different catalysts and anhydride hardeners, second shoulder exotherm peak after the main exotherm peak appearing at lower temperature could be associated to the epoxy homo-polymerization. Therefore, it can be concluded that ESO/MHHPA polymerization is the only chemical reaction occurs during polyesterification process and the crosslinked ESO thermoset does not contain any epoxy homopolymer. This finding is also consistent with the curing mechanism proposed (cf. Figure 4) in which the ESO resin will chemically react with the MHHPA curing agent in the presence of TEAB catalyst forming 3-dimensional polyester linkages instead of forming polyether linkages among ESO resins. It is also noticed that the T_{onset} and T_{peak} (c.f. Table 3) of the ESO thermoset shift to lower temperature as the TEAB concentration is increased from 0.3 to 0.8 phr. The shifts of DSC heating thermograms to lower temperature are presumably due to the increase in the crosslinking reaction rate. There was a direct relationship between initial curing reaction rate and catalyst concentration of a catalyzed reaction [12]. This is consistent with the finding by Liu *et al.* [15] which stated that the increase in catalyst concentration in epoxy-phenol/montmorillonite nanocomposites will shift T_{onset} and T_{peak} to lower temperature.

Also, as shown in Figure 5, ESO thermoset undergoes the enthalpy relaxation phenomenon at relatively low TEAB concentration. The extent reduces progressively as the TEAB catalyst concentration increases from 0.3 to 0.8 phr. The reduction of this enthalpy relaxation phenomenon is believed to be due to the increase in crosslink density resulting from an increase in the extent of ESO conversion in ESO thermoset. Shin and coworkers [16, 17] also reported that the restriction of enthalpy relaxation can be directly related to an increase in crosslink density and activation energy for the enthalpy relaxation.

The influence of TEAB concentration on the degree of conversion (α) of ESO thermoset is summarized in Table 2. The degree of conversion increases about 4.2% when the TEAB concentration is increased from 0.3 to 0.8 phr. This result indicates that the efficiency of TEAB to facilitate the ring opening of MHHPA curing agent and to create more reactive sites on the anhydride (zwitterions) increases with increasing TEAB catalyst concentration. The increased number of zwitterions formation favours the polyesterification reaction in ESO thermoset and accounts for the increment in degree of conversion eventually. This finding is in good agreement with the study on the curing kinetics of bisphenol-F resin using benzyl dimethyl amine as a catalyst reported by Shokrolahi *et al.* [18] who determined the positive relationship between the catalyst concentration and the extent of conversion rate.

3.1.3. DMA characterization

The crosslink density and the molecular weight between crosslink (M_c) of the ESO thermoset as a function of TEAB concentrations are reported in Table 2. It is found that the crosslink density of

ESO thermoset increases with TEAB concentration whereas M_c exhibits a different trend. Generally, the crosslink density and M_c obtained for the ESO thermosets are found to be lower than the epoxidized vegetable oil (EVO)/petroleum-based epoxy blends [19], but close to those triethylamine catalyzed ESO/anhydride systems [20]. The increase in TEAB concentration gives rise to an increase in the number of reactive sites on the MHHPA curing agents. The consequence is an increase in the catalyzed reaction rate and the extent of conversion. This incident will attribute to an increment in crosslink density. These findings seem to contradict with the previous findings reported by Boquillon and Fringant [12] who mentioned that the crosslink density reduces with the catalyst concentration due to the diffusional restriction of the reagent at high catalyst concentration. One possible explanation could be linked to the difference in the polymerization reaction rate in both epoxy systems. The high concentration of 2-methylimidazole (2MI) catalyst in epoxidized linseed oil (ELO)/ tetrahydrophthalic anhydride (THPA) system leads to a fast gelling of the ELO thermoset. Consequently, the diffusion of the reagents is slow and results in lower extent of conversion. While, in ESO thermoset catalyzed with low TEAB concentrations, the diffusion restriction associated to vitrification is less hindered. Therefore, the extent of conversion and crosslink density increase with the catalyst concentrations. This would inherently result in lower M_c value in ESO thermoset catalyzed with higher TEAB concentration.

3.2. Thermal properties of ESO thermoset

3.2.1. Dynamic mechanical analysis

The storage modulus (E'), damping properties (tanδ) and the glass transition temperature (T_g) of thermally cured ESO thermoset are studied with DMA. The E' and tanδ of cured ESO as a function of temperature are shown in Figure 6. Basically, in the testing temperature range, the ESO thermosetting resin shows three regions of viscoelasticity: the glassy state, the leathery state and the rubbery state. As shown in Figure 6, it is determined that the E'-T curve shifts to higher temperature as the TEAB concentration in the ESO thermoset increased from 0.3 to 0.8 phr. The increment in E' as a function of TEAB concentration is attributed to the increment in crosslink density and the reduction in the molecular weight between crosslink (M_c) of the ESO thermoset. The reduction in M_c as discussed in the previous section indicates a reduction in the chain's mobility and consequently an increase in stiffness and storage modulus. This finding is in good agreement with the reduction in storage modulus with increasing M_c reported by Jin and Park [21].

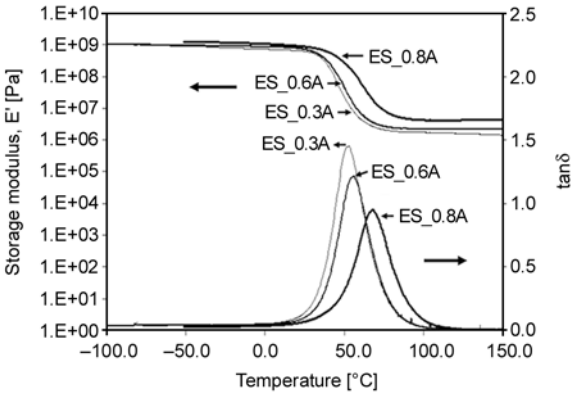

Figure 6. Effect of TEAB concentration on the E' and tanδ of ESO thermoset

Figure 6 shows the effects of TEAB concentration on the tanδ of the ESO thermosetting materials. The shifting of tanδ-T curve to lower temperature can be associated to the depression of glass transition temperature (T_g). Damping value (tanδ) of the cured ESO catalyzed with higher TEAB concentration is lower than that of those with lesser catalyst concentration. Higher crosslinked ESO thermosetting resin has the tendency to render higher elastic stiffness. Generally, the reduction in elastic constant will lead to the improvement in damping properties. Therefore, more flexible ESO thermosetting resins with lower crosslink densities would possess higher tanδ peak. In addition, it can be seen that the damping peak intensity decreases with increasing TEAB concentration. The broadening and reduction in the damping peak height with increasing TEAB concentration are due to the increase in degree of crosslinking [22, 23]. This is owing to the fact that highly cross-linked network structure can retard and restrict the chains mobility and subsequently lead to the reduction in the damping peak intensity [24].

Table 3 shows the influence of TEAB concentration on the glass transition temperature (T_g) of cured ESO thermoset. It is determined that the T_g values obtained for the TEAB-catalyzed ESO thermosets are comparable to or even higher than the existing epoxy resins based on ESO. An increment in the T_g

value is detected if the TEAB catalyst concentration increase from 0.3 to 0.8 phr. These changes in T_g values can be related to the increase in cross-link density of the curable ESO thermoset and the reduced amounts of unreacted monomer in the ESO thermoset. The presence of unreacted monomers in the thermoset would plasticize the specimens dramatically and lower the T_g value. This is owing to the fact that the plasticizing effect of unreacted monomers will add flexibility and enhance the degree of freedom for movement of the molecular chain in the 3-dimensional crosslink network structure.

However, from the DSC characterization as discussed previously, it is determined that the degrees of conversion of TEAB-catalyzed ESO thermosets, except for the ES_0.3A thermoset, approach 99%. Hence, the residual monomer concentration in cured ESO thermoset is found to be very low. It is therefore, expected that the observed change in T_g value is solely due to the influence of crosslink density in ESO thermoset. The increase in TEAB concentration gives rise to an increment in crosslink density and a reduction in degree of freedom for chain movements and internal rotation in the network structure. Moreover, the increase in TEAB concentration in ESO thermoset is expected to induce more complete curing reaction in which about all the unreacted monomers are built into three dimensional infusible cross-linked network structure of ESO thermoset. Thus, ESO thermoset catalyzed with higher TEAB concentration tends to possess higher T_g value.

3.2.2. Thermogravimetry analysis

Thermogravimetry analysis (TGA) was used in this present study to determine the thermal stability of TEAB-catalyzed ESO thermoset. Figure 7 presents the TGA and DTG curves as a function of temperature for the cured ESO thermoset. Table 3 summarizes the TGA results [i.e. onset decomposition temperature (T_o) and the maximum decomposition temperature (T_d)] for the cured ESO thermoset. It is clearly noted in Figure 7 that ESO thermoset experiences two-stage thermal decomposition when being heated up to 600°C. TEAB-catalyzed ESO thermoset passes through T_{o1} at nearly 200°C, T_{o2} at 350°C and T_d at 450°C. With approximation 25 wt% of thermal curable ESO decomposes during the first

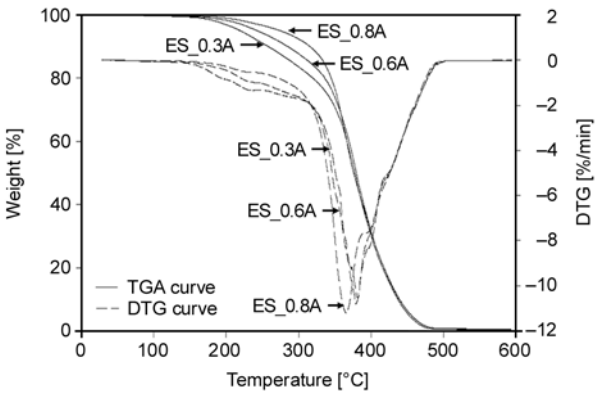

Figure 7. TGA and DTG traces of TEAB-catalyzed ESO thermosets

stage of thermal decomposition and about 71 wt% is lost during the second stage of decomposition. The remaining 4 wt% of the ESO residuals decompose totally as the heating temperature is further increased up to 500°C.

The first stage of decomposition is believed to be due to the decomposition of the low-molecular-weight components such as MHHPA curing agent or catalysts. It is believed that, generally, the low-molecular-weight compound will show lower thermal stability as the thermal stability is determined to be proportional to molecular weight. The second stage of the major decomposition which takes place at the temperature range of 350 to 400°C could be attributed to the thermal decomposition of ESO component. Similar decomposition behaviour was reported by Gerbase *et al.* [20] for the ESO/triethylamine/dodecenylsuccinic anhydride mixtures, where two different thermal decomposition stages present. Also, Hazer *et al.* [25] found that the decomposition temperature of the soya components in microbial elastomers is at around 310°C. Referring to Figure 7, the first stage effect of ESO thermoset with different TEAB concentration is found to be diverged from each other. ESO thermoset with higher TEAB concentration is determined to be more thermal stable than those thermosets with lower concentration. This finding is believed to be attributed to the increase in degree of crosslinking and crosslink density as the TEAB catalyst concentration is increased. Foussier and Rabek [26] also reported in their study that polymer system with highly cross-linked network structure commonly exhibit greater thermal stability than those systems with lower crosslinking.

3.3. Kinetics of water absorption of ESO thermoset

Figure 8 shows the effect of TEAB concentration on the water uptake of the ESO thermoset after subjected to water absorption test. It is seen that the water uptake of all TEAB-catalyzed ESO thermosetting resins reach the saturation stage at approximately 2000 hours. This is owing to the fact that the water uptake of TEAB-catalyzed ESO thermoset has achieved the equilibrium condition. The water uptake would reach the real saturation at equilibrium stage, in which all the micro-voids in the 3-dimensional crosslinked network structure are filled with water molecules [27]. Water uptake of cured ESO thermosets is attributed to the presence of free volume and hydrophilic functional groups such as hydroxyl groups in their backbone structure. The hydroxyl groups in cured ESO thermoset tend to attract water molecules which are polar in nature. The water molecules absorbed in ESO thermoset may exist as bound water or unbounded cluster.

It is clearly noted that the maximum water uptake (M_m) and water diffusion coefficient (D) of the cured TEAB-catalyzed ESO thermoset decrease with increasing TEAB concentration as shown in Table 4. It is determined that increase the number of crosslink in cured ESO thermoset would reduce the penetration of water molecules into the ESO network structure. This is owing to the fact that the intense crosslink network would hinder the water molecules to diffuse into the free volume followed by residing in the volume available in the ESO thermoset. Research study conducted by Saijun *et al*., [28] also showed that polymeric systems with higher crosslink density will possess lower free volume and lower water uptake. The water absorption behaviour is highly dependent on the free volume and chemical nature of polymer material. The high TEAB concentration in ESO thermoset would give rise to an increase in crosslinking and a decrease in free volume. This phenomenon will eventually lead to a reduction in the capability of the water molecules to penetrate and reside in the free volume. Therefore, the maximum water uptake and water diffusion coefficient of the ESO thermoset decrease with increasing TEAB concentration.

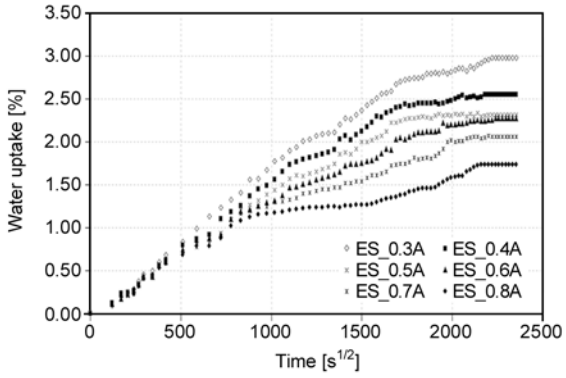

Figure 8. Effect of TEAB concentration on water uptake of ESO thermoset

Table 4. Maximum water absorption (M_m) and diffusion coefficient (D) of ESO thermoset

ESO thermoset		M_m [%]	D [10^{-12} m^2/s]
TEAB-catalyzed	ES_0.3A	2.94	1.09
	ES_0.4A	2.60	0.87
	ES_0.5A	2.34	0.73
	ES_0.6A	2.28	0.70
	ES_0.7A	2.09	0.51
	ES_0.8A	1.77	0.48

4. Conclusions

Based on the work devoted to study the effect of tetraethylammonium bromide concentration on the curing characteristic, thermal properties and kinetics of water absorption of ESO thermoset, the following conclusions can be drawn:

The polyesterification rate, degree of conversion and crosslink density were higher for ESO thermoset catalyzed with higher TEAB concentration. From the DMA and TGA studies, it was found that ESO thermoset with higher TEAB concentration possessed higher storage modulus, glass transition temperature and thermal stability. It was found that the water absorption behaviour of ESO thermoset obeyed Fickian law. The maximum water absorption (M_m) and water diffusion coefficient (D) of the ESO thermosets were in the range of 1.77 to 2.94% and 0.48 to $1.09 \cdot 10^{-12}$ m^2/s respectively. Water uptake and diffusivity of ESO thermoset can be reduced by increasing the crosslink density in the thermoset.

Acknowledgements

Authors would like to express their appreciation to Universiti Sains Malaysia for the Incentive Grant (8021013) and the Research University Postgraduate Research Grant Scheme (USM-RU-PRGS 8043019). Authors also thank Ministry of Science, Technology and Innovation (MOSTI), Malaysia for the National Science Foundation fellowship.

References

[1] Keles E., Hazer B.: Synthesis of segmented polyurethane based on polymeric soybean oil polyol and poly (ethylene glycol). Journal of Polymers and the Environment, **17**, 153–158 (2009).
DOI: 10.1007/s10924-009-0132-0

[2] Petrović S., Xu Y. J., Milić J., Glenn G., Klamczynski A.: Biodegradation of thermoplastic polyurethanes from vegetable oils. Journal of Polymers and the Environment, **18**, 94–97 (2010).
DOI: 10.1007/s10924-010-0194-z

[3] Cakmakli B., Hazer B., Acikgöz S., Can M., Cömert B.: PMMA-multigraft copolymers derived from linseed oil, soybean oil, and linoleic acid: Protein adsorption and bacterial adherence. Journal of Applied Polymer Science, **105**, 3448–3457 (2007).
DOI: 10.1002/app.26397

[4] Xia Y., Henna H., Larock C.: Novel thermosets from the cationic copolymerization of modified linseed oils and dicyclopentadiene. Macromolecular Materials and Engineering, **294**, 590–598 (2009).
DOI: 10.1002/mame.200900060

[5] Andjelkovic D., Lu Y. S., Kessler R., Larock C.: Novel rubbers from the cationic copolymerization of soybean oils and dicyclopentadiene, 2 – Mechanical and damping properties. Macromolecular Materials and Engineering, **294**, 472–483 (2009).
DOI: 10.1002/mame.200900053

[6] Liu Z., Erhan S. Z.: Ring-opening polymerization of epoxidized soybean oil. Journal of the American Oil Chemists' Society, **87**, 437–444 (2010).
DOI: 10.1007/s11746-009-1514-0

[7] Jin F-L., Park S-J.: Thermal and rheological properties of vegetable oil-based epoxy resins cured with thermal latent initiator. Journal of Industrial and Engineering Chemistry, **13**, 808–814 (2007).

[8] Gupta A. P., Ahmad S., Dev A.: Development of novel bio-based soybean oil epoxy resins as a function of hardener stoichiometry. Polymer-Plastics Technology and Engineering, **49**, 657–661 (2010).
DOI: 10.1080/03602551003681796

[9] Ortiz R. A., López D. P., Cinneros M. L. G., Valverde J. C. R., Crivello V.: A kinetic study of the acceleration effect of substituted benzyl alcohols on the cationic photopolymerization rate of epoxidized natural oils. Polymer, **46**, 1535–1541 (2005).
DOI: 10.1016/j.polymer.2004.12.020

[10] Gao Y.: Synthesis and evaluation of vegetable (soybean) oil based epoxy resin for beverage can coating. PhD thesis, Missouri Universiti of Science and Technology (2002).

[11] Tan S. G., Chow W. S.: Thermal properties, fracture toughness and water absorption of epoxy-palm oil blends. Polymer-Plastics Technology and Engineering, **49**, 900–907 (2010).
DOI: 10.1080/03602551003682042

[12] Boquillon N., Fringant C.: Polymer networks derived from curing of epoxidised linseed oil: Influence of different catalysts and anhydride hardeners. Polymer, **41**, 8603–8613 (2000).
DOI: 10.1016/S0032-3861(00)00256-1

[13] Tham W. L., Chow W. S., Mohd Ishak Z. A.: Simulated body fluid and water absorption effects on poly(methyl methacrylate)/hydroxyapatite denture base composites. Express Polymer Letters, **4**, 517–528 (2010).
DOI: 10.3144/expresspolymlett.2010.66

[14] Li Y., Gao J., Liu G., Zhang R.: Cure kinetics and thermal property of bisphenol-S epoxy resin and phthalic anhydride. International Journal of Polymeric Materials, **49**, 441–455 (2001).
DOI: 10.1080/00914030108035876

[15] Liu D., Shi Z., Matsunaga M., Yin J.: DSC investigation of the hindered effect on curing behavior for epoxy–phenol/MMT nanocomposites based on the acidic octadecylamine modifier. Polymer, **47**, 2918–2927 (2006).
DOI: 10.1016/j.polymer.2006.02.010

[16] Shin J., Nazarenko S., Hoyle E.: Effects of chemical modification of thiol−ene networks on enthalpy relaxation. Macromolecules, **42**, 6549–6557 (2009).
DOI: 10.1021/ma9001403

[17] Shin J., Nazarenko S., Paige Phillips J., Hoyle E.: Physical and chemical modifications of thiol–ene networks to control activation energy of enthalpy relaxation. Polymer, **50**, 6281–6286 (2009).
DOI: 10.1016/j.polymer.2009.10.053

[18] Shokrolashi F., Sadi M., Shokrolahi P.: A study on curing kinetic of bisphenol-F using benzyl dimethyl amine by isothermal DSC. Journal of Thermal Analysis and Calorimetry, **82**, 151–156 (2005).
DOI: 10.1007/s10973-005-0856-6

[19] Tan S. G., Chow W. S.: Biobased epoxidized vegetable oils and its greener epoxy blends: A review. Polymer-Plastics Technology and Engineering, **49**, 1581–1590 (2010).
DOI: 10.1080/03602559.2010.512338

[20] Gerbase A. E., Petzhold C. L., Costa P. O.: Dynamic mechanical and thermal behavior of epoxy resins based on soybean oil. Journal of the American Oil Chemists' Society, **79**, 797–802 (2002).
DOI: 10.1007/s11746-002-0561-z

[21] Jin F-L., Park S-J.: Impact-strength improvement of epoxy resins reinforced with a biodegradable polymer. Materials Science and Engineering: A, **478**, 402–405 (2008).
DOI: 10.1016/j.msea.2007.05.053

[22] Banik I., Bhowmick K.: Dynamic mechanical properties of electron beam modified fluorocarbon rubber. Journal of Applied Polymer Science, **69**, 2079–2087 (1998).
DOI: 10.1002/(SICI)1097-4628(19980906)69:10<2079::AID-APP19>3.0.CO;2-X

[23] Jacobs P. M., Jones F. R.: The influence of heterogeneous crosslink density on the thermomechanical and hygrothermal properties of an unsaturated polyester resin: 1. Thermomechanical response. Polymer, **34**, 2122–2127 (1993).
DOI: 10.1016/0032-3861(92)90116-E

[24] Rials G., Glasser G.: Engineering plastics from lignin - IV. Effect of crosslink density on polyurethane film properties – Variation in NCO:OH ratio. International Journal of the Biology, Chemistry, Physics and Technology of Wood, **38**, 191–199 (1984).
DOI: 10.1515/hfsg.1984.38.4.191

[25] Hazer B., Hazer D. B., Coban B.: Synthesis of microbial elastomers based on soybean oil. Autoxidation kinetics, thermal and mechanical properties. Journal of Polymer Research, **17**, 567–577 (2010).
DOI: 10.1007/s10965-009-9345-0

[26] Fouassier J. P., Rabek J. F.: Radiation curing in polymer science and technology: Fundamentals and methods. Elsevier, London (1993).

[27] Chow W. S.: Water absorption of epoxy/glass fiber/organo-montmorillonite nanocomposites. Express Polymer Letters, **1**, 104–108 (2007).
DOI: 10.3144/expresspolymlett.2007.18

[28] Saijun D., Nakason C., Kaesaman A., Klinpituksa P.: Water absorption and mechanical properties of water-swellable natural rubber. Songklanakarin Journal of Science and Technology, **31**, 561–565 (2009).

eXPRESS Polymer Letters Vol.5, No.6 (2011) 493–505
Available online at www.expresspolymlett.com
DOI: 10.3144/expresspolymlett.2011.48

Electrochemical synthesis of Poly[3, 4-Propylenedioxythiophene-co-N-Phenylsulfonyl Pyrrole]: Morphological, electrochemical and spectroscopic characterization

*F. G. Guler, A. S. Sarac**

Istanbul Technical University, Department of Chemistry, Polymer Science and Technology, Maslak, 34469, Istanbul, Turkey

Received 22 September 2010; accepted in revised form 16 December 2010

Abstract. Electroactive random copolymers of 3,4-Propylenedioxythiophene (ProDOT) and N-Phenylsulfonyl Pyrrole (PSP) were electrochemically synthesized on single carbon fiber microelectrode (SCFME) by cyclic voltammetry (CV). Fourier Transform Infrared-Attenuated Total Reflectance (FTIR-ATR) measurements indicate the inclusion of PSP into the copolymer structure. The influence of feed ratios on the copolymers was studied by CV and electrochemical impedance spectroscopy (EIS) and equivalent circuit modelling (ECM). The morphologies and film thicknesses of copolymers were characterized by scanning electron microscopy (SEM) and atomic force microscopy (AFM). The results have shown that the principal changes in morphology, conductivity, porous nature and thickness of Poly(ProDOT-co-PSP) film depend on the concentration of PSP. The strong electron-withdrawing sulfonyl group substitution on PSP significantly inhibited electrochemical copolymerization. Semicircular characteristics at Nyquist plots reflected an increasing trend with the increase of PSP concentration in the feed at high frequency. The semicircular characteristic of the copolymer film is useful for the bioelectrochemical sensor applications.

Keywords: *polymer synthesis, molecular engineering, electrocopolymerization, copolymer of ProDOT, Electrochemical Impedance Spectroscopy*

1. Introduction

Conductive polymers have been electrochemically preferred because of their physical or chemical properties such as volume, color, stored charge or porosity and used for a number of applications such as electrochromic displays [1–11], smart windows [12], solar cells [13–14], supercapacitors [15–16] and biosensors [17–18].

3,4-alkylenedioxythiophene based polymers exhibit low oxidation potential, high and quite stable conductivities, a high degree of optical transparency as a conductor, and the ability to be rapidly switched between conducting doped and insulating neutral states. Substitution at the 3- and 4-positions of thiophene prevents the occurrence of α-β and β-β coupling during electropolymerization, yielding more ordered polymers with longer conjugation lengths. The synthesis of 3,4-disubstituted polythiophenes was carried out stabilizing the oxidized form, providing solubility, processability [19].

Poly(ProDOT) was synthesized by the traditional double-Williamson etherification route, having $\Delta\lambda$%T of 66% at λ_{max} compared to the 54% transmittance change for PEDOT [20]. ProDOT exhibited higher contrast in comparison to conjugated polymers from EDOT [1].

*Corresponding author, e-mail: sarac@itu.edu.tr

Side-chain derivatization is possible due to ProDOT flexibility of the conjugated backbone structure. The dimethyl and diethyl derivatives especially exhibit enhanced electrochromic contrasts throughout the visible region [21] and high capacitive behaviors [15–16]. A series of Poly(ProDOTs) are disubstituted with long chain esters. This functionality enhances solubility in polar solvents [22]. Electropolymerization of hydroxymethyl-substituted 3, 4-Propylene dioxythiophene monomer (ProDOT-OH) was easily performed [23]. Multiwalled carbon nanotubes (MWNTs) were functionalized with Poly(ProDOT) by oxidative polymerization and MWNT-g-PProDOT hybrid was prepared and showed that improved thermal stability [24].

Films of conjugated polymers are generally synthesized onto a support electrode surface by electropolymerization (anodic oxidation) of the corresponding monomer in the presence of an electrolyte solution. Carbon fibers have highly accessible surface area, low resistivity and high stability which consist of stacked hexagonal carbon layers, forming small coherent units (crystallites) of only a few micrometers in the stacking direction [25]. Electropolymerization on carbon fiber microelectrode (CFME) can improve the interfacial properties between the carbon fiber and polymeric matrix. Generally electrocoating of conjugated polymers on carbon fiber easily allows the characterization of the deposited films by spectroscopic, morphological and electrochemical techniques. Conducting polymers which were coated electrochemically onto CFMEs were studied in detail and reported by Sarac and coworkers [16, 26–33].

Electrochemical impedance spectroscopy (EIS) is a powerful technique to study charge transfer, ion diffusion and capacitance of conducting polymer modified electrodes [34–39]. EIS has been used to develop equivalent electric circuits to describe the electrochemical properties of films of conducting polymers in organic solution [40–41]. EIS has also provided information concerning corrosion protection by inhibitors [42–47].

The chemical synthesis through two different methods of N-phenylsulfonyl pyrrole (PSP) was reported and used as a gas sensitive resistor [48]. N-phenyl sulfonyl-1H-pyrrole-3-sulfonyl chloride was synthesized by using chromosulphonic acid in acetonitrile [49].

The copolymers from different monomers or comonomers have been synthesized by both electrochemical and chemical oxidative polymerizations to efficiently modify the structure and to improve the properties of the conducting polymers [50–55]. The electrochemical polymerization allows obtaining materials with controlled properties without suffering the experimental disadvantages [56].

In this paper, we report the electrochemical random copolymerization of ProDOT and PSP onto different working electrodes. The electrochemical and morphological properties of Poly(ProDOT) and copolymer films were characterized by FTIR-ATR, EIS, SEM and AFM. The electrochemical impedance data was fitted to an equivalent circuit in order to identify differences between the conductivities of Poly(ProDOT) and copolymers. Briefly, the effect of PSP mole fractions on the electrochemical and morphologic properties of resulting copolymers using alternative characterization techniques was shown with this paper.

2. Experimental details

2.1. Chemicals and materials

SGL SIGRAFIL C 320B (SGL Carbon Group, Meitingen, Germany; a high strength and high modulus of elasticity coupled with high electrical conductivity carbon fibers) containing single filament in a roving were used as a working electrode. ProDOT and PSP were purchased from Sigma-Aldrich (Germany) and used as received. Electrochemical polymerizations (electrocoatings) were performed in acetonitrile (ACN, Merck, Darmstadt, Germany) containing $NaClO_4$ (Sigma-Aldrich, Germany) at the same scan rate (30 mV/s) and deposition cycle numbers (10 cycles) (applied charges).

2.2. Characterization

Electrochemical measurements (EIS with supplied Power Sine software package and Cyclic Voltammograms) were performed with a Princeton Applied Research (PAR) Parstat 2263 potentiostat (Oak Ridge, USA). The potentiostat is a self-contained unit that combines potentiostatic circuitry with phase-sensitive detection. The impedance measurements were carried out by scanning in the frequency range

10 mHz–100 kHz with applied AC signal amplitude of 10 mV using Power Sine. The impedance spectrum was analyzed using AC impedance data analysis software (ZSimpWin V3.10, Michigan, USA).

For spectroscopic measurements, Poly(ProDOT-co-PSP) copolymers were synthesized onto ITO-PET (NV Innovative Sputtering Technology, Zulte, Belgium, PET 175 μm,Coating ITO-60) in the potential range from –0.8 to 1.5 V at a scan rate of 50 mV/s in 0.1M $NaClO_4$/ACN. Polymer films on ITO-PET were analysed using an ATR-FTIR reflectance spectrometer (Perkin Elmer, Spectrum One, California, USA; having a universal ATR attachment with a diamond and ZnSe crystal C70951). Perkin Elmer Spectrum software was used to carry out FTIR-ATR measurements between 650–4000 cm^{-1}.

Thin films of copolymers, electrocoated onto carbon fibers were analyzed by scanning electron microscopy on a Nanoeye Desktop Mini-SEM (SEC. Co., Ltd.; South Korea) The increase in the average values of film thicknesses was obtained via SEM images taking into account the diameter of the uncoated fiber. The diameters for the fibers were calculated from an average of 5–6 measurements on individual fibers.

Thin film of copolymer, electrocoated onto silicon wafer (n-doped, Cz type; Wacker Siltronic AG., München, Germany) was analyzed by atomic force microscopy (AFM) using a Nanosurf Easyscan 2 AFM (Nanoscience Instruments, Liestal ,Switzerland) instrument with a 10 μm AFM head.

2.3. Preparation of Single Carbon Fiber Microelectrodes (SCFMEs)

A three-electrode system was used employing SCFME which was prepared by using a single carbon fiber (diameter ~7 μm) that was rolled to a copper wire and fixed with a Teflon tape and inserted into a glass capillary (diameter ~4.45 mm) as working electrode. The single carbon fiber and copper wire were attached and connected to the potentiostat. ~1 cm of SCFME was dipped into the electrolyte solution to keep the electrode area costant (~$2 \cdot 10^{-3}$ cm^2). Button electrodes were prepared by using Ag and Pt wires in glass capillary (~4.45 mm diameter) filled with MMA and polymerized by UV light, which was inert against the electrolyte solution. The reference and counter electrode surface areas were kept constant (~0.47 mm^2) during the experiments.

3. Results and discussions

3.1. Electrocopolymerization of ProDOT and PSP

ProDOT and PSP were electrochemically copolymerized on SCFMEs in the potential range from –0.8 to 1.5 V at a scan rate of 30 mV/s in 0.1M $NaClO_4$/ACN. After 10 potential cycles completed, the working electrode surfaces were washed and analyzed in monomer free solution (0.1M $NaClO_4$/ACN) to find out their redox behaviour at different scan rates between 15 and 200 $mV \cdot s^{-1}$ by CV. The amount of PSP concentration was increased from 5 to 20 mM when ProDOT concentration was held constant (10 mM). Three copolymers with different compositions were synthesized with by using X_{PSP} = [(PSP/(ProDOT+PSP)] mole fraction [CP1 (0.33), CP2 (0.50), and CP3 (0.66)].

The potential shift to the positive direction with an increase of PSP concentration in the feed indicates that the monomer ratio affects the copolymer composition and its electrochemical properties. The obvious peak potential shift provided information about the increase in the electrical resistance in the copolymer film. As shown at multisweep cyclic voltammograms of ProDOT (10 mM) in the presence of PSP (5; 10; 20 mM); the intensity of the current peaks increased with increase in the number of potential cycles indicating a continuous growth of electroactive copolymer on the electrode (Figure 1a, c).

For repeated cycling the cathodic peak current decreases and the anodic one increases until a steady-state pattern. Also the current during the first cycle was quite different from that in the second cycle. After 5 cycles the system has settled down. Results obtained from multiple cycling showed that the first five cycles of the voltammogram were usually in unstable stage (Figure 1a–c). After five cycles, steady state condition (6^{th} cycle) was achieved.

Oxidation potentials (E_{ONSET}) of CP1 and CP2 were obtained as 1.139 and 1.127 V higher than oxidation potential of CP3 (1.19 V) during the electrogrowth process. This is due to increased PSP concentration in feed ratio. The strong electron–withdrawing sulfonyl group in PSP can be stabilized by using the radical cation intermediates to

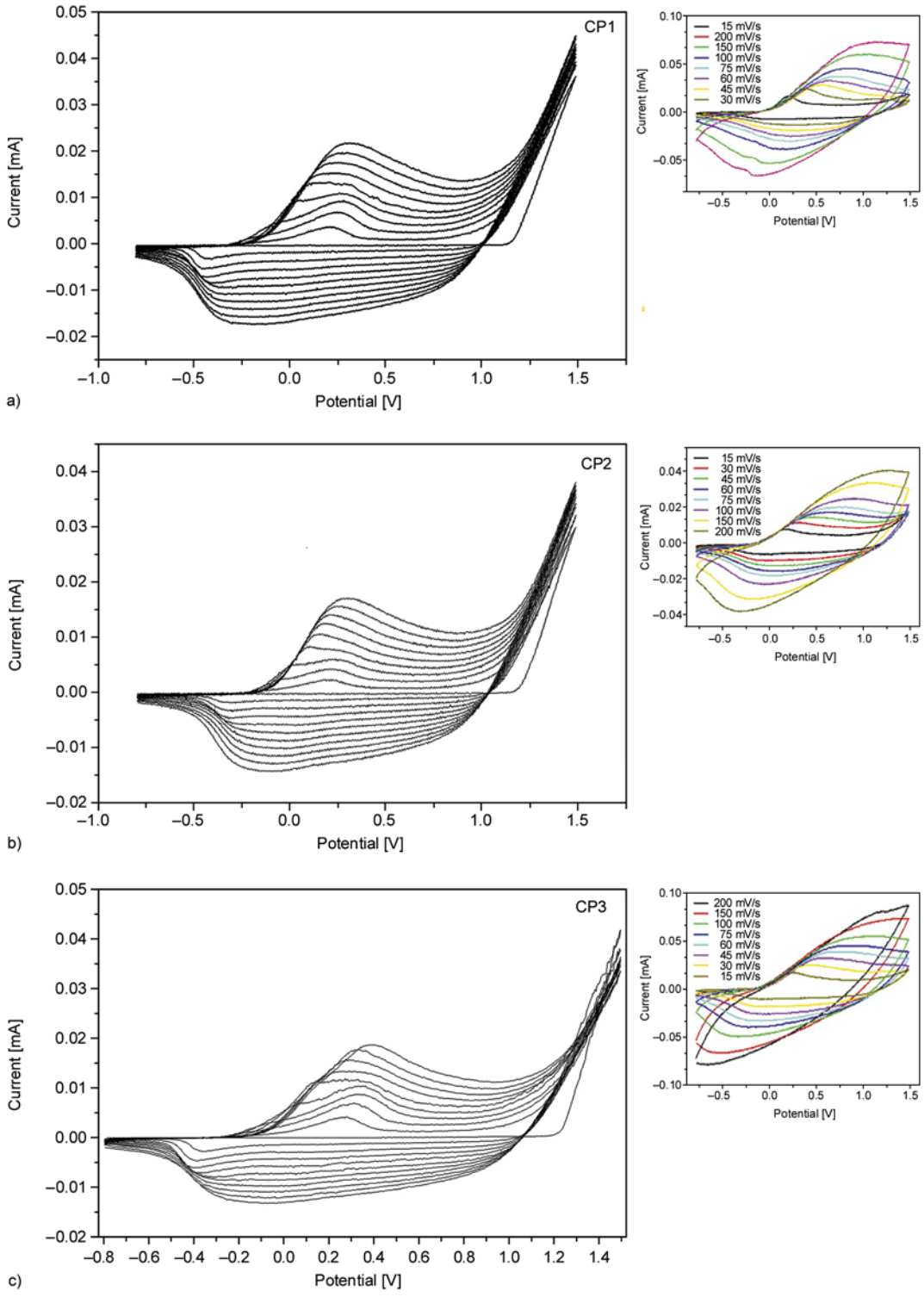

Figure 1. Cyclic voltammetry of electrogrowth of 10 mM ProDOT and (a) 5 mM (CP1), (b) 10 mM (CP2), (c) 20 mM (CP3) PSP in 0.1M $NaClO_4$/ACN; scan rate: 30 mV/s; scan number: 10 cycles on SCFME. Graphs on right hand side: CV of monomer-free diagrams belongs to Poly(ProDOT-co-PSP) in 0.1M $NaClO_4$/ACN at different scan rates (15 to 200 mV/s)

diffuse away from the electrode and thus inhibiting electropolymerization (Table 1). The peak current decreased in direct proportion with decrease of oxidation potential (Figure 2).

The anodic and cathodic peak current increased with increase in scan rate. Figure 3a and b show that the anodic and cathodic redox reaction for the copolymers formed in 0.1M $NaClO_4$/ACN appear to be

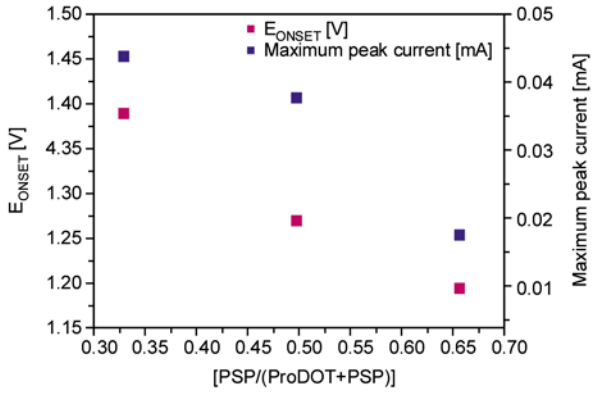

Figure 2. Plot of oxidation potential and maximum peak current obtained from CV for different mole fraction of Poly(ProDOT-co-PSP)

diffusion-controlled, as proved by the linearity of the plot and are extremely reversible even at high scan rates.

3.2. *Ex-situ* FTIR-ATR measurements of Poly(ProDOT-co-PSP) and Poly(ProDOT)

For spectroscopic characterization of Poly(ProDOT-co-PSP) films, the same mole fractions of the copolymers were also prepared by cyclic voltammetry on ITO-PET with the same conditions of random Poly (ProDOT-co-PSP) films formation on SCFME (Figure 4).

Inclusion of PSP into the electrocopolymerized thin film, and doping with the respective anion of the supporting electrolyte were followed by FTIR-ATR (Figure 5). This technique allows us to assign corresponding functional groups in the resulting copolymer.

Table 1. Comparison of thickness of copolymer coated SCFME, ΔQ, C_{LF} and phase angle of copolymer films

Copolymers	CP1	CP2	CP3
ΔQ [mC]	7.184	5.498	3.305
Thickness of copolymer coated SCFME [μm]	19.86	15.75	11.15
C_{LF} [mF·cm^{-2}]	173.5	172.3	65.5
~i_{pa} * [mA]	0.044	0.038	0.018
E_{ONSET} [V]	1.139	1.127	1.119
Phase of Z [°]	66.99°	51.18°	43.28°

*i_{pa} values are anodic current peaks, obtained from 10th cycles of cyclic voltammograms

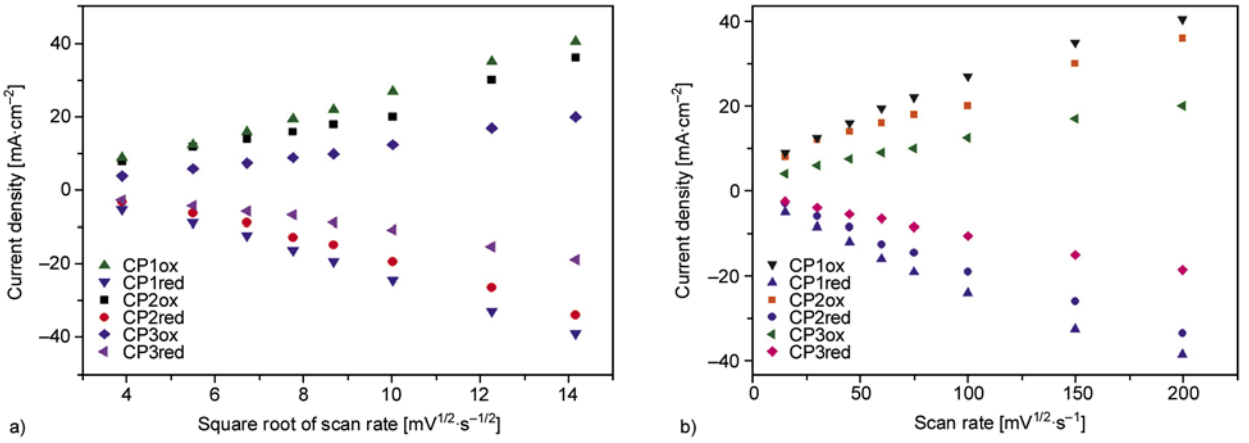

Figure 3. Plots of anodic and cathodic peak current density (a) square root of scan rate, (b) scan rate dependent on the copolymer films in monomer free solution in 0.1M $NaClO_4$/ACN

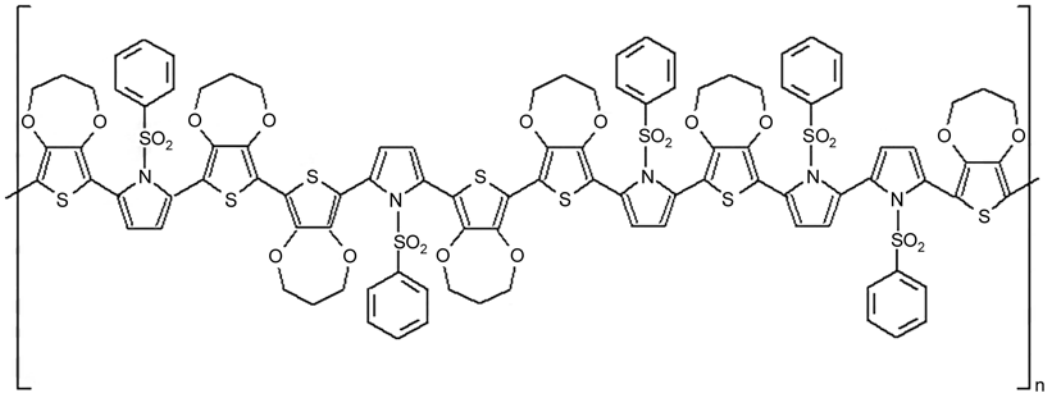

Figure 4. Chemical structure of random Poly(ProDOT-co-PSP)

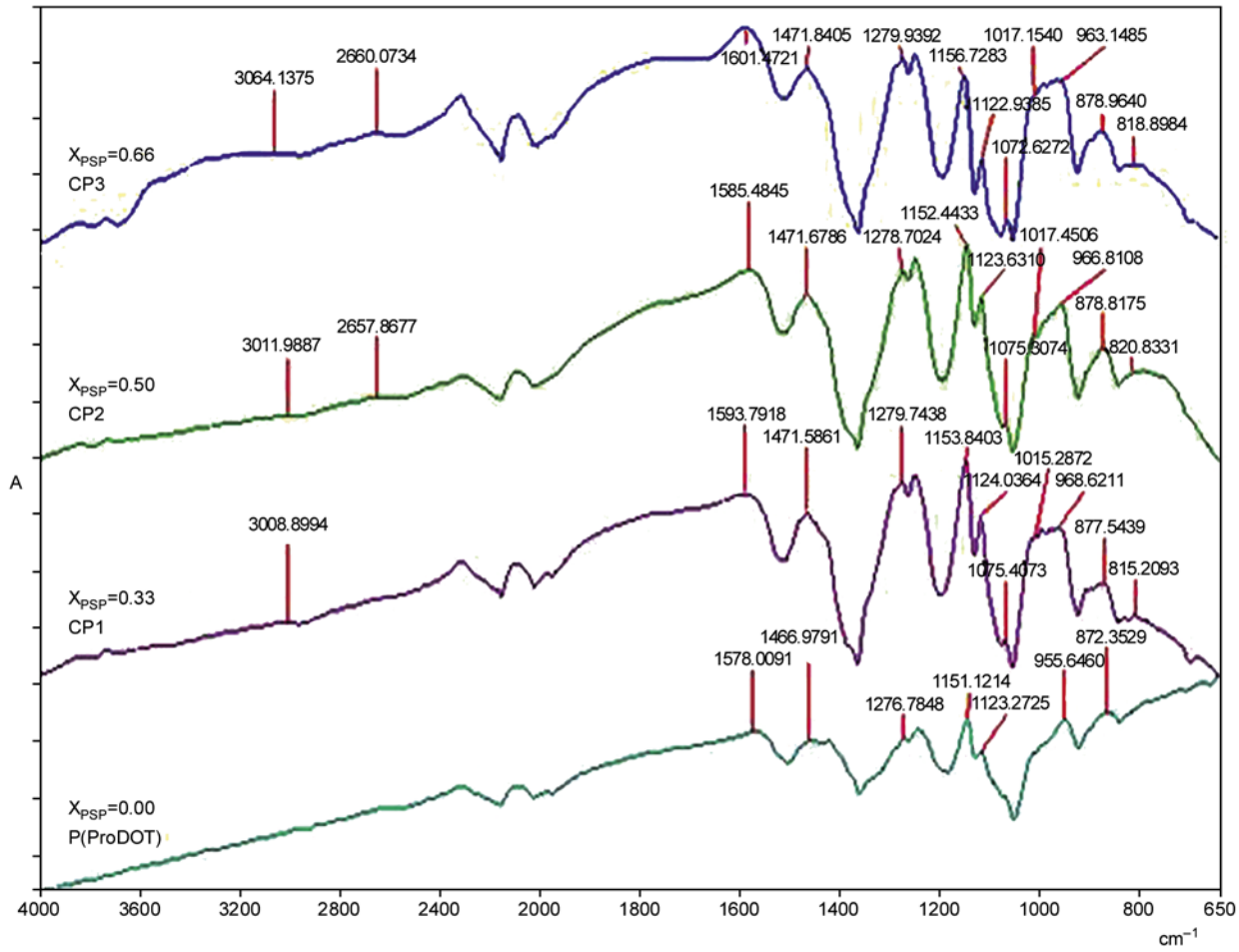

Figure 5. Ex-Situ FTIR-ATR spectrum of Poly(ProDOT-co-PSP) and Poly(ProDOT) films on ITO-PET

Table 2. FTIR-ATR assignments of Poly(ProDOT-co-PSP)s and Poly(ProDOT)

[cm^{-1}]	Poly(ProDOT)	CP1	CP2	CP3
C–H stretching (aromatic)	–	3008	3011	3064
C–H deformation (aromatic)	–	–	2657	2660
CH_2 wagging	1123	1122	1124	1123
C=C stretching (thiophene ring)	1466	1471	1471	1471
Sulfonyl stretching	–	1075	1075	1072
The stretching quonidal structure of thiophene	1276	1279	1278	1279
C–O–C group stretching	1151	1153	1152	1156
C–N stretching (N-substitued pyrrole)	–	1015	1018	1017
C–O bending	955	963	968	966
C–H bending (aromatic)	–	815	820	818
C–S stretching	872	877	878	879

The band at 1466–1471 cm^{-1} (stretching of C=C bond) and the peak at 1276–1279 cm^{-1} (the stretching quinoidal structure of thiophene) are known to be characteristic vibrational peaks of polythiophene. Vibrations at 1151–1156 cm^{-1} are assigned to stretching in the alkylenedioxy group (C–O–C bond). The band at 1015–1018 cm^{-1} (C–N stretching) originated from the N-substitued pyrrole of PSP. Sulfonyl stretching at 1072–1075 cm^{-1}, aromatic C–H bending (815–820 cm^{-1}) and aromatic C–H stretching (3008–3064 cm^{-1}) become distinct when PSP ratio is increased in the copolymer. Further vibrations from the C–S bond, in the thiophene ring, can be seen at 872–879 cm^{-1}, attributed to C–S stretching. All assignments were denoted in Table 2.

3.3. Morphological analysis of Poly(ProDOT-co-PSP) films

The morphologies of copolymer coatings onto SCMFEs were investigated by SEM (Figure 6). By

using small size electrolyte anions as ClO_4^-, a high density of pores was obtained in the films. SEM images of copolymers of this study have similar porous structure with ProDOT-Et_2 [57]. The observed differences at film thicknesses were obtained due to an increase of PSP in the feed (Table 1). This thickness difference helps us to follow the incorporation of PSP into the copolymer structure. The difference in the capacitance is also due to change of film thickness and fiber morphology in the course of their modification. A continuous increase in current with successive scans is observed,

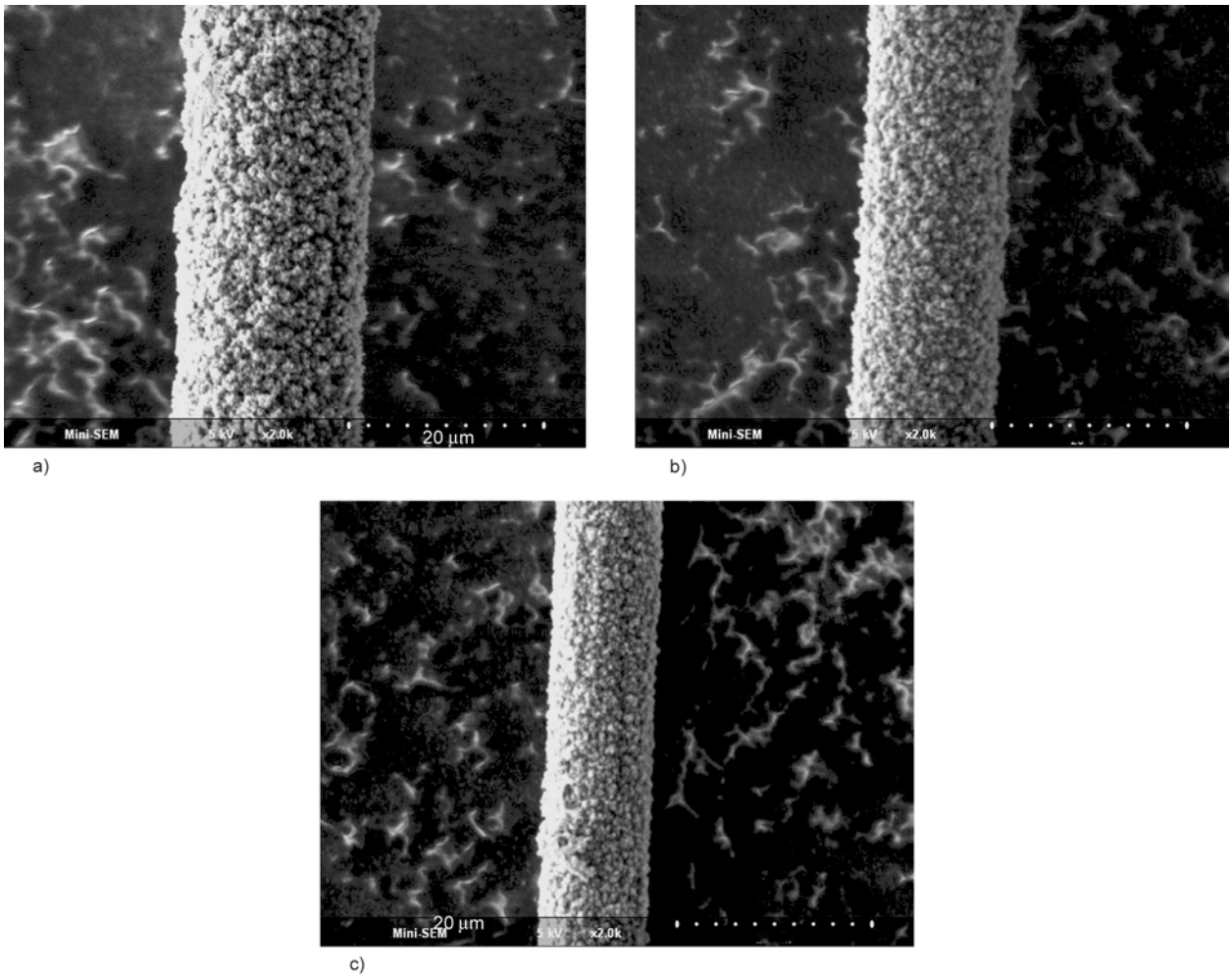

Figure 6. SEM images of CP1 (a), CP2 (b) and CP3 (c) electrocoated onto SCMFE in 0.1M $NaClO_4$/ACN after 10 cycles

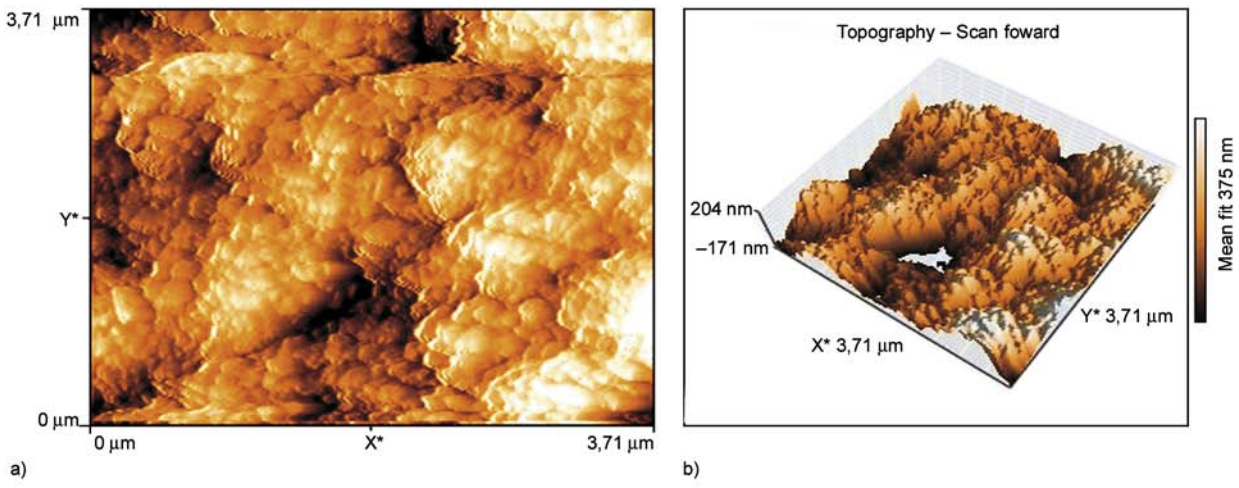

Figure 7. AFM (a) and 3D AFM (b) topographies of the silicon wafer electrode surface after modification with the CP1

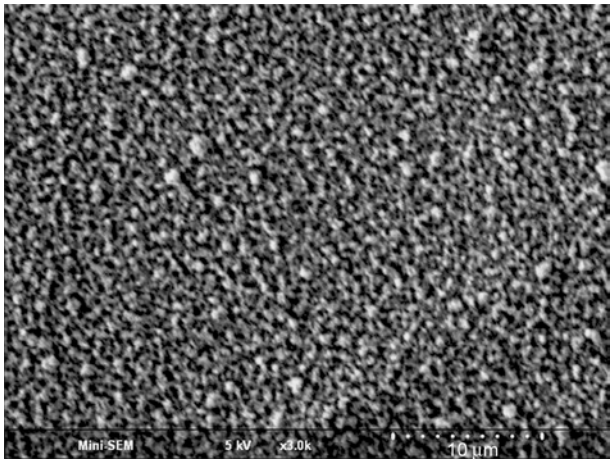

Figure 8. SEM image of the silicon wafer electrode surface after modification with the CP1

indicating an increase in the thickness, and also in the conductivity of the polymeric film formed on the electrode surface, which is followed by CV measurements [58].

The monomer mixture of ProDOT (10 mM) and PSP (5 mM) was copolymerized at constant potential (1.0 V) by chronoamperometry onto silicon wafer for AFM analysis. The images were obtained at none-contact mode AFM (Figure 7). Root mean square (RMS), roughness value was calculated via Nanosurf Easyscan 2 software program by selecting raw data (RMS: 65.8 nm). The SEM image was also obtained for modified silicon wafer (Figure 8). These spherical-shape aggregates were obtained by the growth of much smaller nanoscale aggregates dependent on the polymerization charge.

3.4. Electrochemical Impedance Spectroscopy

The electrical properties of Poly(ProDOT) and copolymers on SCFMEs were determined by electrochemical impedance measurements in monomer free solution. The Nyquist, Bode Magnitude and Bode Phase plots of thin films were given in the frequency range 0.01 Hz–100 kHz (Figure 9a–c).

The copolymers are also exhibiting different impedance data from that of Poly(ProDOT) which shown an ideal capacitive line (Bode phase angles close to 90°) by the application of electrochemical impedance spectroscopic measurements, indicating fast charge transfer at the carbon fiber/polymer and polymer/solution interfaces, as well as fast charge transport in the polymer bulk. Bode-phase angles which approached the maximum at 0.01 Hz were ~ 66.99° for CP1, ~51.18° for CP2 and ~43.28° for

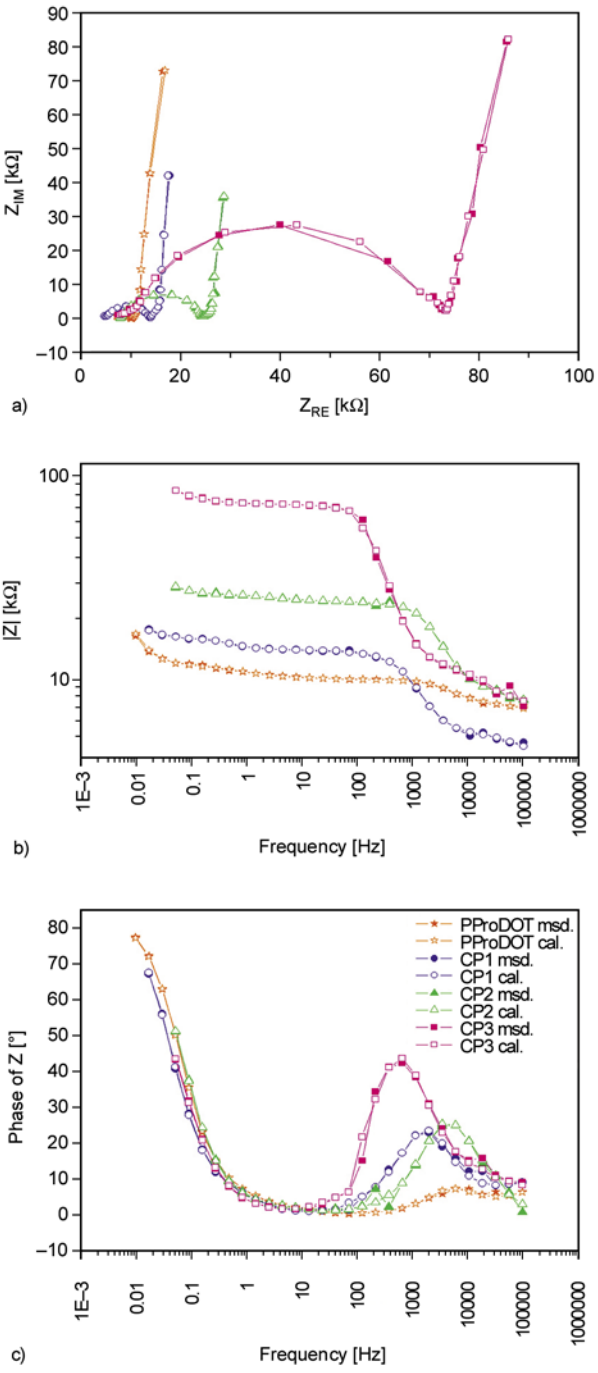

Figure 9. (a) Nyquist (b) Bode magnitude (c) Bode phase plots of of different mole fractions of Poly (ProDOT-co-PSP) electrografted on SCFMEs; correlated with the calculated data from the equivalent circuit modelling; (R(W(CR)(QR))(CR))

CP3, respectively, (Figure 9c). That indicates the presence of PSP in copolymer structure. The Bode-phase peaks of the copolymers in the frequency range of 10 Hz–10 000 Hz appeared which should be caused by the transition from resistor to capacitor with the increase of PSP ratio. The Bode magnitude plots for copolymers were presented in Fig-

ure 9b, CP1 had higher conductivity compared to CP2 and CP3. Nyquist plots were also used to estimate the low-frequency redox capacitance (C_{LF}) of the copolymer-modified SCFMEs. It can be evaluated from the equation $C_{LF} = -1/(2\pi \cdot f \cdot Z_{IM})$, where Z_{IM} is the obtained from the slope of a plot of the imaginary component of the impedance at low frequencies versus inverse of the reciprocal frequency f (f = 0.01 Hz) and other symbols have their usual meanings.

The C_{LF} and film thickness of copolymers decreased which indicates the increase of PSP concentration in the feed. Total charges were obtained during electrogrowth process as 7.184, 5.489 and 3.305 mC (Table 1). The increase of PSP concentration in the feed resulted the decrease in film thickness and growth rate of copolymer. This is confirmed by the cyclic voltammetry of mixture of monomers, the decrease found in the total charge, film thickness and C_{LF} in the plot of it against PSP mole fraction of copolymer (Figure 10).

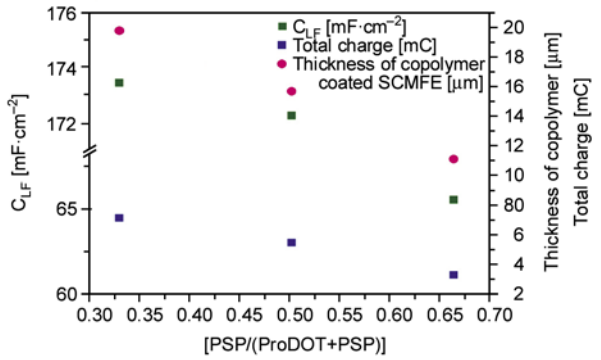

Figure 10. Thicknesses of copolymer coated SCFMEs obtained from SEM, low frequency capacitances and total charges (ΔQ) which were applied during the electropolymerization, for different mole fractions of Poly(ProDOT-co-PSP)

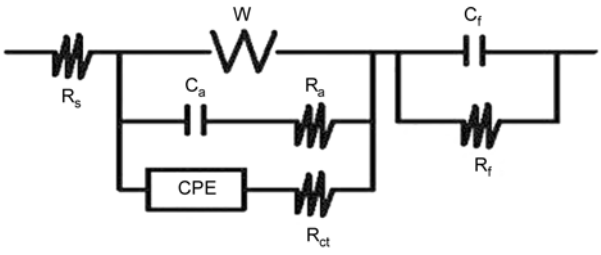

Figure 11. The equivalent circuit model of Poly(ProDOT), CP1, CP2 and CP3 coating on a single carbon fiber electrode. (R_s = solution and pore resistance and W = Warburg impedance, Z_W; R_a and C_a are the resistance and the adsorption capacitance; R_{ct} = charge transfer resistance; CPE is used for modelling the double layer capacitance, C_{dl}; R_f and C_f are film resistance and film capacitance of coated copolymer film on carbon fiber microelectrode)

The Nyquist plots (complex plane plots) were semicircles and formed under ideal conditions for biosensing [59]. The diameter of the semi-circle increased with an increase of PSP in the feed that destroys the integrated aromatic system of thiophene. It corresponds to the charge transfer resistance which included in the equivalent circuit (Figure 11) as the resistance of the modified electrode.

3.5. Electrical equivalent circuit

The EIS data were fitted with an equivalent electrical circuit in order to characterize the electrochemical properties of copolymer. The experimental results obtained from equivalent circuit have shown that both the double-layer and the film capacitances decreased with the increase of incorporated PSP ratio into copolymer structure, while the charge-transfer and the pore resistance increased.

The most widely used is the constant phase element (CPE), which has a non-integer power dependence on the frequency. CPE is used in a model in place of a capacitor C_{dl} (double layer capacity) to compensate for roughness of the electrode, porosity and nonhomogeneity in the system. A rough or porous surface can cause a double-layer capacitance to appear as a CPE with a n value between 0.9 and 1 [60]. In this study, CPE was used as double layer capacitance due to a porous structure (n~1) (Table 3). The impedance spectra for copolymers may be described by the equivalent circuit of Figure 11, (R(W(CR)(QR))(CR)). The model is composed of the electrolyte and pore resistance (R_s), the adsorption capacitance and resistance (C_a and R_a), double-layer capacitance and charge-transfer resistance (C_{dl} and R_{ct}), Warburg impedance (W), resitance and capacitance of the copolymer film onto SCMFE (R_f and C_f). R_a and C_a connected with the charging/discharging process in the surface of the film. Both of these parameters improve the quality-of-fit of the frequency dispersion transition between the charge transfer semi-circle and the Warburg impedance or capacitance line. C_{dl} and R_{ct} formed by the inward penetration of ClO_4^- anion along pores at the electrolyte|copolymer interface. W is related to diffusion of species along the micropores and depends

Table 3. Mole fraction dependence of parameters calculated from the equivalent circuit model for Poly(ProDOT) and Poly(ProDOT-co-PSP) films on SCFME

	Poly(ProDOT)	CP1	CP2	CP3
R_S [Ω·cm^2]	2.528	4.738	12.574	14.656
W/Y_0 [μS·s^{-n}·cm^{-2}]	0.0253	0.218	0.278	0.528
C_a [mF·cm^{-2}]	92.35	41.35	27.98	5.08
R_a [Ω·cm^2]	8.25	11.37	15.57	34.06
C_{dl} [mF·cm^{-2}]	466.95	176.05	118.80	55.30
n	0.946	0.974	0.902	0.906
R_{ct} [Ω·cm^2]	19.75	41.66	78.34	167.84
C_f [mF·cm^{-2}]	117.22	0.02	0.013	0.0053
R_f [Ω·cm^2]	3.85	19.19	25.26	107.60
Chi Squred, χ^2	$1.955 \cdot 10^{-4}$	$7.565 \cdot 10^{-4}$	$7.878 \cdot 10^{-4}$	$2.969 \cdot 10^{-3}$

on the electrode geometry (spherical diffusion at microelectrode).

At Nyquist plots of copolymers, appeared semi-circle in high frequency range was associated with anion transfer at the film|solution interface and can be described by the charge transfer resistance R_{ct}, in series combination with a CPE. The increase in diameter of the circle, i.e., higher the charge transfer resistance (R_{ct}), is most useful for biosensing [59]. After the charge transfer semi-circle, straight line at the x-axis can be related to Warburg impedance, Z_W, due to the diffusion of charged species in the film at low frequency.

The copolymers have high electrolyte and pore resistivity (R_s), resulting from the decrease in pore size and film thickness, making it more difficult to maintain connectivity between the pores and causing the lowest interfacial area for charge transport. Film capacitance (C_f), double-layer capacitance (C_{dl}) and adsorption capacitance (C_a) were found to be inversely proportional to the concentration of PSP (Figure 12).

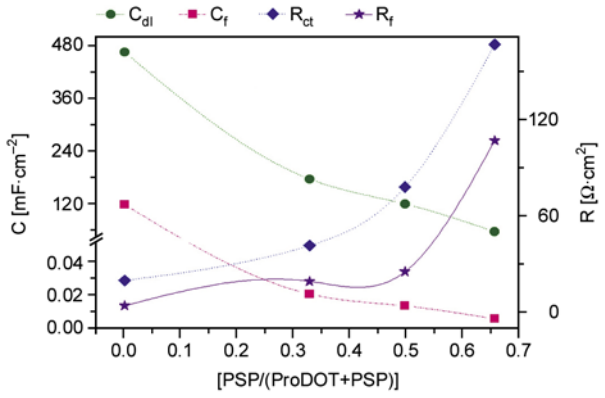

Figure 12. Charge transfer (R_{ct}) and film (R_f) resistances; double layer (C_{dl}) and film (C_f) capacitances obtained by fitting experimental data to the equivalent circuit model for Poly(ProDOT), CP1, CP2 and CP3

4. Conclusions

A new copolymer, obtained from ProDOT and PSP by the cyclic voltammetry, was successfully synthesized. The experimental results from CV and EIS and the theoretical results obtained from equivalent circuit combined with morphological characterization. FTIR-ATR characteristic peaks of PSP indicate the inclusion into copolymer. A decrease in peak currents and total charges of copolymer was observed as compared to homopolymer of Poly(ProDOT). The changing of the capacitance properties, film thickness and fiber morphology was found to be inversely proportional to the increasing PSP concentration in the feed. These information hints that sulfonyl group in PSP has very strong electron-withdrawing effect thus making it difficult to polymerize electrochemically. The capacitance properties of copolymers at lower frequency become smaller as compared to Poly(ProDOT), hence suggesting an increase in the sulfonyl content in the copolymer due to the addition of PSP, which in turn suggests more sulfonyl structure in the copolymer. The changing of the capacitance of the copolymer is reflected by the equivalent circuit model by the dependency of the mole fractions. The decreasing of the film thickness obtained from SEM and the decrease of capacitance values clearly indicates the inclusion of PSP into copolymer. The well-defined electrochemistry of Poly(ProDOT-co-PSP) films onto SCMFEs opens up the possibility for bioelectrochemical sensor electrodes.

Acknowledgements

This work was supported by TUBITAK 107T933 project which was acknowledged.

References

[1] Padilla J., Seshadri V., Filloramo J., Mino K., Mishra P., Radmard B., Kumar A., Sotzing A., Otero F.: High contrast solid-state electrochromic devices from substituted 3,4-propylenedioxythiophenes using the dual conjugated polymer approach. Synthetic Metals, **157**, 261–268 (2007).
DOI: 10.1016/j.synthmet.2007.03.003

[2] Carpi F., DeRossi D.: Colours from electroactive polymers: Electrochromic, electroluminescent and laser devices based on organic materials. Optics and Laser Technology, **38**, 292–305 (2006).
DOI: 10.1016/j.optlastec.2005.06.019

[3] Padilla J., Seshadri V., Otero T. F., Sotzing G. A.: Electrochemical study of dual conjugated polymer electrochromic devices. Journal of Electroanalytical Chemistry, **609**, 75–84 (2007).
DOI: 10.1016/j.jelechem.2007.06.008

[4] Kimura G., Yamada K.: Electrochromism of poly(3,4-ethylenedioxythiophene) films on Au nano-brush electrode. Synthetic Metals, **159**, 914–918 (2009).
DOI: 10.1016/j.synthmet.2009.01.055

[5] Yamada K., Seya K., Kimura G.: Electrochromism of poly(pyrrole) film on Au nano-brush electrode. Synthetic Metals, **159**, 188–193 (2009).
DOI: 10.1016/j.synthmet.2008.08.009

[6] Welsh D. M., Kumar A., Morvant M. C., Reynolds J. R.: Fast electrochromic polymers based on new poly (3,4-alkylenedioxythiophene) derivatives. Synthetic Metals, **102**, 967–968 (1999).
DOI: 10.1016/S0379-6779(98)01014-5

[7] Camurlu P., Şahmetlioğlu E., Şahin E., Akhmedov I. M., Tanyeli C., Toppare L.: Fine tuning of color via copolymerization and its electrochromic device application. Thin Solid Films, **516**, 4139–4144 (2008).
DOI: 10.1016/j.tsf.2007.10.098

[8] Xia X. H., Tu J. P., Zhang J., Huang X. H., Wang X. L., Zhang W. K., Huang H.: Multicolor and fast electrochromism of nanoporous NiO/poly(3,4-ethylenedioxythiophene) composite thin film. Electrochemistry Communications, **11**, 702–705 (2009).
DOI: 10.1016/j.elecom.2009.01.017

[9] Sahoo R., Mishra S. P., Kumar A., Sindhu S., Rao K. N., Gopal E. S. R.: Novel high contrast electrochromic polymer materials based on 3,4-propylenedioxythiophene. Optical Materials, **30**, 143–145 (2007).
DOI: 10.1016/j.optmat.2006.11.030

[10] Jain V., Sahoo R., Mishra S. P., Sinha J., Montazami R., Yochum H. M., Heflin J. R., Kumar A.: Synthesis and characterization of regioregular water-soluble 3,4-propylenedioxythiophene derivative and its application in the fabrication of high-contrast solid-state electrochromic devices. Electrochromic Devices Macromolecules, **42**, 135–140 (2009).
DOI: 10.1021/ma801708d

[11] Wen Z., Itoh T., Uno T., Kubo M., Wen T., Yamamoto O.: Polymer electrolytes based on poly(ethyleye oxide) and cross-linked poly(ethylene oxide-co-propylene oxide). Solid State Ionics, **175**, 739–742 (2004).
DOI: 10.1016/j.ssi.2003.10.023

[12] Invernale M. A., Bokria J. G., Ombaba M., Lee K-R., Mamangun D. M. D., Sotzing G. A.: Variable-color poly(3,4-propylenedioxythiophene) electrochromics from precursor polymers. Polymer, **51**, 378–382 (2010).
DOI: 10.1016/j.polymer.2009.12.015

[13] Hou Y., Cheng Y., Hobson T., Liu J.: Design and synthesis of hierarchical MnO_2 nanospheres/carbon nanotubes/conducting polymer ternary composite for high performance electrochemical electrodes. Nano Letters, **10**, 2727–2733 (2010).
DOI: 10.1021/NL101723g

[14] Campos L. M., Mozer A. J., Günes S., Winder C., Neugebauer H., Sariciftci N. S., Thompson B. C., Reeves B. D., Grenier C. R. G., Reynolds J. R.: Photovoltaic activity of a PolyProDOT derivative in a bulk heterojunction solar cell. Solar Energy Materials and Solar Cells, **90**, 3531–3546 (2006).
DOI: 10.1016/j.solmat.2006.06.051

[15] Hsu C-Y., Chen H-W, Lee K-M., Hu C-W., Ho K-C.: A dye-sensitized photo-supercapacitor based on PProDOT-Et2 thick films. Journal of Power Sources, **195**, 6232–6238 (2010).
DOI: 10.1016/j.jpowsour.2009.12.099

[16] Sarac A. S., Gilsing H-D., Gencturk A., Schulz B.: Electrochemically polymerized 2,2-dimethyl-3,4-propylenedioxythiophene on carbon fiber for microsupercapacitor. Progress in Organic Coatings, **60**, 281–286 (2007).
DOI: 10.1016/j.porgcoat.2007.07.025

[17] Ates M., Sarac A. S.: Conducting polymer coated carbon surfaces and biosensor applications. Progress in Organic Coatings, **66**, 337–358 (2009).
DOI: 10.1016/j.porgcoat.2009.08.014

[18] Xia L., Wei Z., Wan M.: Conducting polymer nanostructures and their application in biosensors. Journal of Colloid and Interface Science, **341**, 1–11(2010).
DOI: 10.1016/j.jcis.2009.09.029

[19] Tourillon G., Garnier F.: Structural effect on the electrochemical properties of polythiophene and derivatives. Journal of Electroanalytical Chemistry and Interfacial Electrochemistry, **161**, 51–58 (1984).
DOI: 10.1016/S0022-0728(84)80249-1

[20] Kumar A., Welsh D. M., Morvant M. C., Piroux F., Abboud K. A., Reynolds J. R.: Conducting poly(3,4-alkylenedioxythiophene) derivatives as fast electrochromics with high-contrast ratios. Chemistryl of Materials, **10**, 896–902 (1998).
DOI: 10.1021/cm9706614

[21] Gaupp C. L., Welsh D. M., Rauh R. D., Reynolds J. R.: Poly(ProDOT-Et2): A high-contrast, high-coloration efficiency electrochromic polymer. Macromolecules Rapid Communications, **23**, 885–889 (2002).
DOI: 10.1002/1521-3927(20021001)23:15<885::AID-MARC885>3.0.CO;2-X

[22] Sinha J., Sahoo R., Kumar A.: Processable, regioregular, and 'click'able monomer and polymers based on 3,4-propylenedioxythiophene with tunable solubility. Macromolecules, **42**, 2015–2022 (2009).
DOI: 10.1021/ma802289j

[23] Mishra S. P., Sahoo R., Ambade A. V., Contractor A. Q., Kumar A.: Synthesis and characterization of functionalized 3,4-propylenedioxythiophene and its derivatives. Journal of Materials Chemistry, **14**, 1896–1900 (2004).
DOI: 10.1039/B404600E

[24] Kumar N. A., Kim S. H., Cho B. G., Lim K. T., Jeong Y. T.: Surface functionalization of multiwalled carbon nanotubes with poly(3,4-propylenedioxythiophene) and preparation of its random copolymers: New hybrid materials. Colloid and Polymer Science, **287**, 97–102 (2009).
DOI: 10.1007/s00396-008-1945-4

[25] Oberlin A.: Carbonization and graphitization. Carbon, **22**, 521–541 (1984).
DOI: 10.1016/0008-6223(84)90086-1

[26] Ates M., Sarac A. S.: Electrochemical impedance spectroscopy of poly[carbazole-co-N-p-tolylsulfonyl pyrrole] on carbon fiber microelectrodes, equivalent circuits for modelling. Progress in Organic Coatings, **65**, 281–287 (2009).
DOI: 10.1016/j.porgcoat.2008.12.007

[27] Sarac A. S., Sezgin S., Ates M., Turhan C. M.: Electrochemical impedance spectroscopy and morphological analyses of pyrrole, phenylpyrrole and methoxyphenylpyrrole on carbon fiber microelectrodes. Surface Coatings Technology, **202**, 3997–4005 (2008).
DOI: 10.1016/j.surfcoat.2008.02.007

[28] Sarac A. S., Sezgin S., Ates M., Turhan C. M., Parlak E. A., Irfanoglu B.: Electrochemical impedance spectroscopy of poly(N-methyl pyrrole) on carbon fiber microelectrodes and morphology. Progress in Organic Coatings, **62**, 331–335 (2008).
DOI: 10.1016/j.porgcoat.2008.01.016

[29] Tezcan C., Sarac A. S.: Electrochemical copolymerization of 3,4-Ethylenedioxythiophene and *N*-Phenylsulfonyl Pyrrole: Morphologic, spectroscopic, electrochemical characterizations. Journal of the Electrochemical Society, **157**, 99-105 (2010).
DOI: 10.1149/1.3490420

[30] Sarac A. S., Ates M., Parlak E. A.: Comparative study of chemical and electrochemical copolymerization of N-methylpyrrole with N-ethylcarbazole spectroscopic and cyclic voltammetric analysis. International Journal of Polymeric Materials, **54**, 883–897 (2005).
DOI: 10.1080/009140390504861

[31] Sarac A. S., Ates M., Parlak E. A.: Electrolyte and solvent effects of electrocoated polycarbazole thin films on carbon fiber microelectrodes. Journal of Applied Electrochemistry, **36**, 889–898 (2006).
DOI: 10.1007/s10800-006-9145-8

[32] Sarac A. S., Serantoni M., Tofail S. A. M., Henry J., Cunnane V. J., McMonagle J. B.: Characterisation of nanosize thin films of electrografted N-vinylcarbazole copolymers (P[NVCz–co-VBSA] and P[NVCz–co-3-MeTh]) onto carbon fibre: AFM, XPS, and Raman spectroscopy. Applied Surface Science, **243**, 183–198 (2005).
DOI: 10.1016/j.apsusc.2004.09.095

[33] Sarac A. S., Serantoni M., Tofail S. A. M., Cunnane V. J.: Morphological and spectroscopic analyses of poly[N-vinylcarbazole-co-vinylbenzenesulfonic acid] copolymer electrografted on carbon fiber: The effect of current density. Applied Surface Science, **229**, 13–18 (2004).
DOI: 10.1016/j.apsusc.2004.02.005

[34] Popkirov G. S., Barsoukov E., Schindler R. N.: Investigation of conducting polymer electrodes by impedance spectroscopy during electropolymerization under galvanostatic conditions. Journal of Electroanalytical Chemistry, **425**, 209–216 (1997).
DOI: 10.1016/S0022-0728(96)04965-0

[35] Deslouis C., Musiani M. M., Tribollet B., Vorotyntsev M. A.: Comparison of the AC ımpedance of conducting polymer films studied as electrode-supported and freestanding membranes. Journal of Electrochemical Society, **142**, 1902–1908 (1995).
DOI: 10.1149/1.2044212

[36] Láng G., Inzelt G.: Some problems connected with impedance analysis of polymer film electrodes: Effect of the film thickness and the thickness distribution. Electrochimica Acta, **36**, 847–854 (1991).
DOI: 10.1016/0013-4686(91)85284-E

[37] Parsons R.: The electrical double layer: Recent experimental and theoretical developments. Chemical Reviews, **90**, 813–826 (1990).
DOI: 10.1021/cr00103a008

[38] Vorotyntsev M. A., Badiali J-P., Inzelt G.: Electrochemical impedance spectroscopy of thin films with two mobile charge carriers: Effects of the interfacial charging. Journal of Electroanalytical Chemistry, **472**, 7–19 (1999).
DOI: 10.1016/S0022-0728(99)00253-3

[39] Abidian M. R., Martin D. C.: Experimental and theoretical characterization of implantable neural microelectrodes modified with conducting polymer nanotubes. Biomaterials, **29**, 1273–1283 (2008).
DOI: 10.1016/j.biomaterials.2007.11.022

[40] Bobacka J., Grzeszczuk M., Ivaska A.: Electron transfer at conducting polymer film electrodes: Mechanism and kinetics of ferrocene oxidation at poly(3-octylthiophene). Journal of Electroanalytical Chemistry, **427**, 63–69 (1997).
DOI: 10.1016/S0022-0728(96)05023-1

[41] Bobacka J., Lewenstam A., Ivaska A.: Electrochemical impedance spectroscopy of oxidized poly(3,4-ethylenedioxythiophene) film electrodes in aqueous solutions. Journal of Electroanalytical Chemistry, **489**, 17–27 (2000).
DOI: 10.1016/S0022-0728(00)00206-0

[42] Mansfeld F. Kendig M. W.: Evaluation of anodized aluminum surfaces with electrochemical ımpedance spectroscopy. Journal of Electrochemical Society, **135**, 828–833 (1988).
DOI: 10.1149/1.2095786

[43] Khaled K. F.: The inhibition of benzimidazole derivatives on corrosion of iron in 1 M HCl solutions. Electrochimica Acta, **48**, 2493–2503 (2003).
DOI: 10.1016/S0013-4686(03)00291-3

[44] Carnot A., Frateur I., Zanna S., Tribollet B., Dubois-Brugger I., Marcus P.: Corrosion mechanisms of steel concrete moulds in contact with a demoulding agent studied by EIS and XPS. Corrosion Science, **45**, 2513–2524 (2003).
DOI: 10.1016/S0010-938X(03)00076-3

[45] Aziz I., Zhang Q., Xiang M.: Using EIS to evaluate anti-corrosion properties of the SiCp/5A06 aluminium MMC treated by cerium conversion coatings. Journal of Rare Earths, **28**, 109–116 (2010).
DOI: 10.1016/S1002-0721(09)60062-4

[46] Simões A. M., Fernandes J. C. S.: Studying phosphate corrosion inhibition at the cut edge of coil coated galvanized steel using the SVET and EIS. Progress in Organic Coatings, **69**, 219–224 (2010).
DOI: 10.1016/j.porgcoat.2010.04.022

[47] Farelas F., Galicia M., Brown B., Nesic S., Castaneda H.: Evolution of dissolution processes at the interface of carbon steel corroding in a CO_2 environment studied by EIS. Corrosion Science, **52**, 509–517 (2010).
DOI: 10.1016/j.corsci.2009.10.007

[48] de Lacy Castello B. P. J., Evans P., Guernion N., Ratcliffe N. M., Sivanand P. S., Teare G. G.: The synthesis of a number of 3-alkyl and 3-carboxy subtituted pyrroles: Their chemical polymerisation onto poly (vinylidene fluoride) membranes and their use as gas senstive resistor. Synthetic Metals, **114**, 181–188 (2000).
DOI: 10.1016/S0379-6779(00)00250-2

[49] Janosik T., Shirani H., Whalstörm N., Malky I., Stensland J., Bergman J.: Efficient sulfonation of 1-phenylsulfonyl-1*H*-pyrroles and 1-phenylsulfonyl-1*H*-indoles using chlorosulfonic acid in acetonitrile. Tetrahedron, **62**, 1699–1707 (2006).
DOI: 10.1002/chin.200624113

[50] Li X-G., Huang M-R., Duan W., Yang Y-L.: Novel multifunctional polymers from aromatic diamines by oxidative polymerizations. Chemical Reviews, **102**, 2925–3030 (2002).
DOI: 10.1002/chin.200246251

[51] Lu Q. F., Huang M. R., Li X. G.: Synthesis and heavy-metal-ion sorption of pure sulfophenylenediamine copolymer nanoparticles with intrinsic conductivity and stability. Chemistry A: European Journal, **13**, 6009–6018 (2007).
DOI: 10.1002/chem.200700233

[52] Malinauskas A.: Chemical deposition of conducting polymers. Polymer, **42**, 3957–3972 (2001).
DOI: 10.1016/S0032-3861(00)00800-4

[53] Prévost V., Petit A., Pla F.: Studies on chemical oxidative copolymerization of aniline and o-alkoxysulfonated anilines: I. Synthesis and characterization of novel self-doped polyanilines. Synthetic Metals, **104**, 79–87 (1999)
DOI: 10.1016/S0379-6779(99)00009-0

[54] Fu G. D., Zhao J. P., Sun Y. M., Kang E. T., Neoh K. G.: Conductive hollow nanospheres of polyaniline via surface-ınitiated atom transfer radical polymerization of 4-vinylaniline and oxidative graft copolymerization of aniline. Macromolecules, **40**, 2271–2275 (2007).
DOI: 10.1021/ma0613988

[55] Li X-G., Duan W., Huang M-R., Rodriguez L. N. J.: Electrocopolymerization of *meta*-phenylenediamine and *ortho*-phenetidine. Reactive and Functional Polymers, **62**, 261–270 (2005).
DOI: 10.1016/j.reactfunctpolym.2005.01.001

[56] Ocampo C., Alemán C., Oliver R., Arnedillo M. L., Ruiz O., Estrany F.: Copolymers of N-methylpyrrole and 3,4-ethylenedioxythiophene: Structural, physical and electronic properties. Polymer International, **56**, 803–809 (2007).
DOI: 10.1002/pi.2213

[57] Lee K-M., Chen P-Y., Hsu C-Y., Huang J-H., Ho W-H., Chen H-C., Ho K-C.: A high-performance counter electrode based on poly(3,4-alkylenedioxythiophene) for dye-sensitized solar cells. Journal of Power Sources, **188**, 313–318 (2009).
DOI: 10.1016/j.jpowsour.2008.11.075

[58] Saraç A. S., Bardavit Y.: Electrografting of copolymer of poly[N-vinylcarbazole-co-styrene] and poly[N-vinylcarbazole-co-acrylonitrile] onto carbon fiber: Cyclovoltammetric (CV), spectroscopic (Uv-Vis, FT-IR-ATR), and morphological study (SEM). Progress in Organic Coatings, **49**, 85–94 (2004).
DOI: 10.1016/j.porgcoat.2003.08.018

[59] Johnsson B., Löfås S., Lindquist G.: Immobilization of proteins to a carboxymethyldextran-modified gold surface for biospecific interaction analysis in surface plasmon resonance sensors. Analytical Biochemistry, **198**, 268–277 (1991).
DOI: 10.1016/0003-2697(91)90424-R

[60] Girija T. C., Sangaranarayanan M. V.: Investigation of polyaniline-coated stainless steel electrodes for electrochemical supercapacitors. Synthetic Metals, **156**, 244–250 (2006).
DOI: 10.1016/j.synthmet.2005.12.006

eXPRESS Polymer Letters Vol.5, No.6 (2011) 506–515
Available online at www.expresspolymlett.com
DOI: 10.3144/expresspolymlett.2011.49

New polyelectrolyte complex particles as colloidal dispersions based on weak synthetic and/or natural polyelectrolytes

M. Mihai[*], *C. A. Ghiorghiţă, I. Stoica, L. Niţă, I. Popescu, Ghe. Fundueanu*

'Petru Poni' Institute of Macromolecular Chemistry, 41A Grigore Ghica Voda Alley, 700487 Iasi, Romania

Received 13 October 2010; accepted in revised form 16 December 2010

Abstract. This study aims to evidence the formation of stable polyelectrolyte complex particles as colloidal dispersions using some weak polyelectrolytes: chitosan and poly(allylamine hydrochloride) as polycations and poly(acrylic acid) (PAA) and poly(2-acrylamido-2-methylpropanesulfonic acid – co – acrylic acid) (PAMPSAA) as polyanions. Polyelectrolyte complex particles as colloidal dispersion were prepared by controlled mixing of the oppositely charged polymers, with a constant addition rate. The influences of the polyelectrolytes structure and the molar ratio between ionic charges on the morphology, size, and colloidal stability of the complex particles have been deeply investigated by turbidimetry, dynamic light scattering and atomic force microscopy. A strong influence of polyanion structure on the values of molar ratio n^-/n^+ when neutral complex particles were obtained has been noticed, which shifts from the theoretical value of 1.0, observed when PAA was used, to 0.7 for PAMPSAA based complexes. The polyions chain characteristics influenced the size and shape of the complexes, larger particles being obtained when chitosan was used, for the same polyanion, and when PAMPSAA was used, for the same polycation.

Keywords: *nanomaterials, polyelectrolyte complex, weak polyelectrolyte, dynamic light scattering, atomic force microscopy*

1. Introduction

Oppositely charged polymers form polyelectrolyte complexes (PEC) after mixing of their solutions [1]. PECs are of interest due to their facile preparation and responsiveness to environmental stimuli. Moreover, using water as a solvent, PECs are attractive for biomedical applications. Examples include controlled drug delivery systems, enzyme and DNA carriers, surface modification of medical implants, membranes for cell culture and growth, biosensors, and nanostructured materials [2–5].

At relatively low concentrations and when one of the components is taken in excess, PEC formation can lead to stable colloidal dispersions [6–12]. The characteristics of the polyelectrolyte components (molecular weight, nature of ionic groups, charge density, and architecture) and the solvent (ionic strength, pH) determine the internal structure of the particles. The level of aggregation is dominantly controlled by the concentration of the polymer solution. PECs as colloidal dispersions are interesting for industrial applications as coatings, auxiliary products in paper manufacturing, and for special purposes in biotechnology and medicine [13–15]. When weak polyelectrolytes are involved in PEC preparation, the molar ratio between charges when neutral complex particles were obtained is strongly influenced by the pH value of polyions solutions, conferring an amphoteric character to thePEC aggregates [16]. The amphoteric behavior of the PEC

[*]Corresponding author, e-mail: marcelas@icmpp.ro

particles, namely the sign of net surface charge, is determined by the positive or negative charges on the chain loops and chain ends on the particle surface.

Chitosan (CS) is a natural amino-polysaccharide (copolymer of β-(1-4) linked 2-acetamido-2-deoxy-D-glycopyranose and 2-amino-2-deoxy-D-glycopyranose) produced by deacetylation of chitin from crustaceans' exoskeletons and fungal cell walls [17]. Sustainable interest in the biomedical application of chitosan to discourage bacterial adhesion and implant infection is stimulated strongly by its non-toxicity [18], biodegradability [19], and strong antibacterial properties [20]. It has been already shown that polyelectrolyte complexes and multilayers based on chitosan, by virtue of their biocompatibility, have valuable biomedical applications such as membranes for dialysis, packaging, coatings and wounds dressing, polyelectrolyte complex beads for controlled delivery of proteins, drugs, vaccines [21–28]. Promising results were obtained in application of chitosan based nonstoichiometric PECs as flocculants [29].

Our previous studies dealt with the preparation of PECs nanoparticles as stable colloidal dispersions using strong synthetic polyanions and synthetic or natural (CS) polycations. Also, the factors (polyions structure and molar mass, molar ratio between charges, addition order, titrant addition rate) which influence particles size, morphology, and storage stability were investigated [30–33]. This study aims to obtain PECs as colloidal dispersion using some weak polyelectrolytes: CS and poly(allylamine hidrochloride) (PAH) as polycations and poly(acrylic acid) (PAA) and poly(2-acrylamido-2-methylpropanesulfonic acid – co – acrylic acid) (PAMPSAA) as polyanions. PAA and PAH, which have identical polymer backbones and differ only in the ionic side group, were chosen as model weak polymers for PEC formation. The influence of polyelectroytes structure and the molar ratio between ionic charges on the complex particles morphology, size, and colloidal stability have been deeply investigated by turbidimetry, dynamic light scattering (DLS) and atomic force microscopy (AFM).

2. Materials and methods

2.1. Materials

CS sample was kindly provided by Yaizu Suisankagaku Ind. (Shizuoka, Japan), as powder and was used without further purification. The viscometric average molar masses of CS sample, M_v = 80 000 g/mol, was estimated using Equation (1) [34]:

$$[\eta] = 6.95 \cdot 10^{-4} \cdot M_v^{0.81} \quad (1)$$

The intrinsic viscosity of CS solution in 0.3 M CH_3COOH – 0.2 M CH_3COONa (1:1, v/v) was measured with an Ubbelohde viscometer at 25±0.1°C.

The deacetylation degree was determined by two metods:

– by potentiometric titration, according to ref. [35], dissolving CS in a known excess of HCl and performing potentiometric titration with 0.1 N NaOH, using an all-purpose titrator 716DMS Titrino, Metrohm (Herisau, Switzerland), equipped with a dosing unit and a combined glass electrode;
– from ^{1}H-NMR spectra recorded on Bruker NMR model Avance DRX 400 (400 MHz) spectrometer (Bruker, Switzerland). The CS sample was dissolved in D_2O and, to avoid the overlap between the signals of acetic acid and acetyl groups, some drops of HCl have been added to solubilize the polymer. The deacetylation degree was calculated as described before by Hirai *et al*. [36].

A deacetylation degree of about 82.5% was determined by both methods.

PAH, purchased from Aldrich (code no: 283215), with M_w = 15 000 g/mol, was used as received. PAA with a molar mass M_w = 70 000 g/mol was synthesized and purified according to ref. [37]. The copolymer PAMPSAA, which contains 55 mol% of 2-acrylamido-2-methylpropanesulfonic acid (AMPS) and 45 mol% of acrylic acid (AA), was synthesized and purified according to ref. [38]. The intrinsic viscosity of the copolymer, determined in 1M NaCl at 25°C, was $[\eta]$ = 0.72 dl/g.

2.2. Preparation of polyelectrolyte complexes as colloidal dispersions

CS solution was prepared in 1 vol% acetic acid solution, and 0.02 M NaCl. PAH and polyanions

solutions, were prepared by dissolution of appropriate amounts in 0.02 M NaCl aqueous solution. The concentration of polycations solution was $5 \cdot 10^{-4}$ M and that of polyanions solutions was $5 \cdot 10^{-3}$ M.

Dispersions of PECs were prepared at room temperature, by mixing the solutions of oppositely charged polyelectrolytes in appropriate proportions. The amount of polycation was kept constant within a complex series, while the amount of polyanion was varied according to the desired mixing molar ratio, n^-/n^+. The polyanion solution was added dropwise to the polycation solution, under magnetic stirring. A constant addition rate of 3.8 ml polyanion/(ml polycation·h) was used as optimum addition rate, taking into account the complex morphology and the preparation speed, according to our previous investigations on the formation of PECs as colloidal dispersion from synthetic polycations and polyanions [30–33]. After mixing, the formed dispersions were stirred 60 min and were characterized after 24 h, if other conditions were not specified.

2.3. Characterization methods

Polyelectrolyte and potentiometric titrations were performed with the particle charge detector Mütek PCD 03 (BTG Instruments GmbH, Herrsching, Germany). The particle charge detector includes a Teflon piston, which moves up and down in a cylindrical Teflon cell containing the polyelectrolyte solution in the slit between the cylinder and piston. Displacement of the ion cloud around the polymer chains which are stuck on the porous wall of Teflon cylinder creates the streaming potential (measured in mV) at the electrode pair located in upper and bottom parts of the cell. The measured streaming potential is linearly correlated with the charge density of polyelectrolytes and it becomes zero in case of charge neutrality. The concentration of the charged groups of each solution was evaluated by titration with a standard solution of a strong oppositely charged polyelectrolyte, poly(sodium ethylenesulfonate) or poly(diallyldimethyl-ammonium chloride), with a concentration of 10^{-3} M. The concentration of the charged groups in the examined solution was calculated from the amount of standard solution needed to reach the zero value of the streaming potential. All measurements were made at room temperature. Potentiometric titration was carried out between pH 2 and 10, using 0.1 M NaOH and HCl, respectively.

The turbidity of the complex dispersions was characterized by the optical density at $\lambda = 500$ nm (OD_{500}), with a Lambda 900 spectrometer (Perkin-Elmer Co. Ltd., Massachusetts, USA), using deionized water to establish the baseline. At this wavelength, the used polyelectrolytes do not absorb. Optical density results were expressed as the average of at least three independent measurements.

DLS measurements of PEC dispersions were carried out using a Zetasizer 3000 (Malvern Instruments, Worcestershire, UK) equipped with a 10 mW He-Ne laser (633 nm) as light source. The measurements were performed at a scattering angle of 90°, and the reported results are the average of two DLS independent measurements. The samples were kept at a constant temperature of 25°C during all experiments. DLS measures the light diffusion in particle dispersions, which can be interpreted using the Stokes-Einstein equation (Equation (2)) to yield the particle average hydrodynamic diameter, D_h:

$$D_h = \frac{k_B T}{3\pi\eta_s D} \tag{2}$$

where k_B is the Boltzmann constant, T is the absolute temperature (298 K), η_s is the dynamic viscosity of the solvent (for water 0.8872 cP), and D is the z-average translational diffusion coefficient. To get information about the size distribution of PEC particles, the size polydispersity was also included in the interpretation.

The shapes of PEC particles were examined by means of a SPM Solver PRO-M AFM (NT-MTD Co. Zelenograd, Moscow, Russia), using a high resolution 'Golden' silicon NSG10/Au/50 cantilever with an Au conductive coating. The topographic images were obtained in tapping mode and were repeated on different areas of the same sample. Prior to use, the silicon wafers substrates were carefully cleaned in two steps: first in 'piranha solution' followed by intensive rinsing with deionized water and second with the mixture NH_4OH/H_2O_2/deionized water, at 70°C, in ultrasonic bath, intensively rinsed with water and finally dried under a nitrogen flow. The clean silicon wafers substrates were immersed in PEC dispersions, identical with those used for DLS, for 20 min, then three times each

1 min in distilled water and finally air-dried at room temperature (in a dust-free environment) for 48 h.

3. Results and discussion

3.1. Potentiometric titration of polyelectrolytes

Although the value of streaming potential depends on numerous factors and can not be used as an absolute value (in the same way as ζ-potential), the method of colloidal titration with streaming potential detection is useful to determine the point of zero charge (*pzc*) in solutions of polyelectrolytes and colloidal dispersions. The *pzc* was considered to be the numeric value of pH where the streaming current is zero mV. When the pH is lower than the *pzc* value, the system is below the *pzc*. Below the *pzc*, the acidic water donates more protons than hydroxide groups, and so the adsorbent surface is positively charged. Conversely, above *pzc* the basic water donates more hydroxide groups than protons and the adsorbent surface is negatively charged. Figure 1 shows the potentiometric titrations curves for all polymers involved in this study, in the presence or absence of NaCl.

As it is already known, the net charge on the weak polyelectrolyte molecules is affected by pH of their surrounding environment. The polyanions used in this study contain carboxyl groups. Below *pzc*, the carboxyl group can undergo protonation ($–COOH_2^+$) at either the carbonyl oxygen or at the hydroxyl oxygen, and a small positive potential was obtained. Above *pzc*, located at pH 1.8 for PAMPSAA and 2.2 for PAA (Figure 1), the presence of hydroxyl ions induced the dissociation of carboxyl groups ($–COO^–$). Thus, above the *pzc* the polyanions had negative streaming potential. At *pzc* the ionization degree of polyanions is zero; e.g., the ionization degree of PAA at pH = 2.2 is 0.007, taking into account that pKa of PAA is close to 4.3.

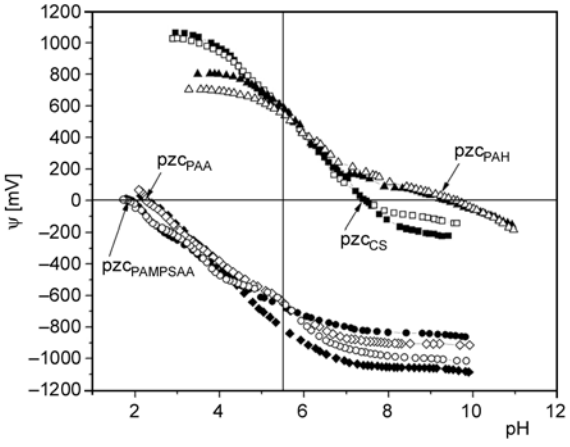

Figure 1. Potentiometric titration of CS (square), PAH (triangle), PAA (diamond), PAMPSAA (circles) in salt-free aqueous solution (close symbols), and 0.02 M NaCl aqueous solution (open symbols); *pzc* = point of zero charges.

On the other hand, below *pzc*, in the presence of hydronium ions, the primary amino groups ($–NH_2$) of the polycations PAH and CS can be protonated ($–NH_3^+$), leading to *pzc* around pH 7.4 for CS and 9.2 for PAH. Primary amines have protic hydrogens and therefore possess a small degree of acidity. Thus, above *pzc* a proton from amine group can be dissociated ($–NH^–$), due to the strongly basic medium and a negative streaming potential is obtained.

In the presence of a small amount of low molecular weight salt (0.02 M NaCl), no significant changes in the shape of titration curves are observed, and the *pzc* remains almost unchanged (Figure 1).

Taking into account the results obtained by potentiometric titration, for PECs preparation the pH value of polyions solutions was adjusted to 5.5, to ensure a similar ionization degree of the complementary polyelectrolytes, suggested by the complementary streaming potential values at this pH: ~600 mV for polycations and ~–600 mV for polyanions.

3.2. Preparation and characterization of PECs

3.2.1. Turbidimetric titration

The formation of colloidal PECs between all studied polyelectrolyte pairs was followed firstly by turbidimetric titration, OD_{500}, as a function of the mixing ratio $n^–/n^+$, i.e., the molar ratio between anionic and cationic units (Figure 2).

It is well known that the turbidity values reflect the influence of some parameters that characterize the PECs dispersions such as concentration, size, shape and polydispersity [6–8, 14, 30, 31]. Therefore, the increase of OD_{500} values with the increase of molar ratio between charges $n^–/n^+$, observed in Figure 2, could be assigned also to the increase of the sizes and polydispersities of the complex particles.

As it is already known, the values of molar ratio $n^–/n^+$ corresponding to neutral PECs particles $(n^–/n^+)_n$ is strongly influenced by the structure of the complementary polyelectrolytes, namely by their structural ability to intrinsic compensate their ionic

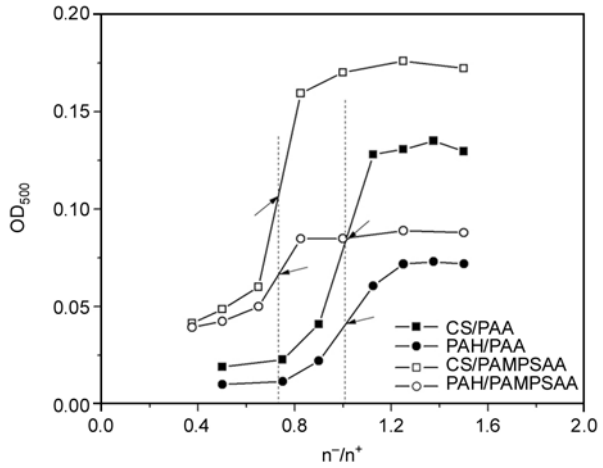

Figure 2. OD_{500} values as a function of the molar ratio between charges, n^-/n^+. The values are the mean of three independent experiments that deviated 0–7%. The continuous lines are 'hand-drawn' lines.

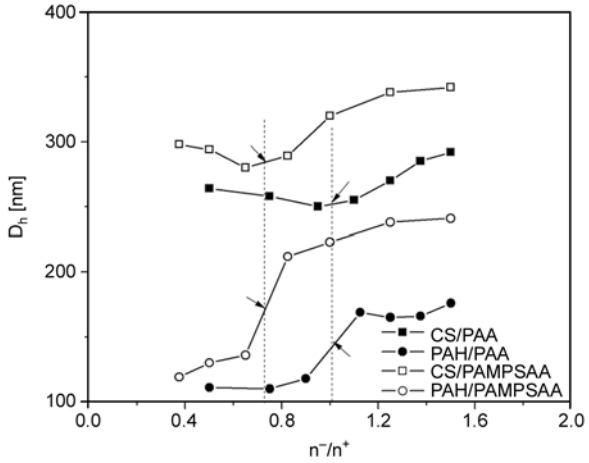

Figure 3. D_h of the PEC dispersions as a function of the molar ratio between charges (n^-/n^+). The values are the mean of three independent experiments that deviated 0–7%. The continuous lines are 'hand-drawn' lines.

charges (polymer/polymer ion pairs) [39]. The values of molar ratio $(n^-/n^+)_n$ was considered as the abscissa value of the rising curve corresponded to the one-half of the maximum of OD_{500}. As Figure 2 shows, neutral complex particles were obtained at a molar ratio between charges of around $n^-/n^+ = 1$, when PAA was the polyanion, and around $n^-/n^+ = 0.7$ when PAMPSAA was used, irrespective the polycation structure. A deviation of the endpoint of polyelectrolyte interactions to lower values of $(n^-/n^+)_n$ was also observed for other studied systems [31] and was ascribed to the difficulties in the intrinsic charge compensation between the complementary polyions.

For the same polyanion, higher values were obtained when CS was the polycation, along the whole range of molar ratio, n^-/n^+ (Figure 2). These results may be ascribed to the lower flexibility of CS chain (which has a semi-rigid chain unlike the synthetic polycation which is flexible), which probably induced the formation of particles with higher size, reflected by higher OD_{500} values. For the same polycation, the OD_{500} values were higher when PAMPSAA was used, comparative with PAA.

3.2.2. Dynamic light scattering

DLS is a suitable method to monitor the formation of PEC particles as a function of the mixing molar ratio n^-/n^+. Figure 3 shows the DLS profiles on the PEC formation between CS and PAH, as starting polycations, and PAA and PAMPSAA as added polyanions.

The shape of the DLS curves was clearly influenced by the complementary polyelectrolytes structure. Thus, for PAH based complexes, D_h values slowly increased up to about 0.9 and 0.6 when PAA and PAMPSAA was used, respectively, abruptly increased around $(n^-/n^+)_n$, and remains almost constant after that. For CS based PECs, a slight decrease in the particle sizes was evident when CS was in excess, i.e. from 300 to 280 nm when PAMPSAA was used and from 265 to 248 nm when PAA was the added polyanion (Figure 3). This behavior suggests that below $(n^-/n^+)_n$ the addition of polyanions allows both the formation of new particles, evidenced by the slow increase of the OD_{500} values (Figure 2), and also their rearrangement toward more compact structures. At values of molar ratio n^-/n^+ higher than that corresponding to $(n^-/n^+)_n$, the inter-particles aggregation took place, leading to the monotonous increase of the complex particles sizes. It seems that this kind of behavior is characteristic for CS based systems, as it was previously observed for PECs prepared with other polyanions [29, 33, 40].

DLS results confirm the values of molar ratio $(n^-/n^+)_n$, observed in Figures 2, at $n^-/n^+ = 1$, when PAA was the polyanion, and around $n^-/n^+ = 0.7$ when PAMPSAA was used, irrespective the polycation structure. When PAMPSAA was used as polyanion, the particle sizes after the molar ratio $(n^-/n^+)_n$ were higher than the sizes of the PEC formed with PAA as polyanion, irrespective of polycation nature

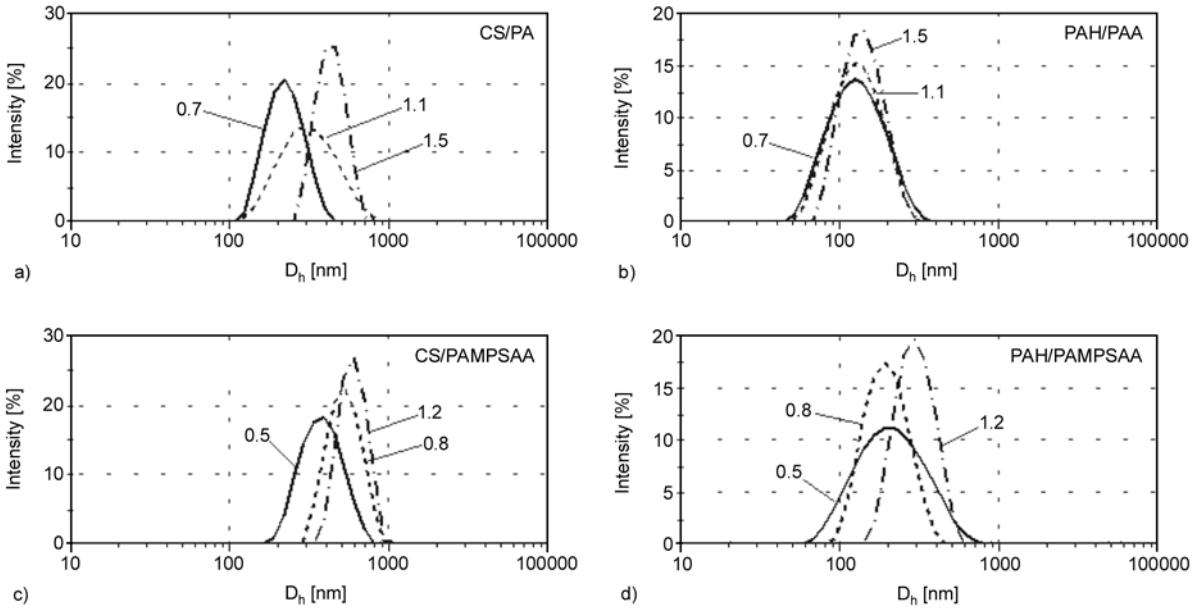

Figure 4. The particle size distribution analysis by intensity, obtain by DLS, for all studied systems and some selected molar ratios between charges

and molar ratio between charges. The copolymer contains 55% AMPS units, with the ionic group attached by a longer spacer to the macromolecular backbone, with high flexibility, and a higher ability to compensate the ionic charges of the polycation. Thus, probably part of the AA and CS ionic sites are hindered, and remain extrinsic compensated by small ions, leading to values of molar ratio $(n^-/n^+)_n$ lower than 1.0.

To evidence the influence of polyions structure on the size and polydispersity of PECs, the intensity of particle size distribution, determined by DLS, was also represented for all studied systems and some selected molar ratio between charges (Figure 4).

As Figure 4 shows, unimodal size distribution was observed for all studied systems, irrespective of the molar ratio between charges. At the same time, high values of polydispersity were observed at values of molar ratio n^-/n^+ below and around $(n^-/n^+)_n$, the highest values being obtained for the PAH/PAMPSAA pair. Moreover, a small decrease of the intensity of particle size distribution at $n^-/n^+ = 1.2$ was evident for all studied samples. This behavior suggests that the secondary aggregation by inter-particles interactions was not so fast and took place only when the polyanion was in excess, leading to a monotonous increase of the complex particles sizes (Figure 3).

3.2.3. Atomic force microscopy

In Figure 5, the AFM images of the PEC dispersion formed between all the studied polyions, at a molar ratio between charges of 1.2 are presented.

As Figure 5 shows, the adsorption of PEC particles on silicon wafers surface, resulted in an inhomogeneous mixture of smaller and bigger particles, for the studied samples. This is not surprising since the PEC particles showed a high polydispersity, evidenced by DLS measurements (Figure 4). Moreover, the AFM images confirm the results presented in Figure 3, namely bigger particle sizes can be observed for PECs prepared with CS as compared to PAH for the same polyanion (Figures 5a and c), and with PAMPSAA as compared to PAA for the same polycation (Figures 5b and d).

The structure of polyanion strongly influenced the PECs particles shape: with PAA almost spherical particles were formed, but with PAMPSAA an irregular shape is evident, irrespective of polycation structure, probably due to the irregular compensation of the copolymer ionic sites.

The profiles of some selected particles of each sample (marked with a white line in Figures 5a–d) are presented in Figure 6.

Even if the interaction with the silica surface could induce conformational changes in the individual PEC particles, due to electrostatic interactions dur-

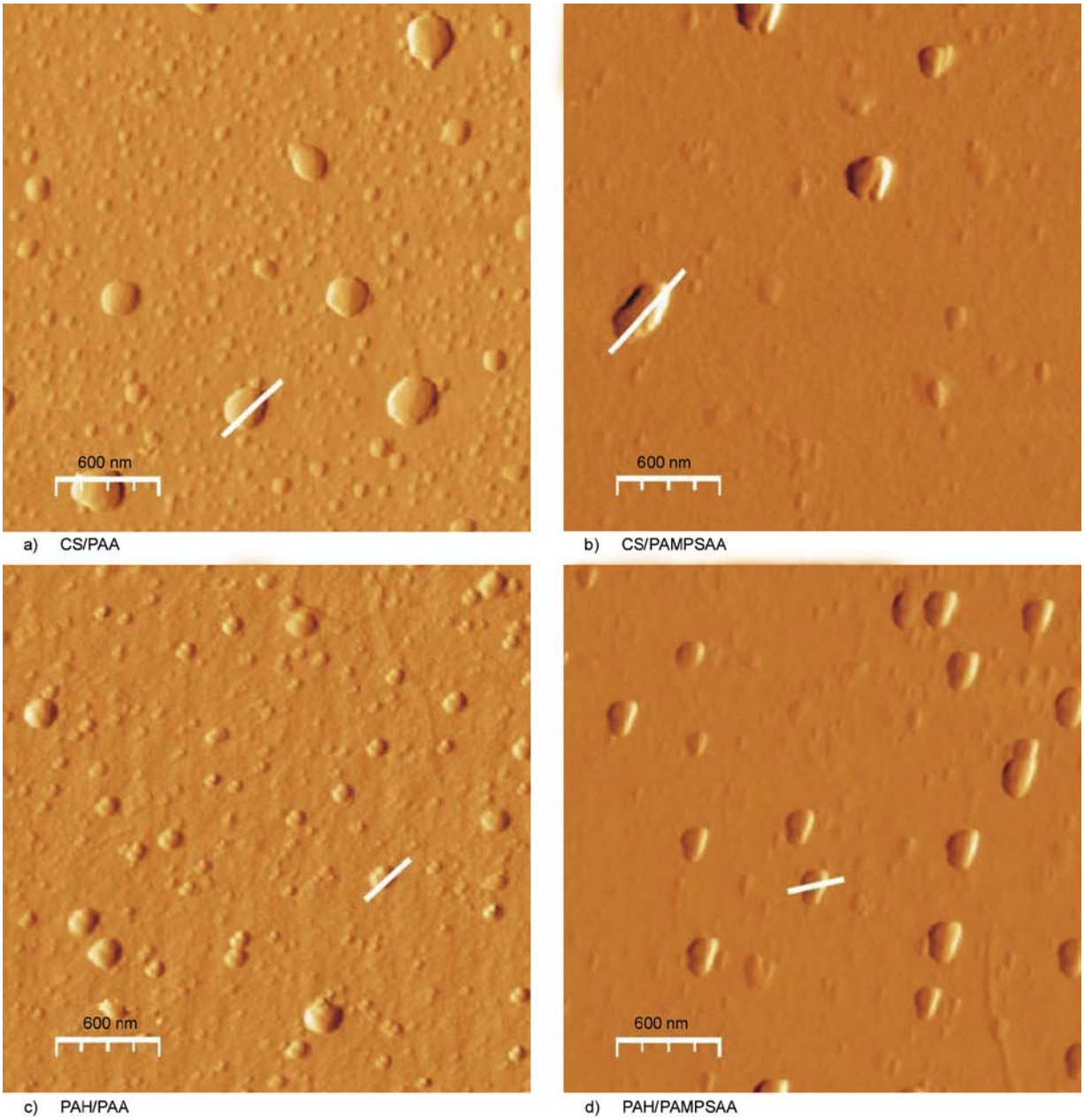

Figure 5. Tapping mode amplitude AFM images of the complex particles at a molar ratio between charges of 1.2, adsorbed on the silicon wafers

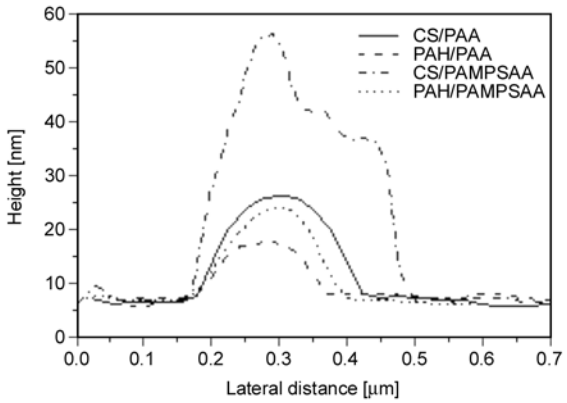

Figure 6. AFM profiles of some selected PEC particles (see white lines labeled particles in Figure 5) adsorbed on silicon wafers

ing adsorption, after the air-drying procedure, the PECs particles still display 3D structures, the values of particles height increasing with their diameter, irrespective of the polyion pair involved in their preparation. Moreover, the values of the particles height were in agreement with the hydrodynamic diameter values (Figure 3), the smallest values being obtained for PAH/PAA complex particles and the highest for CS/PAMPSAA particles.

3.3. Colloidal stability

When the complexation takes place between polyelectrolytes having significantly different molecular weights, weak ionic groups, in nonstoichiometric mixing ratios and under dilute conditions, the reaction mixture develops a colloidal, Tyndall effect. This behavior is ascribed to PECs structure, consisting of a neutral core surrounded by the polyelectrolyte in excess, which stabilizes PECs particles against aggregation, to provide practical nanoscale and microscale products [2, 6, 9, 11]. The excess polyelectrolyte dictates the conditions for stability in different medium conditions. A very important characteristic of the PECs as colloidal dispersion is their colloidal stability. Storage colloidal stability of PECs is very sensitive to the structure of the complementary polyions, to the molar ratio between charges, i.e., the complex is closer or further to the molar ratio $(n^-/n^+)_n$, to the polyions addition order, especially when the complementarities of oppositely charged polyions is disturbed by their structure, and very much to the titrant addition rate, as it was previously demonstrated for PECs prepared with strong polyanions [31–33]. Therefore, the particle sizes, D_h, measured after 24 h from preparation were compared with those measured after two weeks of storage at room temperature (~22°C), without stirring (data not shown here). A high colloidal stability, i.e., low changes in the particle sizes, was found for PAH based PECs, along the whole range of investigated molar ratios between charges. As concerns the CS based PECs, when the polyanion is in excess the values of the particle sizes only slightly changed, the differences being more significant when CS was in excess, compared with those measured after 24 h, the increase of the particles size being in the range of 15–30 nm. These differences can be ascribed to the possible interactions between the primary aggregates, accompanied by rearrangements of chains and the formation of compact particles with higher sizes.

4. Conclusions

Two polyanions, PAA and a copolymer of AMPS with AA, and two weak polycations, PAH and CS, were used in the preparation of some PEC dispersions. Turbidimetry, DLS and AFM have been used as complementary methods to describe the characteristics of the PEC dispersions as a function of the polyions structure and the ratio between charges.

The value of molar ratio $(n^-/n^+)_n$ was clearly influenced by the polyanion structure, and was located at about 1.0 and 0.7 when PAA and PAMPSAA were respectively involved in the complexes preparation, irrespective of the polycation structure. The deviation of the endpoint of polyelectrolyte interactions to lower values of $(n^-/n^+)_n$, in the case of PAMPSAA based PECs, can be ascribed to the presence of AMPS groups, which probably hindered the AA groups, conducting to a partially intrinsic compensate of carboxylic groups by the small counterions.

The AFM images indicated that the adsorbed particles prepared with a molar ratio between charges of $n^-/n^+ = 1.2$, appeared as compact particles, their size and shape being strongly influenced by the complementary polyelectrolytes structure.

A high colloidal stability was found for PAH based PECs, on the whole range of investigated molar ratios between charges, and after the $(n^-/n^+)_n$ for the CS based PECs.

Acknowledgements

The financial support of European Social Fund – 'Cristofor I. Simionescu' Postdoctoral Fellowship Program (ID POSDRU/89/1.5/S/55216) is gratefully acknowledged.

Abbreviations

AFM	atomic force microscopy
CS	chitosan
D_h	hydrodynamic diameter
DLS	dynamic light scattering
n^-/n^+	the molar ratio between anionic and cationic units
$(n^-/n^+)_n$	the molar ratio between anionic and cationic units when neutral complex particles were obtained
OD_{500}	optical density at λ = 500 nm
PAA	poly(acrylic acid)
PAH	poly(allylamine hidrochloride)
PAMPSAA	poly(2-acrylamido-2-methylpropanesulfonic acid – co- acrylic acid)
PI	polydispersity index
PEC	polyelectrolyte complexes
pzc	point of zero charge

References

[1] Drăgan S., Cristea M.: Polyelectrolyte complexes. Formation, characterization and applications. in 'Recent research developments in polymer science' (ed.: Pandalai S. G.) Transworld Research Network, Trivandrum, Kerala, Vol 7, 149–181 (2003).

[2] Tripathy S. K., Kumar J., Nalwa H. S.: Handbook of polyelectrolytes and their applications. Vol. 1–3, American Scientific Publishers, Los Angeles (2002).
[3] Thünemann A. F.: Polyelectrolyte–surfactant complexes (synthesis, structure and materials aspects). Progress in Polymer Science, **27**, 1473–1572 (2002). DOI: 10.1016/S0079-6700(02)00017-5
[4] Liu T., Burger C., Chu B.: Nanofabrication in polymer matrices. Progress in Polymer Science, **28**, 5–26 (2003). DOI: 10.1016/S0079-6700(02)00077-1
[5] Shi X., Shen M., Mohwald H.: Polyelectrolyte multilayer nanoreactors toward the synthesis of diverse nanostructured materials. Progress in Polymer Science, **29**, 987–1019 (2004). DOI: 10.1016/j.progpolymsci.2004.07.001
[6] Buchhammer H-M., Mende M., Oelmann M.: Preparation of monodisperse polyelectrolyte complex nanoparticles in dilute aqueous solution. Progress in Colloid and Polymer Science, **124**, 98–102 (2003). DOI: 10.1007/b12146
[7] Gärdlund L., Wågberg L., Gernandt R.: Polyelectrolyte complexes for surface modification of wood fibres: II. Influence of complexes on wet and dry strength of paper. Colloids and Surfaces A: Physicochemical and Engineering Aspects, **218**, 137–149 (2003). DOI: 10.1016/S0927-7757(02)00588-5
[8] Nyström R. G., Rosenholm J. B., Nurmi K.: Flocculation of semidilute calcite dispersions induced by anionic sodium polyacrylate−cationic starch complexes. Langmuir, **19**, 3981–3986 (2003). DOI: 10.1021/la034037j
[9] Müller M., Kessler B., Richter S.: Preparation of monomodal polyelectrolyte complex nanoparticles of PDADMAC/poly(maleic acid-alt-α-methylstyrene) by consecutive centrifugation. Langmuir, **21**, 7044–7051 (2005). DOI: 10.1021/la050716d
[10] Paneva D., Mespouille L., Manolova N., Degée P., Rashkov I., Dubois P.: Comprehensive study on the formation of polyelectrolyte complexes from (quaternized) poly[2-(dimethylamino)ethyl methacrylate] and poly(2-acrylamido-2-methylpropane sodium sulfonate). Journal of Polymer Science Part A: Polymer Chemistry, **44**, 5468–5479 (2006). DOI: 10.1002/pola.21594
[11] Gummel J., Boué F., Demé B., Cousin F.: Charge stoichiometry inside polyelectrolyte−protein complexes: A direct SANS measurement for the PSSNa−lysozyme system. The Journal of Physical Chemistry B, **110**, 24837–24846 (2006). DOI: 10.1021/jp064383k
[12] Hartig S. M., Carlesso G., Davidson J. M., Prokop A.: Development of improved nanoparticulate polyelectrolyte complex physicochemistry by nonstoichiometric mixing of polyions with similar molecular weights. Biomacromolecules, **8**, 265–272 (2007). DOI: 10.1021/bm0604754
[13] Petzold G., Nebel A., Buchhammer H-M., Lunkwitz K.: Preparation and characterization of different polyelectrolyte complexes and their application as flocculants. Colloid and Polymer Science, **276**, 125–130 (1998). DOI: 10.1007/s003960050219
[14] Reihs T., Müller M., Lunkwitz K.: Preparation and adsorption of refined polyelectrolyte complex nanoparticles. Journal of Colloid and Interface Science, **271**, 69–79 (2004). DOI: 10.1016/j.jcis.2003.11.019
[15] Sui Z., Jaber J. A., Schlenoff J. B.: Polyelectrolyte complexes with pH-tunable solubility. Macromolecules, **39**, 8145–8152 (2006). DOI: 10.1021/ma061098q
[16] Kötz J., Philipp B., Sigitov V., Kudaibergenov S., Bekturov E. A.: Amphoteric character of polyelectrolyte complex particles as revealed by isotachophoresis and viscometry. Colloid and Polymer Science, **266**, 906–912 (1988). DOI: 10.1007/BF01410845
[17] Kubota N., Kikuchi Y.: Macromolecular complexes of chitosan. in 'Polysaccharides: Structural diversity and functional versatility' (ed.: Dumitriu S.) Marcel Dekker, New York, 595–628 (1998).
[18] Franklin J. J., Snow A.: Biochemistry of antimicrobial action. Chapman Hall, London (1981).
[19] Lee K. Y., Ha W. S., Park W. H.: Blood compatibility and biodegradability of partially N-acylated chitosan derivatives. Biomaterials, **16**, 1211–1216 (1995). DOI: 10.1016/0142-9612(95)98126-Y
[20] Rabea E. I., Badawy M. E-T., Stevens C. V., Smagghe G., Steurbaut W.: Chitosan as antimicrobial agent: Applications and mode of action. Biomacromolecules, **4**, 1457–1465 (2003). DOI: 10.1021/bm034130m
[21] Yan X-L., Khor E., Lim L-Y.: Chitosan-alginate films prepared with chitosans of different molecular weights. Journal of Biomedical Materials Research Part B: Applied Biomaterials, **58**, 358–365 (2001). DOI: 10.1002/jbm.1029
[22] Wang L., Khor E., Wee A., Lim L-Y.: Chitosan-alginate PEC membrane as a wound dressing: Assessment of incisional wound healing. Journal of Biomedical Materials Research, **63**, 610–618 (2002). DOI: 10.1002/jbm.10382
[23] Rinaudo M.: Chitin and chitosan: Properties and applications. Progress in Polymer Science, **31**, 603–632 (2006). DOI: 10.1016/j.progpolymsci.2006.06.001

[24] Shi X., Du Y., Sun L., Zhang B., Dou A.: Polyelectrolyte complex beads composed of water-soluble chitosan/alginate: Characterization and their protein release behavior. Journal of Applied Polymer Science, **100**, 4614–4622 (2006).
DOI: 10.1002/app.23021

[25] Bratskaya S., Marinin D., Simon F., Synytska A., Zschoche S., Busscher H. J., Jager D., van der Mei H. C.: Adhesion and viability of two enterococcal strains on covalently grafted chitosan and chitosan/κ-carrageenan multilayers. Biomacromolecules, **8**, 2960–2968 (2007).
DOI: 10.1021/bm700620j

[26] Kang H-S., Park S-H., Lee Y-G., Son T-I.: Polyelectrolyte complex hydrogel composed of chitosan and poly(γ-glutamic acid) for biological application: Preparation, physical properties, and cytocompatibility. Journal of Applied Polymer Science, **103**, 386–394 (2007).
DOI: 10.1002/app.24623

[27] Crini G., Badot P-M.: Application of chitosan, a natural aminopolysaccharide, for dye removal from aqueous solutions by adsorption processes using batch studies: A review of recent literature. Progress in Polymer Science, **33**, 399–447 (2008).
DOI: 10.1016/j.progpolymsci.2007.11.001

[28] Paneva D., Ignatova M., Manolova N., Rashkov I.: Novel chitosan-containing micro- and nanofibrous materials by electrospinning: Preparation and biomedical application. in 'Nanofibers: Fabrication, performance and applications' (ed.: Chang W. N.) Nova Science Publishers, New York, 73–151 (2009).

[29] Mihai M., Dragan E. S.: Chitosan based nonstoichiometric polyelectrolyte complexes as specialized flocculants. Colloids and Surfaces A: Physicochemical and Engineering Aspects, **346**, 39–46 (2009).
DOI: 10.1016/j.colsurfa.2009.05.021

[30] Dragan E. S., Schwarz S.: Polyelectrolyte complexes. VII. Complex nanoparticles based on poly(sodium 2-acrylamido-2-methylpropanesulfonate) tailored by the titrant addition rate. Journal of Polymer Science Part A: Polymer Chemistry, **42**, 5244–5252 (2004).
DOI: 10.1002/pola.20388

[31] Dragan E. S., Mihai M., Schwarz S.: Polyelectrolyte complex dispersions with a high colloidal stability controlled by the polyion structure and titrant addition rate. Colloids and Surfaces A: Physicochemical and Engineering Aspects, **290**, 213–221 (2006).
DOI: 10.1016/j.colsurfa.2006.05.022

[32] Mihai M., Dragan E. S., Schwarz S., Janke A.: Dependency of particle sizes and colloidal stability of polyelectrolyte complex dispersions on polyanion structure and preparation mode investigated by dynamic light scattering and atomic force microscopy. The Journal of Physical Chemistry B, **111**, 8668–8675 (2007).
DOI: 10.1021/jp071655q

[33] Dragan E. S., Mihai M., Schwarz S.: Complex nanoparticles based on chitosan and ionic/nonionic strong polyanions: Formation, stability, and application. ACS Applied Materials and Interfaces, **1**, 1231–1240 (2009).
DOI: 10.1021/am900109u

[34] Gamzazade A. I., Šlimak V. M., Skljar A. M., Štykova E. V., Pavlova S. A., Rogožin S. V.: Investigation of the hydrodynamic properties of chitosan solutions. Acta Polymerica, **36**, 420–424 (1985).
DOI: 10.1002/actp.1985.010360805

[35] Jiang X., Chen L., Zhong W.: A new linear potentiometric titration method for the determination of deacetylation degree of chitosan. Carbohydrate Polymers, **54**, 457–463 (2003).
DOI: 10.1016/j.carbpol.2003.05.004

[36] Hirai A., Odani H., Nakajima A.: Determination of degree of deacetylation of chitosan by ^{1}H NMR spectroscopy. Polymer Bulletin, **26**, 87-94 (1991).
DOI: 10.1007/BF00299352

[37] Dragan S., Cristea M., Luca C., Simionescu B. C.: Polyelectrolyte complexes. I. Synthesis and characterization of some insoluble polyanion-polycation complexes. Journal of Polymer Science Part A: Polymer Chemistry, **34**, 3485–3494 (1996).
DOI: 10.1002/(SICI)1099-0518(199612)34:17<3485::AID-POLA3>3.0.CO;2-U

[38] Stoilova O., Koseva N., Manolova N., Rashkov I.: Polyelectrolyte complex between chitosan and poly(2-acryloylamido-2-methylpropanesulfonic acid). Polymer Bulletin, **43**, 67–73 (1999).
DOI: 10.1007/s002890050534

[39] Dubas S. T., Schlenoff J. B.: Polyelectrolyte multilayers containing a weak polyacid: Construction and deconstruction. Macromolecules, **34**, 3736–3740 (2001).
DOI: 10.1021/ma001720t

[40] Dinu I. A., Mihai M., Dragan E. S.: Comparative study on the formation and flocculation properties of polyelectrolyte complex dispersions based on synthetic and natural polycations. Chemical Engineering Journal, **160**, 115–121 (2010).
DOI: 10.1016/j.cej.2010.03.018

eXPRESS Polymer Letters Vol.5, No.6 (2011) 516–525
Available online at www.expresspolymlett.com
DOI: 10.3144/expresspolymlett.2011.50

Mechanical performance of ozone functionalized MWCNTs/PC nanocomposites

Z. Zhang[1*], *K. Peng*[1], *Y. Chen*[2]

[1]National Center for Nanoscience and Technology, China, Beijing 100190, China
[2]Institute of Process Engineering, Chinese Academy of Sciences, Beijing 100190, China

Received 16 October 2010; accepted in revised form 16 December 2010

Abstract. Multi-walled carbon nanotubes (MWCNTs) were functionalized by ozone (O_3) and then melting mixed into polycarbonate (PC) matrix. The effect of O_3 functionalization on the mechanical performance was systematically studied. It was found that the modified MWCNTs exhibited improved dispersion and interfacial adhesion to the matrix as evidenced by scanning electron microscope and micro-Raman spectrometer, which were believed to contribute to the enhanced yield strength of MWCNTs/PC nanocomposites.

Keywords: *polymer nanocomposites, multi-walled carbon nanotubes, ozone functionalization, polycarbonate, mechanical property*

1. Introduction

Carbon nanotubes (CNTs) have been expected to be an ideal reinforcement for polymers due to their unique one-dimensional structure with good electrical conductivity, robust mechanical and thermal properties [1–3]. Because of their large aspect ratio and high van der Waals interactions, CNTs are normally difficult to be dispersed into polymeric matrices. Meanwhile, their chemical inertness makes them difficult to achieve good interaction with polymers. Chemical functionalizations were shown to be feasible and effective for improving the solubility and dispersion of CNTs. Moreover the functionalized CNTs can provide bonding sites to the polymer matrix so that the adhesion between the polymer and CNTs can be enhanced. So far, the wet chemical modification is the most conventional method to introduce oxygen-containing moieties onto the CNT surface [4, 5]. However, the liquid wastes generated from these solution-phase oxidation methodologies together with the tedious purification procedures would greatly limit their further development of applications. Ozone (O_3) as an environmental friendly route to functionalize CNTs has aroused strong interests for both academia and industry recently [6–9]. One of the most prominent advantages is that this method works under dry conditions without dispersing CNTs into solvents and therefore is convenient for further scale-up. Furthermore, according to our previous study [10], this method can be even carried out at atmospheric pressure and room temperature, leading to comparatively cheaper equipments and lower running costs. Although the oxidation of CNTs by O_3 has been extensively studied [6–9], little research has been done so far on the effect of functionalized CNTs to the mechanical performance of polymer matrices, especially for thermoplastics. Some researchers reported the usage of O_3 oxidized CNTs by either subsequent grafting of a coupling agent or direct dispersing into epoxy resins [11, 12]. In this study, we incorporate O_3 functionalized multi-walled car-

*Corresponding author, e-mail: zhong.zhang@nanoctr.cn

bon nanotubes (MWCNTs) into a polycarbonate (PC) matrix by melt mixing. The amorphous PC was chosen since it is known that CNTs may modify the crystalline morphology in semi-crystalline polymers, which may complicate the interpretation of the effect of O_3 functionalized MWCNTs.

2. Experimental

2.1. Materials

The pristine MWCNTs (marked as *p*-MWCNTs in this paper) were prepared by a chemical vapor deposition method with purity >95 wt.%, average diameter between 10 and 20 nm, and length between 1 and 10 μm. The PC has a brand name as Macrolon 2800, with the melt flow index = 9 g/10 min at 300°C, and density ρ = 1.2 g/cm^3. Both MWCNTs and PC were supplied by Bayer MaterialScience AG (Leverkusen, Germany). Before further functionalization or melt-mixing process, the MWCNTs, PC or master-batches were dried at 373 K overnight within a vacuum oven.

2.2. Functionalization of MWCNTs

The MWCNTs were functionalized with O_3 at room temperature, which has been discussed in our recent work [10]. Generally, 3 g of *p*-MWCNTs was placed into a homemade vertical reactor each time. The O_3 (5 wt% in O_3/O_2 mixture) was continuously passed through the reactor chamber at room temperature during the oxidation process. The reaction time was fixed for 2 or 4 hours, and then the functionalized MWCNTs were defined as 2h-MWCNTs and 4h-MWCNTs in this paper.

2.3. Preparation of nanocomposite

A master batch of 15 wt% MWCNTs in PC was produced by the melt-mixing process in a twin screw extruder (HAAKE-Polylab OS, Haake being part of Thermo Scientific). The screw speed was set at 150 rpm. All barrels of the extruder were set to a heating temperature of 280°C except the barrels of the melting zone which was 270°C. After extrusion, the PC/MWCNT composites were cooled down in a water bath and then finally granulated with a pelletizer. The master batch was diluted by pure PC to obtain concentrations of 1, 3 and 5 wt% MWCNTs in the matrix. Dog-bone samples were prepared using a HAAKE mini-injection molding machine. The barrel temperature was 300°C and the mold temperature was 120°C, and the injection pressure was 800 bar.

2.4. Characterization

Tensile tests were carried out according to a standard methodology of ASTM D638. They were performed using a SANS CMT2000 Tester equipped with an extensometer at a crosshead speed of 1 mm/min at ambient temperature. Young's modulus, yield stress, and elongation at break of each sample were obtained based on at least five specimens per sample.

The composite films were prepared by hot press at 290°C, and the pressure was 5 MPa. The final dimension of the film was 5×5×0.1 mm^3 (length×width×thickness). The Raman spectra were obtained using a Renishaw 2000 MicroRaman spectrometer (Reinshaw, Wotton-under-Edge, UK) with an excitation length of 633 nm. The compressive stresses were produced in the MWCNTs by quenching the composite specimen down to specific temperature using the cooling cell. Quenching was performed by injecting nitrogen gas from a liquid nitrogen reservoir through the thermally isolated cooling cell. The temperatures used in our experiment ranged from 353 K down to 193 K, with a cooling rate of 10°C/min. Thermal equilibrium in each case was obtained by holding the specimen for 10 min at a constant temperature.

The fracture surface of the composite samples was analyzed using a Hitachi S4800 scanning electron microscope (SEM). The morphology of O_3 functionalized MWCNTs was observed using transmission electron microscope (TEM, FEI Tecnai G^2 F20, FEI, Hillsboro, Oregon, USA).

Fourier transform infrared (FTIR) spectra were recorded on Perkin Elmer Spectrum One spectrometer. The MWCNTs were pressed into pellet with potassium bromide and scanned from 4000 to 800 cm^{-1} with a resolution of 2 cm^{-1}. Thermogravimetric analysis (TGA) was performed in a Perkin Elmer Diamond thermogravimetric analyzer under nitrogen atmosphere from 30 to 700°C at a speed of 20°C/min.

The volume resistivity (ρ_v) was measured on strips (12×10×20 mm^3) prepared by compression molding. Four-point fixture combined with a Keithley 4200-SCS electrometer (Keithley, Cleveland, Ohio, USA) was used to measure volume resistance (R_v)

of PC/MWCNT composite samples. The R_v was converted to ρv, using Equation (1):

$$\rho_v = R_v \cdot \frac{A}{t} \quad (1)$$

where A is the effective area of the measuring electrode and t is the specimen thickness.

3. Results and discussion

3.1. Surface functionalization of MWCNTs

Figure 1 gives the typical FTIR spectra of MWCNTs before and after O_3 treatment. For the *p*-MWCNTs, the peak at 1580 cm^{-1} is assigned to the stretching mode of *v*(C=C) of the double bonds in the MWCNT backbone near the surface active sites. After O_3 treatment, the intensity of peak around 1720 cm^{-1} related to carboxylic groups shows an increasing trend, which suggested the MWCNTs were functionalized by treating with O_3. The broad band appeared at 1170 cm^{-1} is attributed to the vibration mode of *v*(O–C–O) of ester or *v*(C–O) of carboxylic acid [13].

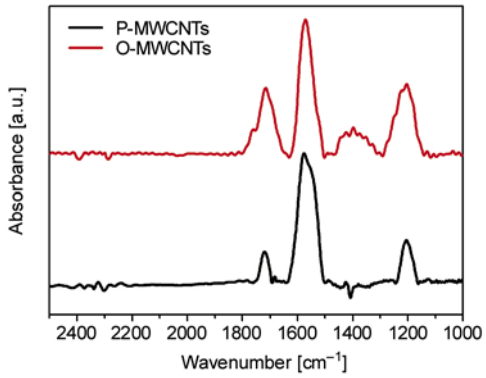

Figure 1. FTIR spectra of the MWCNTs before and after O_3 treatment

3.2. Mechanical property

Figure 2a shows typical stress-strain curves for the PC and PC/MWCNT composites at 3 wt% MWCNT concentration. The values of the elastic modulus as a function of the MWCNT concentration are presented graphically in Figure 2b. Young's modulus of the PC composites visibly increases with increase of MWCNT content regardless of the functionalization. As the MWCNT loadings increase, yield stress of the composite filled with 2h-MWCNTs increased over the range we studied (Figure 2c), whereas yield stress of the composite filled with *p*-MWCNTs decreases at 5 wt% MWCNT concentration.

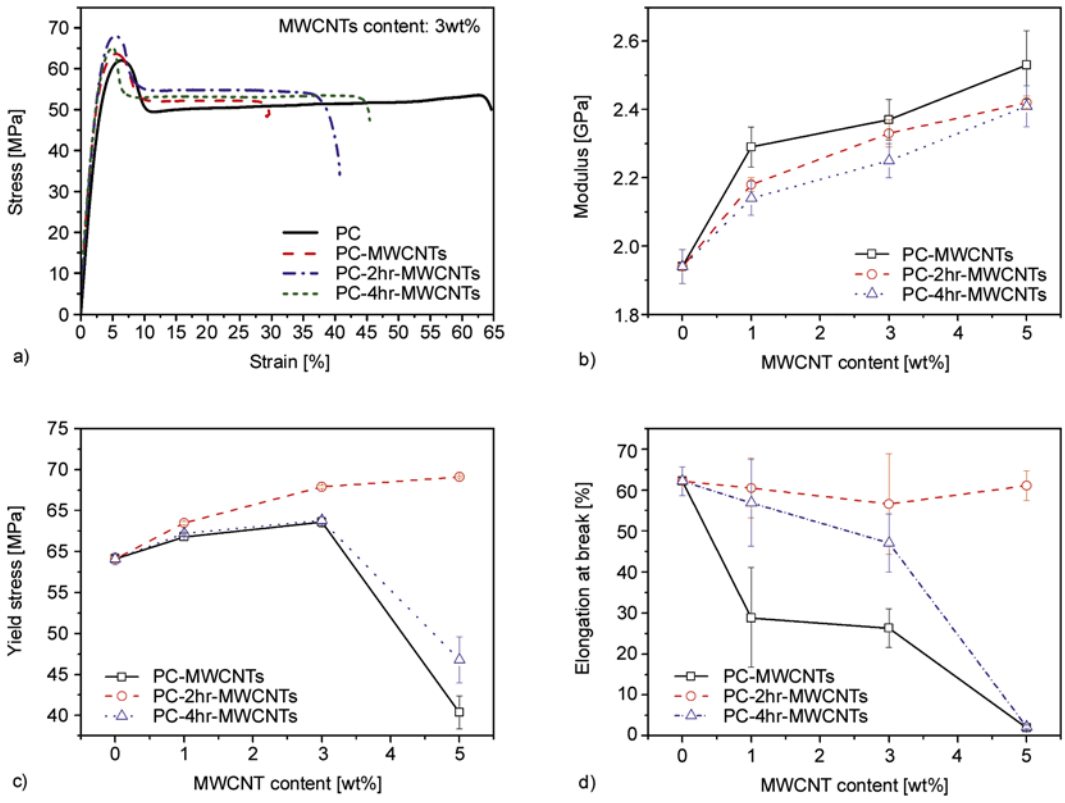

Figure 2. Mechanical properties of MWCNT-filled polycarbonate: (a) stress-strain curves of pure PC and PC/MWCNT composites; (b)~(d) elastic modulus, yield stress and elongation at break as a function of MWCNT content for PC-MWCNTs, PC-2h-MWCNTs and PC-4h-MWCNT samples

Figure 2d shows that elongation at break of PC composites reduces significantly from 60% for neat PC to 2% when *p*-MWCNT content is 5 wt%. However, elongation at break of PC-2h-MWCNT composite had no obvious variation. Notably, for the PC-4h-MWCNT composite, the Young's modulus, yield stress and elongation at break show the similar trend, compared with the *p*-MWCNT based composite, which will be discussed further on.

3.3. Morphology characterization

The quality of the MWCNT dispersion in the composite is examined by SEM. Usually, good dispersion is necessary for optimal mechanical properties [14, 15]. Figure 3 shows the SEM images of the fracture surface of composites at 5 wt% MWCNT concentration, providing some insights of the MWCNT dispersion state. The *p*-MWCNTs are presented mainly in the form of agglomerates, whereas the 2h-MWCNTs are dispersed more uniformly, confirming that O_3 treatment can facilitate MWCNT dispersion in PC matrix, as compared in Figure 3a and b. The agglomerates in poorly dispersed composites cause cracks to initiate and propagate easily, and the generated cracks reduce the strength of the composite. On the contrary, well dispersed MWCNTs are more efficient than the aggregated MWCNTs in transferring applied load. Therefore, a significant enhancement in mechanical property of PC-2h-MWCNT composite compared with that of PC-MWCNTs composite is observed.

3.4. Temperature dependent Raman spectroscopy

Except for the good dispersion, strong interface is also important for CNTs reinforced composite because the external stresses applied to the composite as a whole can be efficiently transferred to the CNTs, allowing them to take a disproportionate share of the load. Due to its sensitivity to the interatomic distance, Raman spectroscopy has been widely used to evaluate the interaction between polymers and CNTs in CNT based composites [16]. Generally, the interaction between CNTs and matrix can be reflected by the Raman shifts of the characteristic peaks [17, 18]. Figure 4a shows the most prominent Raman spectra modes of MWCNTs are the *G*-band (1580 cm^{-1}), the *D*-band (1340 cm^{-1}) and the *G′*-band (2650 cm^{-1}), exited with 633 nm laser [19]. According to Wagner's studies [17], the *G′*-band was found to be exact and convenient to monitor the temperature-induced strain of CNTs embedded in the polymer. In the present study, we induced a compressive deformation in MWCNTs embedded in the PC matrix by cooling the specimens from 353 to 193 K. As shown in Figure 4b, the *G′*-band Raman spectra for 2h-MWCNTs peaked at 2645 cm^{-1}, whereas the *G′*-band for 2h-MWCNTs embedded in PC matrix peaks at 2655 cm^{-1} at 353 K. The higher frequencies shifts were caused by the compression of C=C bonds, which resulted from mismatch in the coefficient of thermal expansion between MWCNTs and PC matrix [17]. With

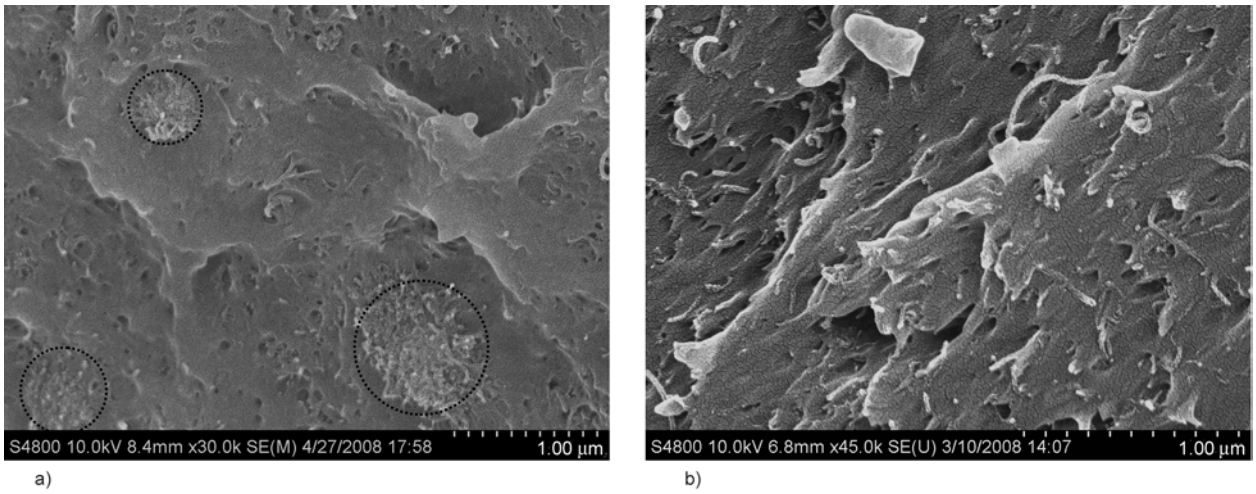

Figure 3. SEM images of composite fracture surfaces showing the dispersion states of MWCNTs. (a) 5 wt% *p*-MWCNTs; (b) 5 wt% 2hr-MWCNTs

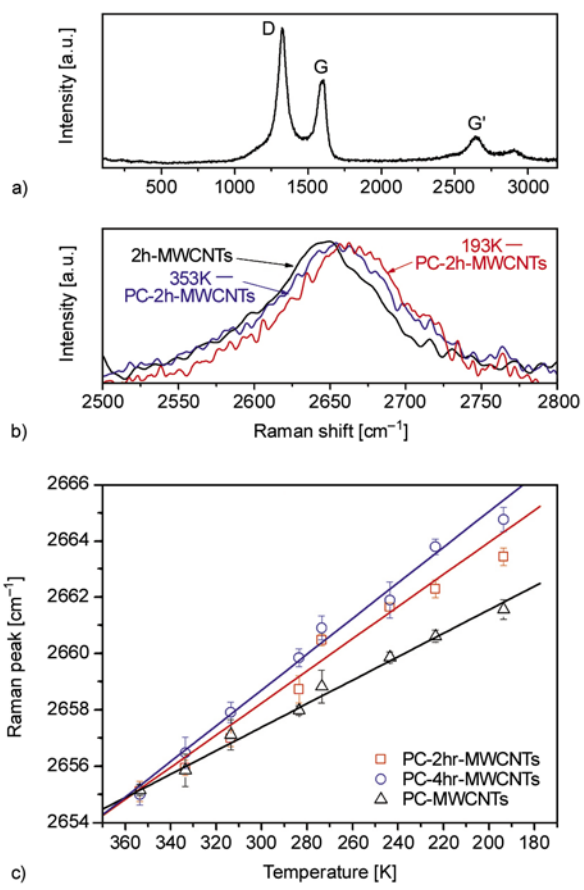

Figure 4. (a) Raman spectra of MWCNTs excited with 633 nm laser; (b) and (c) effects of embedment and cooling on the frequency shift of the *G*′-band of MWCNTs

decreased temperature, the obvious upward shifts of Raman *G*′-band peak position for the embedded MWCNTs are expected, and arise from the further shortening of C=C bond length due to the compressive stresses from the matrix. As seen in Figure 4c, the cooling of the embedded materials from 353 K down to 193 K causes 5 and 8 cm^{-1} shift for *p*-MWCNTs and 2h-MWCNTs, respectively. Comparing with *p*-MWCNT based composite, the 2h-MWCNTs embedded in PC matrix shows larger *G*′-band shift over the temperature range we studied, illuminating more efficient load transfer between the 2h-MWCNTs and PC matrix. The results also indicate that *G*′-band appears larger up-shift with increase of O_3 treatment time. By extending O_3 treatment time, more functional groups can be attached onto the MWCNT surface [10]. Therefore, with the higher degree functionalization on the nanotube surface, PC-4h-MWCNT composite shows much better load transfer behavior.

Furthermore, the morphology of the fracture surface of MWCNTs based nanocomposites can also reflect the interface status. We can find that many holes exist on the fracture surface of PC-*p*-MWCNT composite indicated by the arrow in Figure 5a, which means MWCNTs are pulled out of the matrix due to the poor interfacial bonding between *p*-MWCNTs and PC. However, there is no obvious hole on the fracture surface of PC-2h-MWCNT composite (Figure 5b), suggesting improved interfacial adhesion between 2h-MWCNTs and matrix.

3.5. Thermal stability

The effect of MWCNT presence on the thermal stability of PC composites is studied by means of TGA in N_2 atmosphere, as shown in Figure 6. The temperature corresponding to an initial 5% of weight loss ($T_{5\%}$), to 50% of weight loss ($T_{50\%}$), and the temperature of the maximum rate of weight loss (T_{max}) obtained by TGA and by TGA derivative weight curves are given in Table 1. For pure PC, the

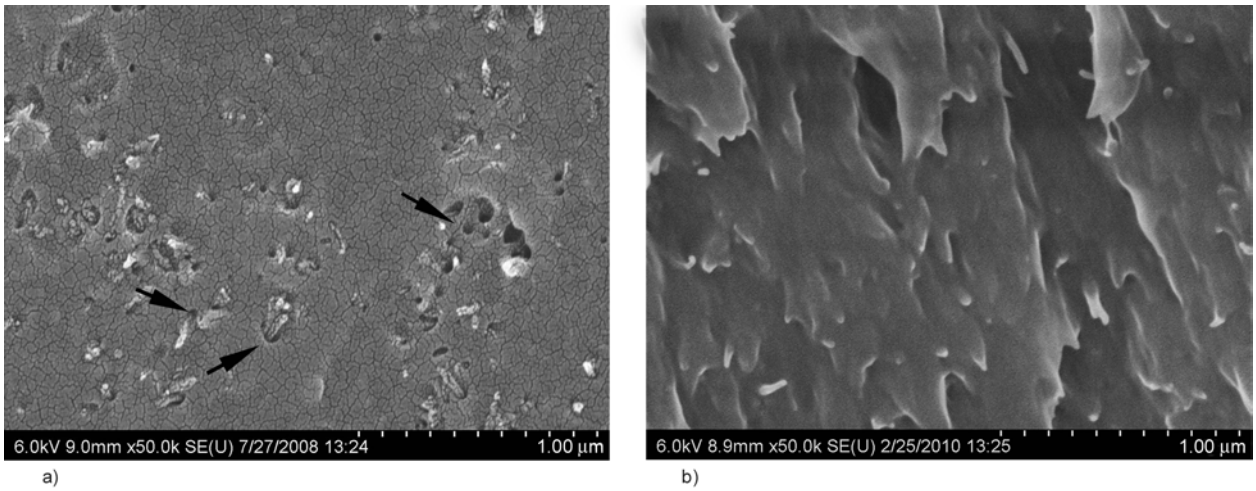

Figure 5. SEM images of composite fracture surfaces: (a) PC-3wt%-MWCNTs; (b) PC-3wt%-2hr-MWCNTs

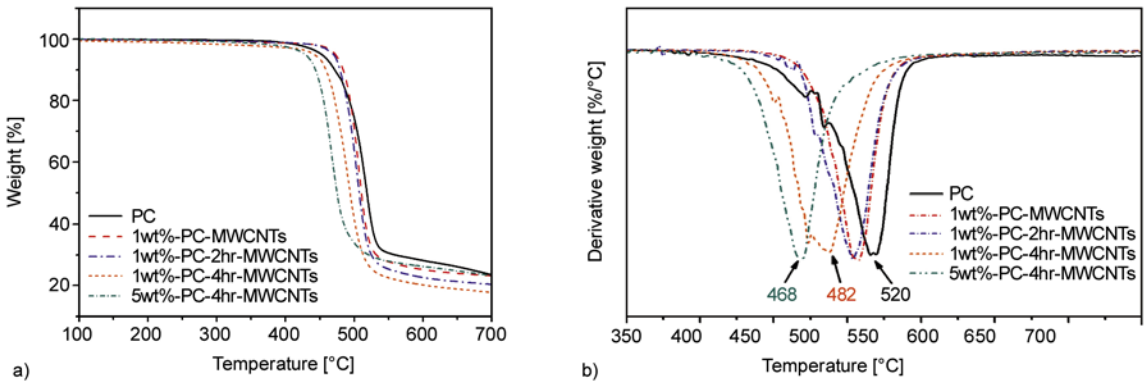

Figure 6. TGA curves of the PC and its composites in N_2 atmosphere: (a) weight loss curves; (b) derivate weight curves

Table 1. TGA data of the PC and its composites

Sample	$T_{5\%}$ [°C]	$T_{50\%}$ [°C]	T_{max} [°C]
PC	452	518	520
PC-1wt%-MWCNTs	472	510	507
PC-1wt%-2h-MWCNTs	470	507	504
PC-1wt%-4h-MWCNTs	441	494	482
PC-5wt%-4h-MWCNTs	428	474	468

major degradation occurs between 460 and 530°C, and that is followed by a much slower degradation process; T_{max} is 520°C. The TGA results indicate that adding MWCNTs and 2h-MWCNTs into the PC matrix can increase the initial decomposition temperature $T_{5\%}$. However, the $T_{5\%}$ of PC-1wt%-4h-MWCNT composite appears to be lower than that of pure PC, implying worse thermal stability for PC-1wt%-4h-MWCNT composite. The major degradation step for the PC-MWCNTs, PC-2h-MWCNTs and PC-4h-MWCNT composites occur at a much lower temperature. T_{max} for PC-1wt%-MWCNTs, PC-1wt%-2h-MWCNTs and PC-1wt%-4h-MWCNTs are 507, 504 and 482°C, lower than that of pure PC. Additionally, T_{max} for PC-5wt%-4h-MWCNTs is just 482°C, which evidently decreases as the MWCNT content increase. Due to the depressed

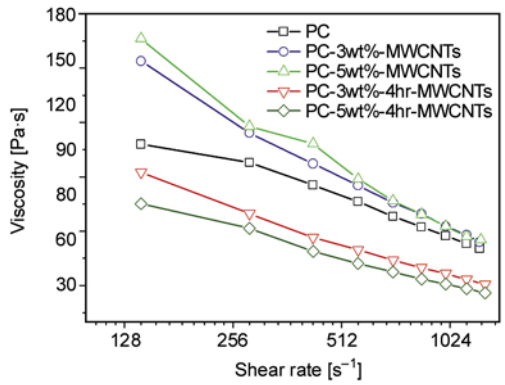

Figure 7. Melt viscosity behavior of composite at 270°C

thermal stability of nanocomposites from TGA results, we can conclude that the molecular weight of the PC matrix degrades in the presence of MWCNTs, as demonstrated by Pötschke [20].

In order to further explore the effects of different blending processes on the degradation of PC, the melt viscosity behavior during mixing in a Haake Minilab ctw5 is monitored in terms of melt viscosity. The viscosity changes during mixing PC with MWCNT and mixing PC with 4h-MWCNTs are compared with that of pure PC, respectively. As shown in Figure 7, the melt viscosity of PC-MWCNT composite is obviously higher than that of pure PC at the same shear rate. However, the incorporation of 4h-MWCNTs leads to the decrease of the melt viscosity due to the degradation of PC matrix during the melt mixing. Usually, alcohols and carboxylic acids can lead to molecular degradation through ester interchange. According to Legras's studies [21, 22], arylcarboxylate salts can attack the carboxylate groups on the carbonate group through nucleophilic and severely degrade the PC. Therefore, the degradation of PC in our study is due to the carboxylic and carbonyl groups on the MWCNT surface. According to Pötschke's study [20], there are two counteracting effects on mechanical property of composites during the composites prepared by dilution of master-batch: on the one hand, the MWCNT addition can enhance the mechanical property of composite; on the other hand, the degradation of PC would reduce the mechanical performance. Therefore, the mechanical property of PC-2h-MWCNT composite was improved, while as that of PC-4h-MWCNT composite is degraded, as already given in Figure 2.

3.6. Electrical conductivity

The concentration dependencies of ρ_v of PC composites with pristine and surface modified MWCNTs for three types are plotted in Figure 8. It can be seen that all MWCNT based PC composites exhibit a typical percolation behavior. The introduction of MWCNTs to PC decreases the ρ_v of the resulting composites. As shown in Figure 8, the percolation threshold value for PC-MWCNTs and PC-2h-MWCNT composites is 1.0 wt% and reaches up to 5 wt% for PC-4h-MWCNT composite.

According to ρv measurement results, the surface modification exhibits a practical effect on them. At the same MWCNT content, the ρv of the composite increases with extending O_3 treatment time to MWCNTs, as shown in Figure 8. To our knowledge, there are three main requirements for ρ_v of CNTs based composites. These are intrinsic CNT resistance, good dispersion and aspect ratio. Usually, the CNTs show increase in their R_v due to the damage to their intrinsic structures after oxidative treatment [23, 24]. According to Simmons and coworker's study [24], since the π-conjugated path on the sidewalls of the SWCNTs can be disrupted by O_3 treatment, the resistance of SWCNTs increased after oxidation. Therefore, the electrical conductivity of MWCNTs could be lowered after O_3 treatment in our case.

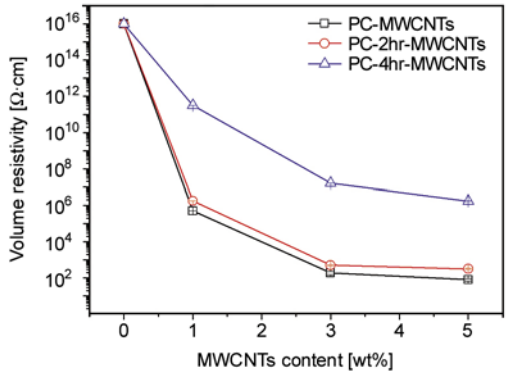

Figure 8. Volume resistivity versus MWCNT content in PC

To exclude the aspect ratio effect of MWCNTs on ρ_v of composites, the two type MWCNTs are extracted after PC-MWCNTs and PC-4h-MWCNT composites are dissolved in tetrahydrofuran. Both had almost the same aspect ratio, as shown in Figure 9.

The morphologies of *p*-MWCNTs, 2h-MWCNTs and 4h-MWCNTs on the carbon grids were observed by TEM, which were extracted from composite. Figure 10 display TEM images of MWCNTs extracted from the PC matrix. From Figure 9a, it can be seen that *p*-MWCNTs keep the same as that of their original. However, from Figure 9b and c, it is clear that the O_3 modified MWCNT surface is covered by a polymer layer, which should be the PC component. This observation further proves that ester interchange reaction is expected to occur between MWCNTs and PC matrix due to the existence of carboxyl groups on the MWCNT surface. Moreover, according to the statistical analysis, the average thickness of coverage polymer for 2h-MWCNTs and 4h-MWCNTs are 3.54±0.35 nm and 7.38±1.78 nm, respectively. Apparently, the thickness of polymer layer increases with the increased O_3 treatment time of MWCNTs. The polymer layer around MWCNT surface would increase the contact resistance between the MWCNTs, which would impair the conductivity of the composite further. The ρ_v results suggest that the PC-coating could

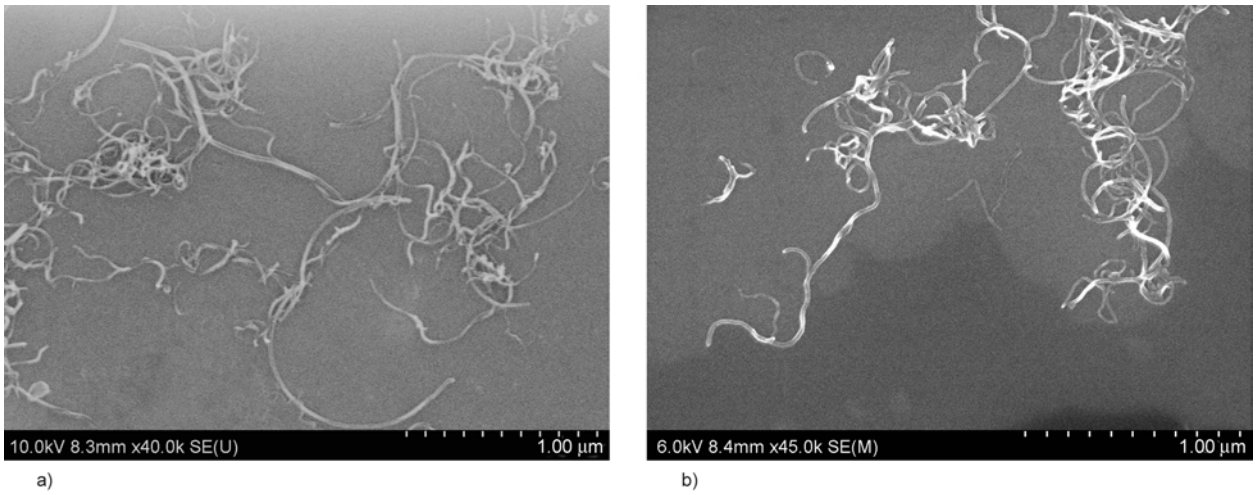

a) b)

Figure 9. SEM images of MWCNTs extracted from PC/MWCNT composite: (a) PC-MWCNTs; (b) PC-4h-MWCNTs

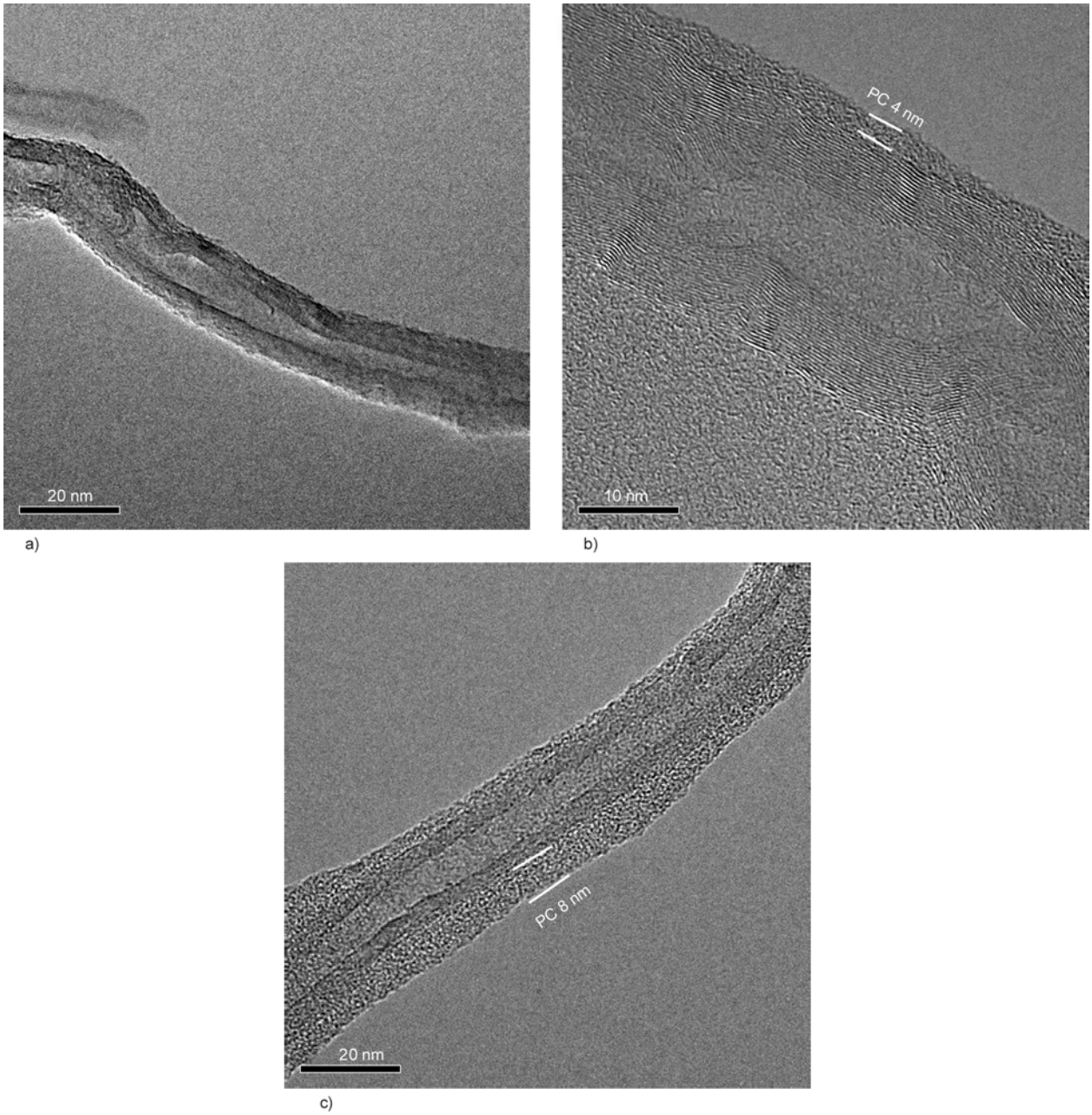

Figure 10. TEM images of MWCNTs extracted from PC/MWCNT composite: (a) PC-MWCNTs; (b) PC-2h-MWCNTs; (c) PC-4h-MWCNTs

effectively insulate the MWCNT surface due to their highly non-conducting property. Additionally, the lower ρ_v value in the case of PC-2h-MWCNTs than that of the PC-4h-MWCNT sample is due to the presence of less amount of PC polymer on the surface of 2h-MWCNTs.

4. Conclusions

Series of as-received and O_3 treated MWCNTs based PC composites are prepared by diluting a master-batch containing 15 wt% MWCNTs using melt mixing. The findings highlighted in this paper may contribute to our understanding on the efficiency of ozonolysis of PC/MWCNT nanocomposites. Therefore, following conclusions can be drawn:

1) Relatively good dispersion is achieved for the O_3 treated MWCNTs. A number of 2h-MWCNTs are found to break rather than pull out at the fracture surface, suggesting that strong bonding exists between PC matrix and MWCNTs. The strong interaction between the 2h-MWCNTs and PC matrix would facilitate the load transfer, resulting improved tensile property in their PC matrix.

2) The thermal stability of PC shows an unusual behavior after adding MWCNTs. According to TGA results, the thermal stability of MWCNT based PC composite reveals a significant decrease after incorporation of O_3 treated MWCNTs due to the degradation of PC matrix, especially for 4h-MWCNTs. This effect leads to the decreased mechanical properties.
3) Notably, the results also indicate that the surface modification of MWCNTs as obtained by O_3 treatment can influence in the electrical property. The percolation threshold value for PC-MWCNTs and PC-2h-MWCNT composites is 1.0 wt% and reaches up to 5 wt% for PC-4h-MWCNT composite. The O_3 treatment does affect the ρ_v negatively due to the change in the MWCNT lattice structure and the formation of a strongly adhered isolating PC layer around the surface of modified MWCNTs.

Acknowledgements

This project was jointly supported by the National Key Basic Research Program of China (Grant No. 2007CB936803) and a key international collaboration project (Grant No. 2008DFA51220) of the Ministry of Science and Technology of China, a key item of the Knowledge Innovation Project of the Chinese Academy of Science (Grant No. KJCX2-YW-M01) and the National Natural Science Foundation of China (Grant No. 51073044). The authors appreciate Bayer MaterialScience AG for supplying the raw materials.

References

[1] Wong E. W., Sheehan P. E., Lieber C. M.: Nanobeam mechanics: Elasticity, strength, and toughness of nanorods and nanotubes. Science, **277**, 1971–1975 (1997). DOI: 10.1126/science.277.5334.1971
[2] Tans S. J., Verschueren A. R. M., Dekker C.: Room-temperature transistor based on a single carbon nanotube. Nature, **393**, 49–52 (1998). DOI: 10.1038/29954
[3] Berber S., Kwon Y. K., Tománek D.: Unusually high thermal conductivity of carbon nanotubes. Physical Review Letters, **84**, 4613–4616 (2000). DOI: 10.1103/PhysRevLett.84.4613
[4] Liu J., Rinzler A. G., Dai H., Hafner J. H., Bradley R. K., Boul P. J., Iverson T., Shelimov K., Huffman C. B., Rodriguez-Macias F., Shon Y-S., Lee T. R., Colbert D. T., Smalley R. E.: Fullerene pipes. Science, **280**, 1253–1256 (1998). DOI: 10.1126/science.280.5367.1253
[5] Zhang J., Zou H. L., Qing Q., Yang Y. L., Li Q. W., Liu Z. F., Guo X., Du Z.: Effect of chemical oxidation on the structure of single-walled carbon nanotubes. Journal of Physical Chemistry B, **107**, 3712–3718 (2003). DOI: 10.1021/jp027500u
[6] Banerjee S., Wong S. S.: Rational sidewall functionalization and purification of single-walled carbon nanotubes by solution-phase ozonolysis. Journal of Physical Chemistry B, **106**, 12144–12151 (2002). DOI: 10.1021/jp026304k
[7] Cai L. T., Bahr J. L., Yao Y. X., Tour J. M.: Ozonation of single-walled carbon nanotubes and their assemblies on rigid self-assembled monolayers. Chemistry of Materials, **14**, 4235–4241 (2002). DOI: 10.1021/cm020273o
[8] Liu L. V., Tian W. Q., Wang Y. A.: Ozonization at the vacancy defect site of the single-walled carbon nanotube. Journal of Physical Chemistry B, **110**, 13037–13044 (2006). DOI: 10.1021/jp055999x
[9] Byl O., Liu J., Yates J. T.: Etching of carbon nanotubes by ozone – A surface area study. Langmuir, **21**, 4200–4204 (2005). DOI: 10.1021/la040132w
[10] Peng K., Liu L. Q., Li H. C., Meyer H., Zhang Z.: Room temperature functionalization of carbon nanotubes using an ozone/water vapor mixture. Carbon, **49**, 70–76 (2010). DOI: 10.1016/j.carbon.2010.08.043
[11] Choi Y-K., Gotoh Y., Sugimoto K-I., Song S-M., Yanagisawa T., Endo M.: Processing and characterization of epoxy nanocomposites reinforced by cup-stacked carbon nanotubes. Polymer, **46**, 11489–11498 (2005). DOI: 10.1016/j.polymer.2005.10.028
[12] Ma P. C., Kim J-K., Tang B. Z.: Effects of silane functionalization on the properties of carbon nanotube/epoxy nanocomposites. Composites Science and Technology, **67**, 2965–2972 (2007). DOI: 10.1016/j.compscitech.2007.05.006
[13] Mawhinney D. B., Naumenko V., Kuznetsova A., Yates J. T., Liu J., Smalley R. E.: Infrared spectral evidence for the etching of carbon nanotubes: Ozone oxidation at 298 K. Journal of the American Chemical Society, **122**, 2383–2384 (2000). DOI: 10.1021/ja994094s
[14] Song Y. S., Youn J. R.: Influence of dispersion states of carbon nanotubes on physical properties of epoxy nanocomposites. Carbon, **43**, 1378–1385 (2005). DOI: 10.1016/j.carbon.2005.01.007
[15] Thostenson E. T., Chou T-W.: Processing-structure-multi-functional property relationship in carbon nanotube/epoxy composites. Carbon, **44**, 3022–3029 (2006). DOI: 10.1016/j.carbon.2006.05.014

[16] Gao Y., Li L. Y., Tan P-H., Liu L. Q., Zhang Z.: Application of Raman spectroscopy in carbon nanotube-based polymer composites. Chinese Science Bulletin, **55**, 3978–3988 (2010).
DOI: 10.1007/s11434-010-4100-9

[17] Lourie O., Wagner H. D.: Evaluation of Young's modulus of carbon nanotubes by micro-Raman spectroscopy. Journal of Materials Research, **13**, 2418–2422 (1998).
DOI: 10.1557/JMR.1998.0336

[18] Schadler L. S., Giannaris S. C., Ajayan P. M.: Load transfer in carbon nanotube epoxy composites. Applied Physics Letters, **73**, 3842–3844 (1998).
DOI: 10.1063/1.122911

[19] Rao A. M., Jorio A., Pimenta M. A., Dantas M. S. S., Saito R., Dresselhaus G., Dresselhaus M. S.: Polarized raman study of aligned multiwalled carbon nanotubes. Physical Review Letters, **84**, 1820–1823 (2000).
DOI: 10.1103/PhysRevLett.84.1820

[20] Pötschke P., Bhattacharyya A. R., Janke A., Goering H.: Melt mixing of polycarbonate/multi-wall carbon nanotube composites. Composite Interfaces, **10**, 389–404 (2003).
DOI: 10.1163/156855403771953650

[21] Legras R., Mercier J. P., Nield E.: Polymer crystallization by chemical nucleation. Nature, **304**, 432–434 (1983).
DOI: 10.1038/304432a0

[22] Bailly C., Daumerie M., Legras R., Mercier J. P.: Kinetics of the thermal degradation of anhydrous bisphenol-A polycarbonate/alkali metal arylcarboxylate systems in the melt. Macromolecular Chemistry and Physics, **187**, 1197–1214 (1986).
DOI: 10.1002/macp.1986.021870517

[23] Zhang X. F., Sreekumar T. V., Liu T., Kumar S.: Properties and structure of nitric acid oxidized single wall carbon nanotube films. Journal of Physical Chemistry B, **108**, 16435–16440 (2004).
DOI: 10.1021/jp0475988

[24] Simmons J. M., Nichols B. M., Baker S. E., Marcus M. S., Castellini O. M., Lee C. S., Hamers R. J., Eriksson M. A.: Effect of ozone oxidation on single-walled carbon nanotubes. Journal of Physical Chemistry B, **110**, 7113–7118 (2006).
DOI: 10.1021/jp0548422

eXPRESS Polymer Letters Vol.5, No.6 (2011) 526–534
Available online at www.expresspolymlett.com
DOI: 10.3144/expresspolymlett.2011.51

Dielectric properties of binary polyvinylidene fluoride/barium titanate nanocomposites and their nanographite doped hybrids

Y. C. Li[1,2], *S. C. Tjong*[1*], *R. K. Y. Li*[1]

[1]Department of Physics and Materials Science, City University of Hong Kong, Kowloon Town, Kowloon, Hong Kong
[2]Department of Materials Science and Engineering, Liaocheng University, Shandong, China

Received 8 October 2010; accepted in revised form 26 December 2010

Abstract. Binary polyvinylidene fluoride/barium titanate (PVDF/$BaTiO_3$) and its nanographite (GN) doped ternary nanocomposites were fabricated using a simple solution casting process followed by compression molding. The dielectric behavior of such hybrids over a wide frequency range was studied. Additions of GN with contents close to the percolation threshold were found to be very effective to enhance dielectric permittivity of the PVDF/$BaTiO_3$ nanocomposites. In this regard, the electrical behavior of ternary PVDF/$BaTiO_3$/GN hybrids can be explained in terms of the percolation theory. Furthermore, both dielectric constant and electrical conductivity of hybrids were found to be strongly frequency and temperature dependent.

Keywords: *nanocomposites, electrical properties, dielectric constant, graphite nanosheet*

1. Introduction

Ferroelectrics such as barium titanate ($BaTiO_3$), lead titanate ($PbTiO_3$) and lead zirconium titanate (PZT) with the perovskite crystal structure have gained considerable interest in industrial sectors. Ferroelectric ceramics exhibit excellent dielectric properties but poor mechanical performances. On the other hand, polymers possess good flexibility but low dielectric permittivity. Thus, combination ferroelectric fillers and polymer can overcome these deficiencies. Despite the advantages of being well processable, inexpensive and low dielectric loss, the dielectric constant of 0–3 composites remains unsatisfactory. For example, Venkatragavaraj *et al.* [1] incorporated PZT of high permittivity ($\varepsilon' = 1750$) into polyvinylidene fluoride (PVDF) ($\varepsilon' = 12$) using both solution-mixing and melt-blending processes. They found that the dielectric constant of resulting composites at room temperature is below 100 even at 50% filler loading. Such composites are ineffective to be used as materials for capacitors and transducers.

The dielectric properties of polymer-$BaTiO_3$ composites depend on several factors including the size and filler content as well as the interfacial bonding between the filler and polymer matrix [1–4]. In general, the dielectric permittivity of barium titanate degrades markedly when its grain size reduces from the micrometer down to nanometer level. A transition from tetragonal to cubic crystal structure occurs by refining its grain size to the nanometer regime [4]. The cubic phase of barium titanate exhibits low permittivity. In a recent study, Xie *et al.* [5] demonstrated that the addition of 50 vol% $BaTiO_3$ nanoparticles (100 nm) to polyimide only yield a dielectric constant of 35.

*Corresponding author, e-mail: aptjong@cityu.edu.hk

According to the literature, the dielectric constant of polymers filled with $BaTiO_3$ microparticles can be enhanced greatly by adding conducting metal and carbon black microparticles as well as vapor grown carbon fibers [6–8]. A significant rise in dielectric constant of such three-component 0–3 composites occurs near the percolation threshold. This is due to the formation of a large quantity of minicapacitors. The conducting fillers are in very close proximity to one another, but remain insulated by thin polymer surface layers. In this respect, conducting nanoparticles are anticipated to be more effective than their microparticle fillers to increase the permittivity of polymer composites.

Graphite is a polymorphic form of carbon consisting of graphene layers stacked along its long crystal axis. Sulfuric acid intercalant is incorporated into graphite interlayers, forming the so-called graphite intercalation compound (GIC). GIC is then subjected to rapid heating or thermal shock to release the intercalant, leading to the formation of expanded graphite (EG). The EG can be further exfoliated into graphite nanosheets of large aspect ratios under sonication. It is considered that graphite nanosheet additions are also beneficial in enhancing dielectric permittivity of PVDF/$BaTiO_3$ nanocomposites. In this study, binary PVDF/$BaTiO_3$ and ternary graphite nanosheet doped PVDF/$BaTiO_3$ nanocomposites were fabricated via solution mixing followed by compression molding. The purpose is to investigate the electrical responses of polymer composites filled with both conducting graphite nanosheets and insulating $BaTiO_3$ nanofillers.

2. Experimental

2.1. Materials

PVDF resin (Kynar 740) with a density of 1.78 g/cm^3 was supplied by Atofina Chemicals Inc. (Philadelphia, Pennsylvania, USA). Spherical barium titanate nanoparticles (85–128 nm) with density of 5.85 g/cm^3 were purchased from Nanostructured & Amorphous Materials Inc. (Houston, Texas, USA). Graphite nanosheet (GN) was supplied by Institute of Polymer and Nanomaterials, Huaqiao University (Quanzhou, China) [9]. The detailed fabrication method of GN was briefly described herein. Natural graphite flake with an average diameter of 500 μm was treated with concentrated sulfuric acid and fuming nitric acid (4:1, v/v) for several hours to produce GIC. Then, the resulting GIC was subjected to a thermal shock at ~1000°C in a furnace to yield EG. Finally, EG was exfoliated into GN in an alcohol-based solvent under sonication for several hours. The resulting GNs with a large aspect ratio of ~250 were collected and used in this study.

2.2. Fabrication of nanocomposites

PVDF was dissolved initially in a flask containing 15 wt% N,N-dimethylformamide (DMF) solvent. Barium titanate nanofillers of 10–60 wt% were then added to the mixed solution for fabricating PVDF/$BaTiO_3$ nanocomposites. To prepare three-component hybrid nanocomposites, the weight ratio of PVDF/$BaTiO_3$ was kept at 80/20. Graphite nanosheet of 1 to 4 phr was also added independently to the precursor solution. The nanocomposite solution was sonicated for 10 h and then heated at 70°C for solvent removal. The resulting products were dried and compression-molded at 220°C for 10 min.

2.3. Structural and electrical measurements

The microstructure of composites was observed in a scanning electron microscope (SEM, JEOL JSM-820, JEOL, Tokyo, Japan). A thin gold layer was sputter-coated onto the composite specimens prior to SEM observation. X-ray diffraction (XRD) measurements were performed using a Philip X'pert diffractometer (PANalytical, Almelo, The Netherlands) in the 2θ range of 2–50° at a scanning speed of 3°/min. Disk specimens for electrical measurements were coated with a silver paste. The frequency dependent electrical properties were measured with an impedance analyzer (Agilent model 4294 A, Agilent, Santa Clara, California, USA) at room temperature. Therefore, a complex permittivity of the composites can be obtained: $\varepsilon^* = \varepsilon' - j\varepsilon''$, where ε' is the real part of permittivity and ε'' is the dielectric loss. The impedance analyzer was equipped with a small furnace for measuring temperature dependent electrical properties. The heating rate of the furnace was maintained at 5°C/min.

3. Results and discussion

3.1. Dielectric responses of PVDF/$BaTiO_3$ composites

Figure 1 shows the variation of ε' with $BaTiO_3$ content for the PVDF/$BaTiO_3$ nanocomposites tested at a frequency of 1 kHz. It can be seen that the ε'

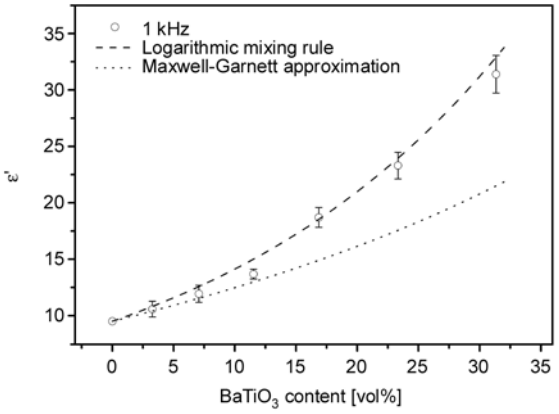

Figure 1. Dielectric constant vs $BaTiO_3$ contents for PVDF/$BaTiO_3$ nanocomposites

increases with increasing filler content. At 31.5 vol% $BaTiO_3$, ε' value reaches to 31.4, being ~3.5 times higher than that of neat PVDF. Theoretically, the dielectric responses of ceramic-polymer systems can be described by the logarithmic mixing rule and Maxwell–Garnett approximation [6, 10, 11]. Logarithmic mixing rule simply relates the permittivity of a composite to a combined dielectric effect of its individual constituents, see Equation (1):

$$\log\varepsilon_c' = x\log\varepsilon_f' + (1-x)\log\varepsilon_p' \quad (1)$$

Maxwell–Garnett approximation is applicable to the inclusions embedded in a continuum matrix of the polymer composite. Mathematically, the permittivity can be expressed by Eqution (2):

$$\varepsilon_c' = \varepsilon_p'\left(1 + \frac{3xA}{1-xA}\right) \quad (2)$$

where $A = (\varepsilon_f' - \varepsilon_p')/(\varepsilon_f' + 2\varepsilon_p')$, x denotes the volume fraction of $BaTiO_3$ filler, ε_c', ε_f', ε_p' denote the real part permittivity of the composite, $BaTiO_3$ and PVDF, respectively. Using $\varepsilon_f' = 500$, $\varepsilon_p' = 9.5$ and $f = 1$ kHz, Equation (1) and (2) are plotted as dash and dot curves respectively as shown in Figure 1. It is evident that the experimental data points obey the logarithmic mixing rule at high filler content while follow the Maxwell–Garnett approximation at low filler content.

Figure 2a–b shows the respective plots of ε' and tanδ vs frequency for the PVDF/$BaTiO_3$ nanocomposites. There exists a distinct enhancement in dielectric constant with increasing filler content while the loss tangent remains nearly the same. The ε' values of nanocomposites decrease with increasing frequency. A significant drop in ε′ occurs when

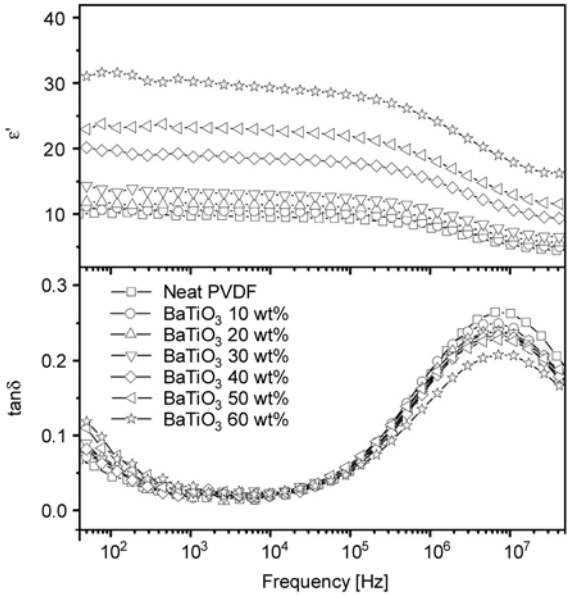

Figure 2. (a) Dielectric constant and (b) loss tangent as a function of frequency for PVDF and PVDF/$BaTiO_3$ nanocomposites

the frequency reaches to $3\cdot10^5$ Hz. This is attributed to the dipole relaxation of the composites lags behind the fast change of applied fields. In this regime, characteristic relaxation peaks of PVDF matrix can be observed (Figure 2b).

Figure 3a–b shows SEM images of the PVDF/$BaTiO_3$ 80/20 and PVDF/$BaTiO_3$ 50/50 nanocomposites. Barium titanate nanoparticles are found to disperse homogeneously in the matrix of nanocomposites prepared by means of solution mixing. A representative SEM image for the GN/$BaTiO_3$/PVDF 2.5/20/80 hybrid is shown in Figure 4.

Figure 5 shows XRD patterns of PVDF, $BaTiO_3$, PVDF/$BaTiO_3$ 80/20 and PVDF/$BaTiO_3$/GN 80/20/2.5 nanocomposites. The peaks located at 2θ = 18.5 and 20° are characteristic reflections of α-PVDF. A distinct peak at $2\theta = 26.6°$ is assigned to the (002) graphite characteristic reflection for the PVDF/BaTiO3/GN 80/20/2.5 nanocomposite. Barium titanate exhibits several diffraction peaks in the tested two-theta range. The peak at $2\theta = 45°$ clearly indicates the presence of cubic barium titanate.

As recognized, PVDF/$BaTiO_3$ composites filled with $BaTiO_3$ microparticles are well studied ceramic/polymer composite materials due to their high dielectric constant [12]. This is because $BaTiO_3$ microparticles with a tetragonal structure exhibit high permittivity. By refining the grain size of $BaTiO_3$ down to nanometer regime, its permittivity

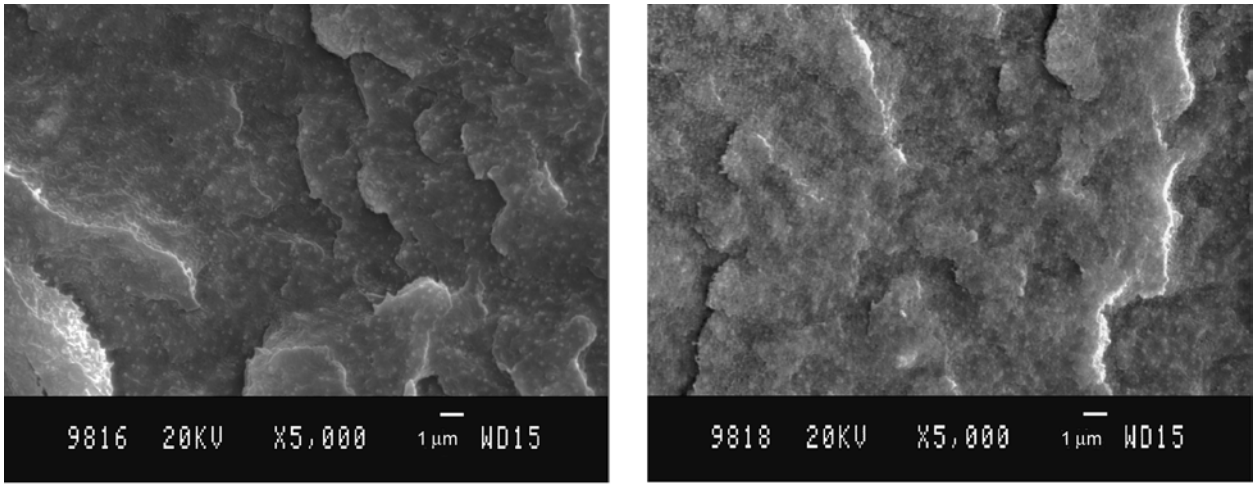

Figure 3. SEM micrographs of (a) PVDF/$BaTiO_3$ 80/20 and (b) PVDF/$BaTiO_3$ 50/50 nanocomposites

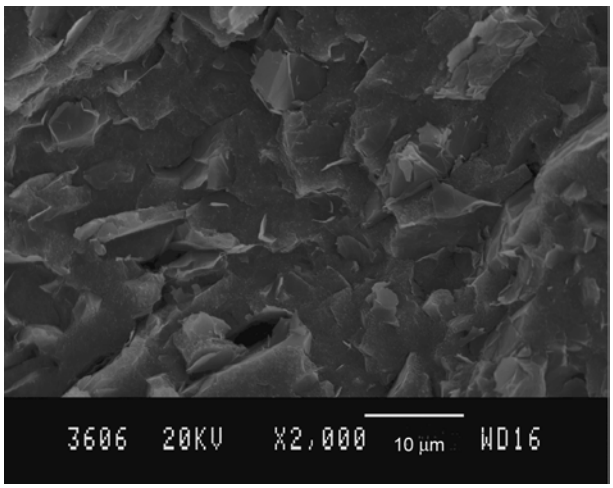

Figure 4. SEM image of PVDF/$BaTiO_3$/GN 80/20/2.5 hybrid

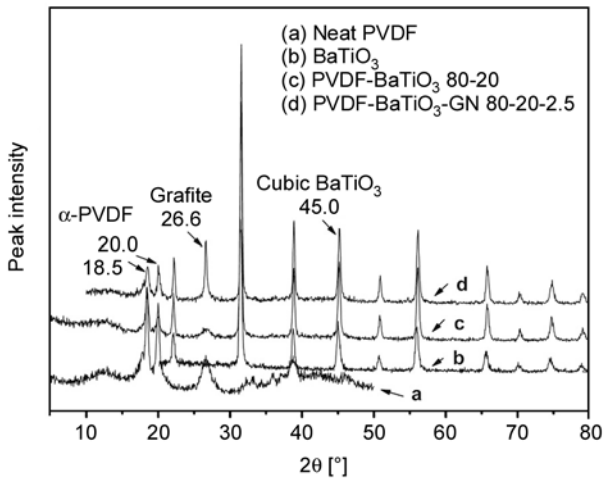

Figure 5. XRD patterns of (a) PVDF, (b) $BaTiO_3$, (c) PVDF/$BaTiO_3$ 80/20 composite, and (d) PVDF/$BaTiO_3$/GN 80/20/2.5 hybrid

reduces significantly owing to a transition from tetragonal (ferroelectric) to cubic structure with a low dielectric constant. Therefore, PVDF/$BaTiO_3$ nanocomposites require larger volume fractions of $BaTiO_3$ nanoparticles to achieve a higher permittivity [13, 14]. Table 1 lists the ε' and tanδ values of neat PVDF and representative PVDF/$BaTiO_3$ nanocomposites. Apparently, it requires 60 wt% $BaTiO_3$ nanoparticle (31.5 vol%) addition to PVDF to achieve a dielectric constant of 31.4. Very recently, Dou *et al.* [13] reported that $BaTiO_3$/PVDF nanocomposite exhibits a dielectric constant of ~29 by adding 50 wt% $BaTiO_3$ nanoparticle. Similarly, the dielectric constant of polyester-styrene resin can be increased from 9.2 to 25.0 by adding heat treated $BaTiO_3$ nanoparticle of 60 wt% (22 vol%). Heat treatment was employed in order to induce grain and particle growth as well as lattice relaxation of $BaTiO_3$ nanoparticles [15]. It appears that thermal treatment of $BaTiO_3$ nanoparticles has little effect in achieving large permittivity for the polymer nanocomposites. In this respect, we employed GN as a third component or hybrid filler to further enhance the permittivity of binary PVDF/$BaTiO_3$ nanocomposites.

Table 1. ε' and tanδ values for neat PVDF and its nanocomposites determined at 1 kHz

Specimen	ε'	tanδ
Neat PVDF	9.7	0.018
PVDF/$BaTiO_3$ 80/20	11.6	0.019
PVDF/$BaTiO_3$ 40/60	31.4	0.026
PVDF/$BaTiO_3$/GN 80/20/2.5	50.0	0.072
PVDF/$BaTiO_3$/GN 80/20/3	492.0	49.1

3.2. Electrical performance of GN/$BaTiO_3$/PVDF hybrids

Figure 6a shows dielectric responses of the PVDF/$BaTiO_3$/GN hybrids filled with low GN loading levels. Both the ε' and tanδ values increase slowly with increasing GN content up to 2.5 phr. Thereafter, they increase sharply as the GN content approaches the percolation threshold. The PVDF/$BaTiO_3$/GN 80/20/2.5 hybrid exhibits a large dielectric constant of 50 and low loss tangent of 0.072 at 1 kHz. The dielectric constant is four times larger than that of PVDF/$BaTiO_3$ 80/20 nanocomposite (~11.9). The PVDF/$BaTiO_3$/GN 80/20/2.5 hybrid also exhibits larger permittivity than the PVDF/$BaTiO_3$ 40/60 system (ε' = 31.4) as described above. In other words, $BaTiO_3$ content of the composite can be reduced markedly from 60 to 20 wt% by adding only 2.5 phr GN without sacrificing but rather improving the permittivity. The ε' and tan δ values of PVDF/$BaTiO_3$/GN 80/20/2.5 and PVDF/$BaTiO_3$/GN 80/20/3 hybrids are also listed in Table 1. An extremely large value of ε' = 492 can be achieved by adding 3 phr GN loading. However, this hybrid is unsuitable for energy storage applications due to its extremely large dielectric loss resulting from the formation of GN network. The formation of conducting network enables trapped carriers to pass through readily, thereby dissipating stored energy considerably. A sharp transition from an insulator to conductor can be also seen from the plot of electrical conductivity vs GN content (Figure 6b).

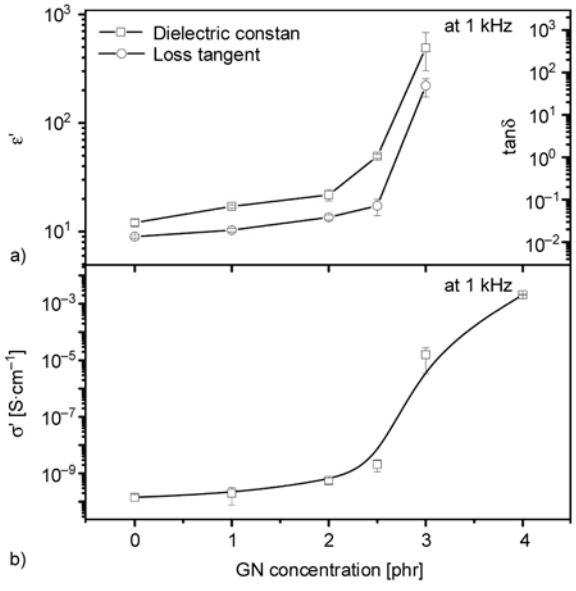

Figure 6. Variations of (a) dielectric constant and loss tangent, and (b) electrical conductivity with GN content for PVDF/$BaTiO_3$/GN hybrids

In fact, large permittivity is beneficial for enhancing energy density stored in a capacitor as given by the expression: $\eta = \varepsilon\varepsilon_o E^2/2$, where η is the stored energy density, ε the permittivity, and ε_o the vacuum permittivity (= $8.85 \cdot 10^{-12}$ F·m^{-1}) and E the applied field [16]. For instance, to generate an energy density of 0.1 J/cm^3, which is the value for the high performing piezoelectric ceramics, assuming a 50% energy conversion efficiency, the electric field required is 47.5 MV/m for a capacitor with a dielectric constant of 10 (permittivity of pure PVDF). For the composite materials with higher permittivity, the lower electrical field is needed to reach a required energy density. Since the permittivity of PVDF/$BaTiO_3$/GN 80/20/2.5 hybrid composite is 50, an electrical field of only 21.3 MV/m is needed to satisfy an energy density of 0.1 J/cm^3.

Figure 7a–c shows the frequency dependent dielectric constant, loss tangent and electrical conductivity of the PVDF/$BaTiO_3$/GN hybrids. It can be seen from Figure 7a that the ε' value of hybrids decreases with increasing frequency. For hybrids with higher GN loadings, the variation of dielectric constant with frequency is even more apparent. The incorporation of a conducting graphite phase into the PVDF/$BaTiO_3$ system affects its dielectric loss significantly, particularly at low frequency region (Figure 7b). The loss tangent increases dramatically by several orders of magnitude in the vicinity of percolation threshold, resulting from the formation of a conducting network. Figure 7c shows the variation of conductivity with frequency. The conductivity of hybrids with low GN contents increases linearly with frequency in a double logarithmic scale. Above the percolation threshold, a frequency independent conductivity or plateau predominates at the low frequency region. This is generally regarded as the dc conductivity. The electrical conductivity becomes frequency dependent when the frequency (f) approaches a critical value f_c (at σ = 110% σ_{dc}). In general, 'ac universal' law (see Equation (3)) can be used to describe electrical conducting behavior of hybrids:

$$\sigma_{ac}' = \sigma_{dc} + A\omega^u \tag{3}$$

where σ_{ac}', are σ_{dc} are the *ac* and *dc* conductivity of the composites, respectively; A is a temperature

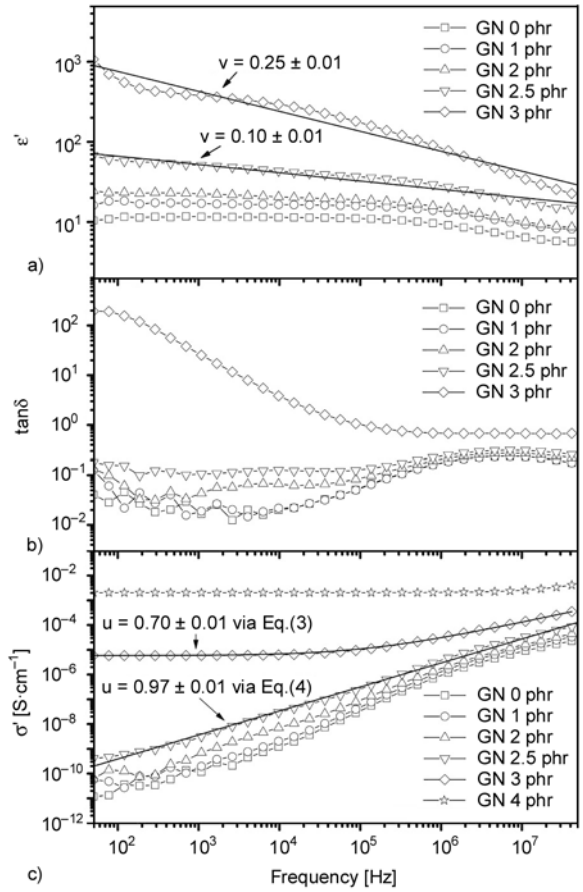

Figure 7. (a) Dielectric constant, (b) loss tangent and (c) conductivity as a function of frequency for PVDF/$BaTiO_3$/GN hybrids

dependant constant, u the critical exponent, and $\omega = 2\pi f$. Below the percolation threshold, the *dc* conductivity of composites is very small. Accordingly, the σ_{dc} term can be neglected and Equation (3) converts to: $\sigma_{ac}' = A\omega^u$. Therefore, '*ac* universal' law can predict the conducting behavior of composites with filler content above the percolation threshold more accurately. A representative fitting curve for the PVDF/$BaTiO_3$/GN 80/20/3 hybrid is shown in Figure 7c. A critical exponent $u = 0.70$ is obtained accordingly.

The ac conductivity and dielectric constant of composites in the vicinity of the percolation threshold generally follow the power law relation [17], see Equations (4) and (5):

$$\sigma'(f,\phi_c) \propto \omega^u \quad (4)$$

$$\varepsilon'(f,\phi_c) \propto \omega^{-v} \quad (5)$$

where v is a critical exponent that obeys the relation $u + v = 1$. The σ' data of PVDF/$BaTiO_3$/GN 80/20/2.5 and PVDF/$BaTiO_3$/GN 80/20/3 hybrids can be best fitted using Equations (4) and (3) that prevail near and above the percolation threshold (Figure 7c). The u values for PVDF/$BaTiO_3$/GN 80/20/2.5 and PVDF/$BaTiO_3$/GN 80/20/3 hybrids are 0.97 and 0.7 respectively. The fitting curves and v values for dielectric constant of these two hybrids are shown in Figure 7a. The solid fitting curve for the PVDF/$BaTiO_3$/GN 80/20/3 hybrid using Equation (5) shows a slight deviation from experimental data. As mentioned above, Equation (5) prevails near the percolation threshold and the GN content of this composite is higher than the threshold. By reducing GN content to 2.5, the solid curve of PVDF/$BaTiO_3$/GN 80/20/2.5 hybrid agrees reasonably with experimental data. The $u + v$ values for PVDF/$BaTiO_3$/GN 80/20/2.5 and PVDF/$BaTiO_3$/GN 80/20/3 hybrids are 1.07 and 0.95, respectively, which obey closely the power law criterion.

3.3. The effect of temperature

Figure 8a shows temperature dependent dielectric constant of PVDF, PVDF/$BaTiO_3$ 80/20 nanocomposite and their representative hybrids. For neat PVDF, the dielectric constant displays two distinct relaxation regions, showing transitions from low to high temperatures. These correspond to its β- and α-relaxation processes [18]. The α-relaxation in this spectrum is associated with the molecular motion of

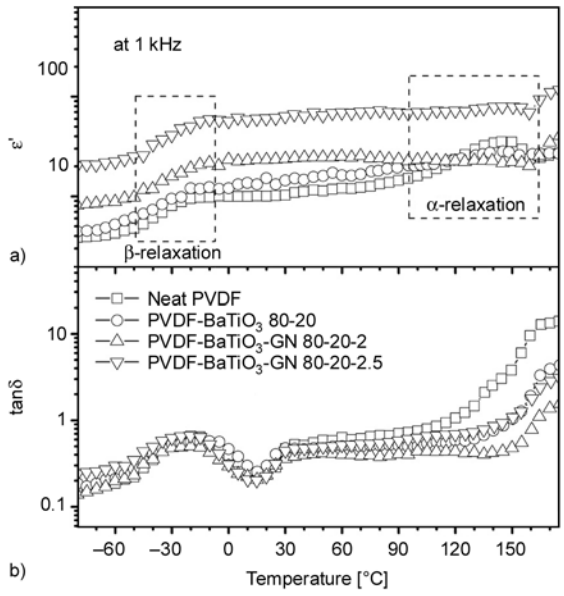

Figure 8. Dielectric constant and loss tangent vs temperature plots for PVDF, PVDF/$BaTiO_3$ 80/20 nanocomposite and their hybrids

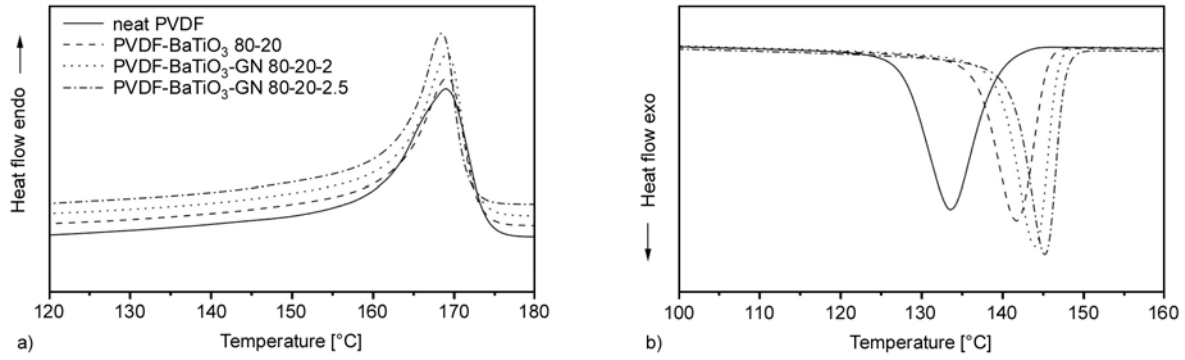

Figure 9. DSC (a) heating and (b) cooling curves for PVDF, PVDF/$BaTiO_3$ 80/20 nanocomposite and their hybrids

PVDF matrix near the melting temperature (T_m), while the β-relaxation is due to the segment movement of PVDF chains near T_g. The effect of filler additions on these relaxations can be clearly seen in the plots of dielectric loss vs temperature (Figure 8b). The α-relaxation peak intensity of the PVDF/$BaTiO_3$ 80/20 nanocomposite decreases by adding barium titanate.

Figure 9 shows DSC heating and cooling curves for PVDF, PVDF/$BaTiO_3$ 80/20 nanocomposite and representative hybrids. These measurements were determined using a differential scanning calorimeter (Perkin model 2910) under a rate of 10ºC/min in a protected nitrogen atmosphere. The melting temperature of PVDF shows little changes by adding barium titanate and graphite nanosheet. However, a distinct increase in the crystallization temperature of PVDF is observed due to the nanofiller additions. This implies an effective nucleating effect of barium titanate and graphite nanosheet for the molecular chains of PVDF during the crystallization process.

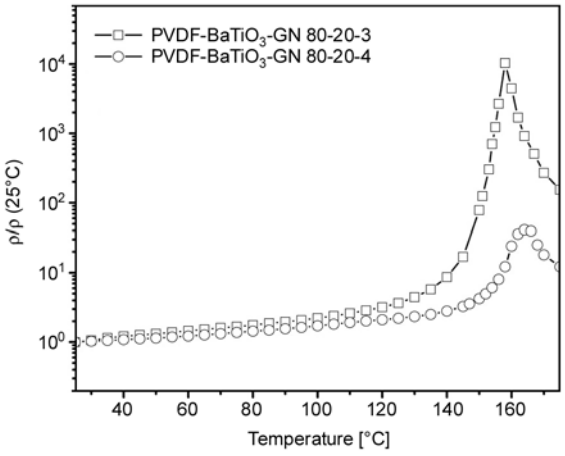

Figure10. Normalized resistivity vs temperature plots for PVDF/$BaTiO_3$/GN 80/20/3 and PVDF/$BaTiO_3$/GN 80/20/4 hybrids

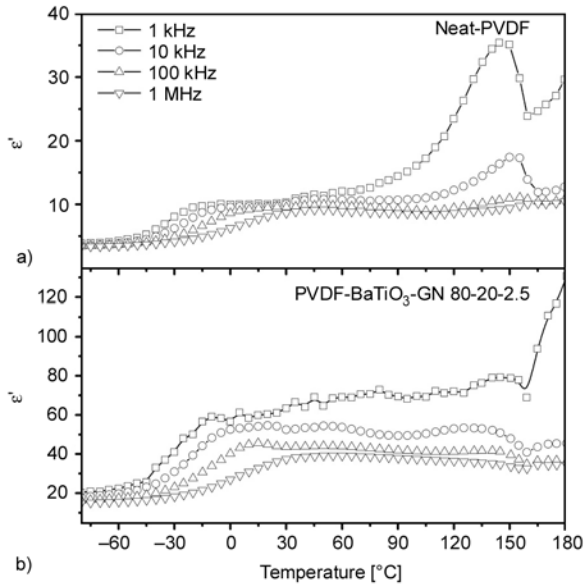

Figure 11. Variation of dielectric constant with temperature at different frequencies for (a) neat PVDF and (b) PVDF/ $BaTiO_3$/GN 80/20/2.5 hybrid

The variation of resistivity (reciprocal of conductivity), normalized to that at 25°C, with temperature of PVDF/$BaTiO_3$/GN 80/20/3 and PVDF/$BaTiO_3$/GN 80/20/4 hybrids is shown in Figure 10. It is seen that the normalized resistivity of hybrids increases slowly with increasing temperature up to the vicinity of T_m, follows by a sharp increase at T_m. Such an increase in resistivity before T_m is commonly seen in many conducting polymers. This behavior is generally known as the positive temperature coefficient (PTC) effect that is mainly associated with thermal expansion of the polymer matrix. Moreover, the PTC peak intensity tends to decrease with increasing GN content. Due to the thermal expansion of polymer matrix, the distance between graphite nanosheets increases markedly. Thus, the interconnecting conduction paths within the polymer matrix are disturbed accordingly.

Figure 11a–11b illustrates the change in ε' with temperature under different frequencies for neat PVDF and the PVDF/$BaTiO_3$/GN 80/20/2.5 hybrid, respectively. It can be seen that the dielectric constant decreases with increasing frequency for both specimens. Furthermore, both the onset temperature of α- and β-relaxation peaks shifts to higher temperatures with increasing frequency.

4. Conclusions

In summary, binary PVDF/$BaTiO_3$ nanocomposites and ternary PVDF/$BaTiO_3$/GN hybrids were fabricated using solution mixing followed by compression molding. Electrical measurements showed that the real part of permittivity of PVDF/$BaTiO_3$ nanocomposites increases with increasing $BaTiO_3$ content. Moreover, the incorporation of low loading levels of graphite nanosheets to the PVDF/$BaTiO_3$ system led to a significant enhancement in dielectric permittivity, especially at the percolation threshold. The ε' value of the PVDF/$BaTiO_3$/GN 80/20/2.5 hybrid was 50, being four times higher than that of the PVDF/$BaTiO_3$ 80/20 nanocomposite. Finally, the electrical behavior of nanographite doped PVDF/$BaTiO_3$ composites can be well interpreted using the percolation theory. In addition, the dielectric constant and conductivity of the composites were strongly dependent on temperature.

References

[1] Venkatragavaraj E., Satish B., Vinod P. R., Vijaya M. S.: Piezoelectric properties of ferroelectric PZT-polymer composites. Journal of Physics D: Applied Physics, **34**, 487–492 (2001).
DOI: 10.1088/0022-3727/34/4/308

[2] Dang Z-M., Zheng Y., Xu H-P.: Effect of the ceramic particle size on the microstructure and dielectric properties of barium titanate/polystyrene composites. Journal of Applied Polymer Science, **110**, 3473–3479 (2008).
DOI: 10.1002/app.28856

[3] Ramajo L., Castro M. S., Reboredo M. M.: Effect of silane as coupling agent on the dielectric properties of $BaTiO_3$-epoxy composites. Composites Part A: Applied Science and Manufacturing, **38**, 1852–1859 (2007).
DOI: 10.1016/j.compositesa.2007.04.003

[4] Arit G., Hennings D., de With G.: Dielectric properties of fine-grained barium titanate ceramics. Journal of Applied Physics, **58**, 1619–1625 (1985).
DOI: 10.1063/1.336051

[5] Xie S-H., Zhu B-K., Wei X-Z., Xu Z-K., Xu Y-Y.: Polyimide/$BaTiO_3$ composites with controllable dielectric properties. Composites Part A: Applied Science and Manufacturing, **36**, 1152–1157 (2005).
DOI: 10.1016/j.compositesa.2004.12.010

[6] Dang Z-M., Shen Y., Nan C-W.: Dielectric behavior of three-phase percolative Ni–$BaTiO_3$/polyvinylidene fluoride composites. Applied Physics Letters, **81**, 4814–4816 (2002).
DOI: 10.1063/1.1529085

[7] Tchmutin I. A., Ponomarenko A. T., Shevchenko V. G., Ryvkina N. G., Klason C., Mcqueen D. H.: Electrical transport in 0-3 epoxy resin–barium titanate–carbon black polymer composites. Journal of Polymer Science Part B: Polymer Physics, **36**, 1847–1856 (1998).
DOI: 10.1002/(SICI)1099-0488(199808)36:11<1847::AID-POLB6>3.0.CO;2-N

[8] Zhang C., Sheng J. F., Ma C. A., Sumita M.: Electrical and damping behaviors of CPE/$BaTiO_3$/VGCF composites. Materials Letters, **59**, 3648–3651 (2005).
DOI: 10.1016/j.matlet.2005.07.004

[9] Chen G., Weng W., Wu D., Wu C., Lu J., Wang P., Chen X.: Preparation and characterization of graphite nanosheets from ultrasonic powdering technique. Carbon, **42**, 753–759 (2004).
DOI: 10.1016/j.carbon.2003.12.074

[10] Kulek J., Szafraniak I., Hilczer B., Połomska M.: Dielectric and pyroelectric response of PVDF loaded with $BaTiO_3$ obtained by mechanosynthesis. Journal of Non-Crystalline Solids, **353**, 4448–4452 (2007).
DOI: 10.1016/j.jnoncrysol.2007.02.077

[11] Cheng K-C., Lin C-M., Wang S-F., Lin S-T., Yang C-F.: Dielectric properties of epoxy resin-barium titanate composites at high frequency. Materials Letters, **61**, 757–760 (2007).
DOI: 10.1016/j.matlet.2006.05.061

[12] Dang Z-M., Wang Y-H., Peng B., Nan C-W.: Effect of $BaTiO_3$ size on dielectric property of $BaTiO_3$/PVDF composites. Journal of Electroceramics, **21**, 381–384 (2008).
DOI: 10.1007/s10832-007-9201-8

[13] Dou X., Liu X., Zhang Y., Feng H., Chen J-F., Du S.: Improved dielectric strength of barium titanate-polyvinylidene fluoride nanocomposite. Applied Physics Letters, **95**, 132904(1)–132904(3) (2009).
DOI: 10.1063/1.3242004

[14] Dang Z-M., Wang H-Y., Zhang Y-H., Qi J-Q.: Morphology and dielectric property of homogenous $BaTiO_3$/PVDF nanocomposites prepared via the natural adsorption action of nanosized $BaTiO_3$. Macromolecular Rapid Communications, **26**, 1185–1189 (2005).
DOI: 10.1002/marc.200500137

[15] Schumacher B., Geßwein H., Haußelt J., Hanemann T.: Temperature treatment of nano-scaled barium titanate filler to improve the dielectric properties of high-k polymer based composites. Microelectronic Engineering, **87**, 1978–1983 (2010).
DOI: 10.1016/j.mee.2009.12.018

[16] Huang C., Zhang Q.: Enhanced dielectric and electromechanical responses in high dielectric constant all-polymer percolative composites. Advanced Functional Materials, **14**, 501–506 (2004).
DOI: 10.1002/adfm.200305021

[17] Bergman D. J., Imry Y.: Critical behavior of the complex dielectric constant near the percolation threshold of a heterogeneous material. Physical Review Letters, **39**, 1222–1225 (1977).
DOI: 10.1103/PhysRevLett.39.1222

[18] Dang Z-M., Yan W-T., Xu H-P.: Novel high-dielectric-permittivity poly(vinylidene fluoride)/polypropylene blend composites: The influence of the poly(vinylidene fluoride) concentration and compatibilizer. Journal of Applied Polymer Science, **105**, 3649–3655 (2007).
DOI: 10.1002/app.26447

eXPRESS Polymer Letters Vol.5, No.6 (2011) 535–544
Available online at www.expresspolymlett.com
DOI: 10.3144/expresspolymlett.2011.52

Tailor-made starch-based conjugates containing well-defined poly(vinyl acetate) and its derivative poly(vinyl alcohol)

D. R. Lu, C. M. Xiao, S. J. Xu, Y. F. Ye*

College of Material Science and Engineering of Huaqiao University, Quanzhou, 362021, China

Received 19 October 2010; accepted in revised form 26 December 2010

Abstract. Reversible addition-fragmentation chain transfer (RAFT) polymerization was adopted to synthesize starch-based conjugates that possessed controllable architecture and properties. Starch-based xanthate agent was prepared and applied as chain transfer agent to conduct the living/controlled polymerization (LCP) of vinyl acetate, which generated tailor-made conjugates of starch and well-defined poly(vinyl acetate) (SVAc). The relevant derivatives, conjugates of starch and chain length-controlled poly(vinyl alcohol) (SVA), were obtained subsequently. Various characterizations such as Fourier transform infrared spectra (FTIR), ultraviolet-visible spectroscopy (UV), proton nuclear magnetic resonance (^{1}H NMR), gel permeation chromatography (GPC), X-ray diffraction (XRD), Thermogravimetric analysis (TGA), and dynamic mechanical thermal analysis (DMTA) were performed to examine the structure of intermediates and the starch-based conjugates. Static contact angle measurements revealed that the hydrophilic character of starch-based conjugates was tunable. Well-defined SVAc was amphiphilic and it was able to self-assemble into size controllable micelles, which was verified by contact angles, transmission electron microscopy (TEM) and dynamic light scattering (DLS) tests. SVA exhibited much higher capability to form physically cross-linked hydrogel than starch did. Both the characteristic of SVAc and SVA were chain length-dependent.

Keywords: *tailor-made polymers, starch, vinyl acetate, synthesis, properties*

1. Introduction

Being challenged with environmental and petroleum resources issues, polymers from renewable resources are considered as the future macromolecular materials [1]. Starch is an annually renewable and biodegradable agriculturally derived polysaccharide. It has been receiving growing attention for decades, and is regarded as a promising candidate for developing sustainable materials [2]. Poly(vinyl alcohol) (PVA) is a water soluble synthetic polymer that exhibits several advantages such as biodegradability, biocompatibility and capacity of forming physically cross-linked hydrogel under mild condition [3–4]. Combination of starch and PVA has been mainly documented as the relevant blend [5] and graft copolymer [6].

It is well known that the structure and function of polymers are intimately related. Subtle modulation of chain architecture probably generates new materials with dramatically different properties [7]. Among the tools to define polymers well, reversible addition-fragmentation chain transfer (RAFT) polymerization is a facile, convenient and versatile approach to prepare functionalized polymers with controlled architecture [8–9]. It may be an effective way for combining the advantages of starch and PVA components with controllable macromolecular architectures. As a natural polymer, the structure of

*Corresponding author, e-mail: congmingxiao@hqu.edu.cn

starch is unavailable to be controlled [10]. Thus, one feasible strategy is to attach the precisely tailor-made PVA onto starch.

As well known, PVA is easy to be derived from saponification of poly(vinyl acetate) (PVAc). Moreover, Stenzel and her coworkers have revealed that RAFT/MADIX (macromolecular design via interchange of xanthates) polymerization enables the monomer VAc to polymerize in a controlled manner [11]. McLeary group has performed the grafting copolymerization of VAc onto two derivatives of cellulose via RAFT polymerization [12]. But rare attention has been paid to the RAFT polymerization of VAc using abundant starch as substrate [13]. These facts encourage us to conduct the research on conjugating starch with well-defined PVA. This article aims at tailoring the synthesis and properties of starch-based conjugates. Herein, starch-based xanthate-mediated living radical polymerization of VAc and subsequent alcoholysis were carried out to generate two kinds of conjugates. The properties of the conjugates were investigated to find out the characters of the starch-based polymers.

2. Experimental

2.1. Materials

Water-soluble starch (Shanghai Chemical Agents Ltd. Co., China) was dried before use. Vinyl acetate (VAc, Shanghai Chemical Agents Ltd. Co., China) was purified by distillation. Maleic anhydride (MAn, m.p. 54–55°C, Shanghai Chemical Agents Ltd. Co., China) and N,N′-Azobisisobutyronitrile (AIBN, Shanghai Chemical Agents Ltd. Co., China) were purified by recrystallizing from benzene (Shanghai Chemical Agents Ltd. Co., China) and anhydrous ethanol (Shanghai Chemical Agents Ltd. Co., China) respectively. Carbon disulfide (Shanghai Chemical Agents Ltd. Co., China) was dried by anhydrous magnesium sulfate (Shanghai Chemical Agents Ltd. Co., China) before used. Dimethyl sulfoxide (DMSO, Shanghai Chemical Agents Ltd. Co., China), anhydrous ethanol, 95% ethanol (Shanghai Chemical Agents Ltd. Co., China), methanol (Shanghai Chemical Agents Ltd. Co., China), sodium hydroxide (Shanghai Chemical Agents Ltd. Co., China), potassium hydroxide (Shanghai Chemical Agents Ltd. Co., China), pyridine (Shanghai Chemical Agents Ltd. Co., China), N,N′-Dimethylformamide (DMF, Shanghai Chemical Agents Ltd. Co., China), potassium ethyl xanthogenate (Shanghai Chemical Agents Ltd. Co., China) and hydrochloric acid (HCl, Shanghai Chemical Agents Ltd. Co., China) were all analytical grade reagents and used as received.

2.2. Synthesis of starch-based xanthate agent

Firstly, unsaturated starch-based macromonomer (SM) was prepared according to the literature [14] by the esterification between starch and MAn. Briefly, 24 g dry starch was dissolved in 28 ml water at 100°C, mixed with 60 ml DMF and transferred into a 250 ml flask. A mixture of 24 g MAn, 24 ml pyridine and 60 ml DMF was added into the flask in droplet under stirring. The reaction mixture was allowed to react for 24 h with agitation at room temperature. The crude product was precipitated from 95% ethanol and purified by extracting with 95% ethanol in a Soxhlet apparatus for 24 h. The dried light yellow powder was pure SM. Yield: 65%. Carbon-carbon double bond percentage: 22.5% (calculated from titration results). FTIR (KBr, cm^{-1}): 3450 (–OH), 2931 (–CH_2–, –CH_3), 1732 (–C=O), 1638 (–C=C–).

Starch-based xanthate agent (SXA) was prepared according to the literature [15] with some improvements. Briefly, 10 g SM was dissolved in 40 ml DMSO at 80°C. The solution and proper amount of acetic acid were added into a 100 ml round-bottom flask. Constant HBr gas was bubbled through the solution and the mixture was kept stirring for 24 h at 60°C. Then 10 g potassium ethyl xanthogenate was added and the mixture was allowed to react for another 24 h. After isolating the by-product KBr by filtration, the crude product was precipitated from 200 ml anhydrous ethanol and purified by 24 h-extraction with ethanol in a Soxhlet apparatus. The dried dark yellow powder was SXA. Yield: 55%. FTIR (KBr, cm^{-1}): 3425 (–OH), 2924 (–CH_2–, –CH_3), 1042 (–C=S). UV (C=S): 385 nm ($n \rightarrow \pi^*$, λ_{max}), 300 nm ($n \rightarrow \pi^*$, λ), H_2O as solvent. ^1H NMR (D_2O, δ ppm): 1.12 (a: O–CH_2–C$\boldsymbol{H}_3$, 3H, t), 2.59 (d: CH–C$\boldsymbol{H}_2$–OCO–, 2H, d), 4.06 (c: –CH_2–C$\boldsymbol{H}$(S)–C=O, 1H, d), 4.43 (e: O–C$\boldsymbol{H}_2$–CH, 2H, d, on starch), 4.86 (b: O–C$\boldsymbol{H}_2$–CH_3, 2H, q), 5.01, 5.31 and 3.2–3.7 (f: protons on starch backbone).

2.3. SXA-mediated VAc RAFT polymerization

To prepare conjugates (SVAc) of starch and molecular weight-controlled poly(vinyl acetate), the RAFT polymerization of VAc mediated via starch-based xanthate agent was conducted [11]. Briefly, 0.1 g SXA was dissolved in 6 ml DMSO at 80°C, and cooled down to room temperature, then a mixture of 0.04 g AIBN and 4 ml VAc was added dropwise. The mixture was transferred into a Schlenk tube which was thoroughly deoxygenated by three consecutive freeze-pump-thaw cycles. Several tubes were kept at 60°C water bath and removed at regular time intervals. The reactions were terminated by plunging the tubes into iced water. SVAc was precipitated from plenty of water, filtered, washed with water for three times, and dried. The samples were extracted with anhydrous ethanol for 48 h to remove the homopolymer. The conversion of monomer was determined by gravimetric method. FTIR (KBr, cm^{-1}): 3455 (–OH), 2931 (–CH_2–, -CH–), 1754 (–C=O). ^{1}H NMR ($CDCl_3$, δ ppm): 1.26 (a: O–CH_2–C***H***$_3$, 3H, t), 1.64–1.94 (e: –C***H***$_2$–CH, 2H, t, in PVAc moiety), 1.96–2.12 (c: –OCO–C***H***$_3$, s, in PVAc moiety), 2.64 (f: CH–C***H***$_2$–OCO–, 2H, d), 4.09 (g: CH_2–C***H***–COOH, 1H, t), 4.46 (h: O–C***H***$_2$–CH, 2H, d, on starch), 4.72 (b: O–C***H***$_2$–CH_3, 2H, q), 4.82–5.05 (d: –OCO–C***H***–CH_2–, 1H, m, in PVAc moiety), 5.23, 5.43, and 3.3–3.8 (i: protons on starch backbone).

2.4. Physical formation of SVAc micelles and SVA hydrogel

A predetermined amount of SVAc was dissolved in THF to obtain 0.004 g/ml solution, and then 1 ml SVAc/THF solution was added into 10 ml water slowly with vigorous stirring and kept at room temperature for 12 h. THF was removed and the SVAc micelles were formed. The final concentration of SVAc micellar solution was $4 \cdot 10^{-4}$ g/ml.

The conjugates (SVA) of starch and chain length-controlled PVA were obtained by alcoholysis of SVAc. Briefly, A mixture of 2.0 g SVAc and 15 ml 5 wt% NaOH/methanol was kept refluxing for 2 h. The yellowish-white SVA powder was filtered and dried.

To form physically cross-linked hydrogel, the aqueous solution of 10 wt% SVA was subjected to three repeated freezing/thawing cycles, 24 h at –16°C and 3 h at ambient temperature.

2.5. Characterizations

The powdered SM, SXA, SVAc and SVA were mixed with dry KBr and compressed into disks respectively. Fourier transform infrared spectra (FTIR) of the samples were recorded using a Nexus 470 FTIR spectrometer (Thermo Fisher Scientific, Waltham, MA, USA). The thio-carbonyl bond (–C=S) in the structure of SXA was identified with Shimadzu UV-2450 UV-Visible spectrometer (Shimadzu Corporation, Kyoto, Japan). ^{1}H NMR spectra of SXA, SVAc and the hydrolysis product of SVAc were recorded on a Bruker AV400 NMR spectrometer (Bruker BioSpin, Rheinstetten, Germany) using D_2O, DMSO-d_6 and $CDCl_3$ as solvent respectively. Thermogravimetric analysis (TGA) of the SM, SVAc and SVA were performed with a TA V2.4F thermoanalyzer (Thermo Fisher Scientific, Waltham, MA, USA). Analyses were conducted over the temperature range from 25 to 800°C with a programmed temperature increment of 20°C/min under N_2 atmosphere. A mixture of 0.5 g SVAc, 10 ml 1M HCl and 10 ml THF was kept refluxing for 6 days to remove starch component completely. Then the apparent molecular weight and polydispersity index (PDI) of the acidic hydrolysis remainder were measured on a Waters gel permeation chromatography (GPC) with three linear Styragel columns, Waters 1515 pump, and Waters 2414 differential refractive index detector at 30°C (Waters Corporation, Milford, MA, USA). THF was used as eluent at a flow rate of 1.0mL/min and polystyrene standards were employed for calibration.

Static contact angle of water on SVAc with defined PVAc, starch, and PVAc films was measured with a JC-2000C contact angle analyzer (Shanghai Zhongchen Digital Technique Equipment Co. Ltd, Shanghai, China), an average of five measurements was taken. The surface morphology of the films was observed with Hitachi S-3500N scanning electron microscope (SEM, Hitachi High-Tech, Tokyo, Japan) at the acceleration voltage of 15 kV. For TEM observation [16], about 0.02 ml SVAc micellar solution was deposited on a carbon-coated electron microscopy copper grid. Water was evaporated at ambient temperature and atmospheric pressure. The morphology of the micelles was measured with Hitachi H-7650 TEM (Hitachi High-Tech, Tokyo, Japan) at an acceleration voltage of 80 kV. The size of SVAc micelles was measured using a Brookhaven

Instruments Corporation (Holtsville, NY) ZetaPlus dynamic light scattering (DLS) apparatus at scattering angle of 90° at 25°C.

X-ray diffraction (XRD) profiles of the dried SVA hydrogel powder were collected with a Bruker D8-Advanced diffractometer (Bruker AXS Inv., Madison WI, USA) using Nickel-filtered Cu-K_α radiation (k = 0.15406 nm) and scanned from 2 to 60° at a scan speed of 3°/min. The viscoelastic properties of the SVA hydrogels were investigated using a dynamic mechanical thermal analysis instrument (DMTA IV, Rhemoteric Scientific Inc., Piscataway, NJ, USA) with compression mode at 25°C [17].

3. Results and discussion

3.1. Synthesis of intermediate and controlled polymerization

Incorporation of PVA will greatly improve the processability, mechanical strength and other properties of starch [18–19], which has been achieved by either radical graft copolymerization or blending means. However, to our best knowledge, no report has mentioned about tuning the architecture and property of starch-based polymers with well-defined PVA so far. RAFT polymerization has the potential to be a key living/controlled polymerization (LCP) method for highly value added fields or large scale applications [20]. Especially it is suitable for synthesizing PVAc, the precursor of PVA, with controlled molecular weight and molecular weight distribution [11]. In view of these, the strategy that performs RAFT polymerization of VAc in the presence of starch-based RAFT agent is adopted to integrate starch and PVA with defined macromolecular architectures.

Two steps are involved in synthesis of starch-based RAFT agents (Figure 1). Macromonomer SM contains 22.5% C=C is derived from the esterification of starch and MAn. By using acetic acid as catalyst, the addition of HBr to the double bonds on SM is easily to be carried out. Then the bromium atoms are substituted with xanthogenate groups to obtain SXA. Though two forms of SXA may be formed, both of them contain the xanthogenate functional groups. No matter which one is the major product, either is available to conduct the expected starch-based xanthate-mediated living radical polymerization of VAc. According to the Markovnikov addition principle, the probable major intermediates and the target product are 3, 5 and 7.

The structures of SM and SXA are confirmed with FTIR (Figure 2), UV and ^{1}H NMR (Figure 3a). The characteristic absorption bands on the FTIR spectra of SM at 1732 and 1638 cm^{-1} are attributed to the stretching vibration of –C=O and C=C. An absorption peak appears at 1042 cm^{-1} on the FTIR spectra and UV absorptions of thio-carbonyl bond (–C=S) exhibit at 300 and 38 nm, which verify the samples contain –C=S groups. In addition, the ^{1}H NMR analysis results also demonstrate SXA has been synthesized successfully. The proton signals at 4.43, 5.01, 5.31 and 3.2~3.7 ppm belong to the

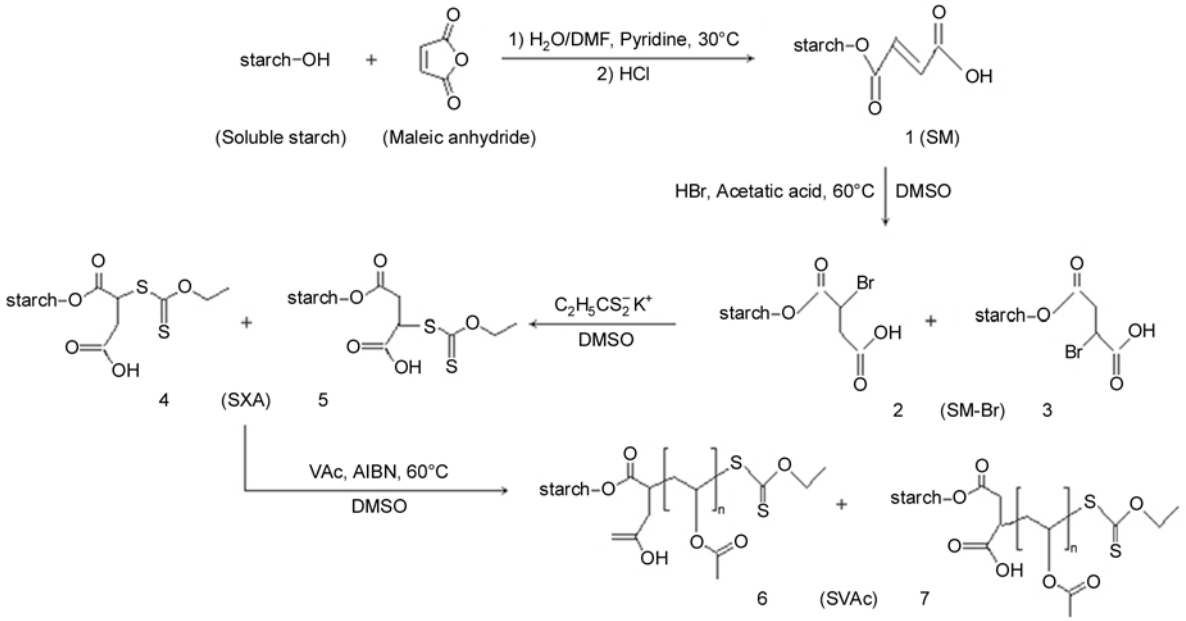

Figure 1. Route of controlled incorporation of well-defined PVAc onto starch via RAFT polymerization

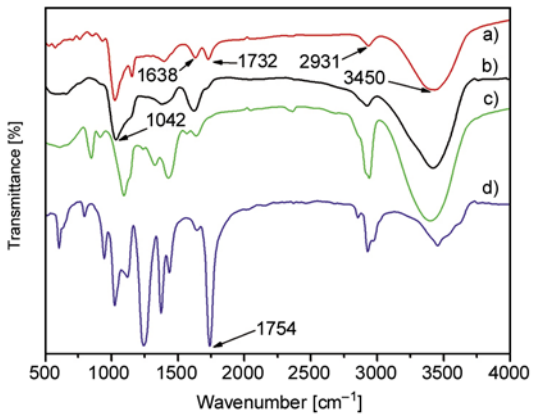

Figure 2. FTIR spectra of SM (a), SXA (b), SVA (c) and SVAc (d)

starch backbone. And the peaks at 1.12, 4.06 and 4.86 ppm indicate that xanthogenate group has been bonded onto starch backbone.

Owing to the characteristic structure of VAc monomer, few RAFT agents are available for its controlled polymerization [21]. Fortunately, polysaccharides can be played as a leaving group to mediate the RAFT polymerization [12, 22–23]. The utilization of polysaccharides-based RAFT agent not only retains the characteristics of natural polymers, but also forms well-defined structure. In current study, SXA is used as macro-RAFT agent and the controlled polymerization of VAc is carried out as expected. The enhanced absorption peak at 1754 cm^{-1} on the FTIR spectra of corresponding polymer (Figure 2) is attributed to carbonyl group, which suggests that the sample is the target product SVAc. On the FTIR spectra of the alcoholysis derivatives of SVAc (Figure 2), the characteristic absorption band of carbonyl group has disappeared whereas the absorption band of hydroxyl group is strengthened. This proof indicates that SVAc has converted into SVA completely. ^{1}H NMR spectra (Figure 3b) also verify the structure of SVAc. The signs at 1.64~1.94, 1.96~2.12 and 4.82~5.05 ppm are related to the protons on PVAc chain. The peaks at 2.64, 4.09, 4.46, 3.3–3.8, 5.23 and 5.43 ppm belong to that on the starch segment. And the protons of xanthogenate group show their chemical shifts at 1.26 and 4.72 ppm.

Figure 4 exhibits the thermal degradation profiles of SM, SVAc and SVA. Their thermal stabilities also reveal the success of the polymerization and alcoholysis reaction. The initial difference of weight loss among SM, SVAc and SVA reflects their water content or hydrophilicity variance. It is found that both SVAc and SVA show two degradation platforms. The first stages (200–350°C) are assigned to both the decomposition of SM backbone and PVAc segments, and the second ones (390–480°C) are related to the PVAc or PVA moiety [24]. Since both SM and SVA contain more hydroxyl groups than SVAc, and there are carboxyl groups on the backbone of SM, the ability to form intermolecular hydrogen-bond is in the following order: SM > SVA > SVAc. As a result, the final residual weight fraction of the samples is in the same order. These phenomena confirm the structures of SM, SVAc and SVA once more.

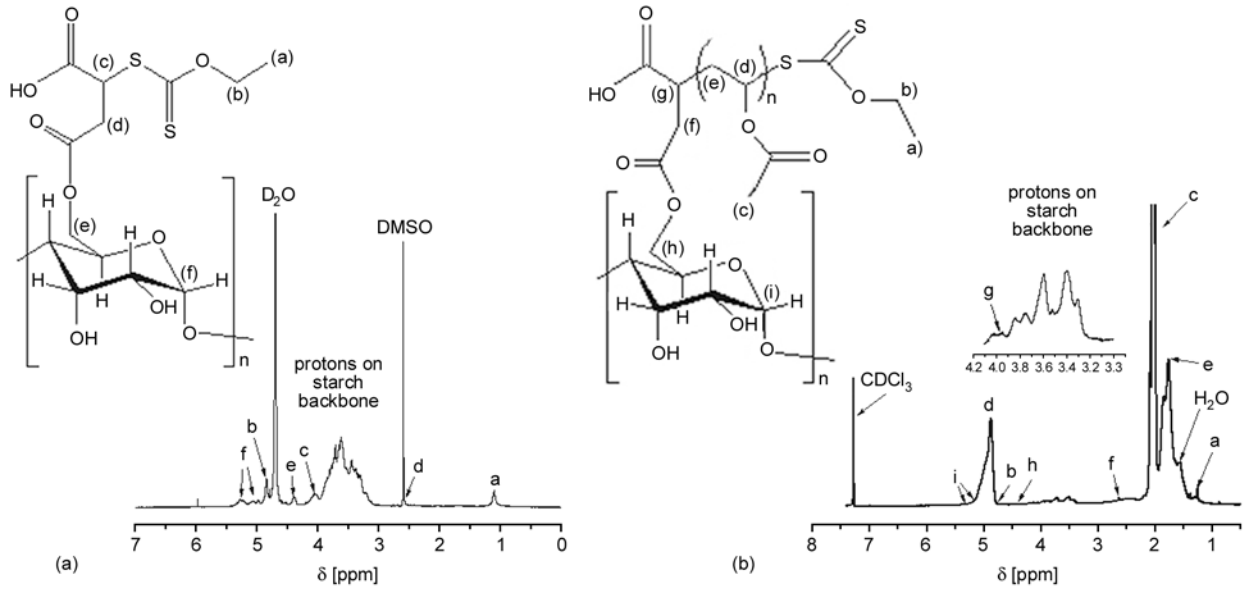

Figure 3. ^{1}H NMR spectra of Starch-based xanthate agent (a) and SVAc (b)

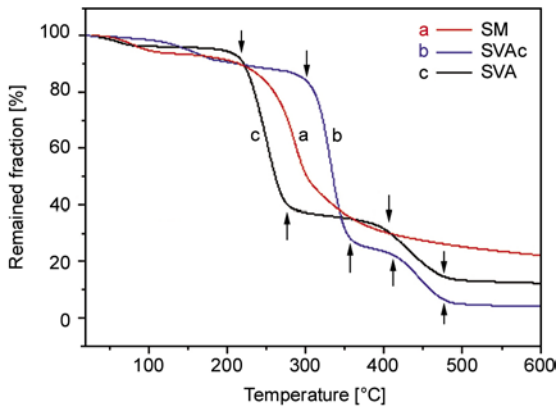

Figure 4. Thermogravimetric analysis profiles of SM (a), SVAc (b, M_n =8.6·10^4) and its derivative SVA (c)

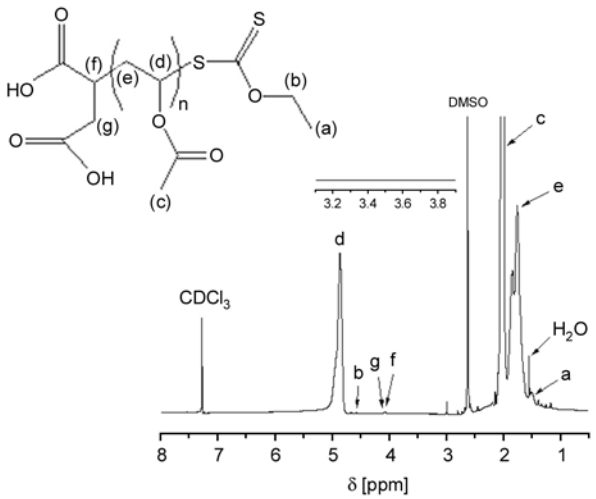

Figure 5. ^{1}H NMR spectrum of the hydrolysis remainder of SVAc

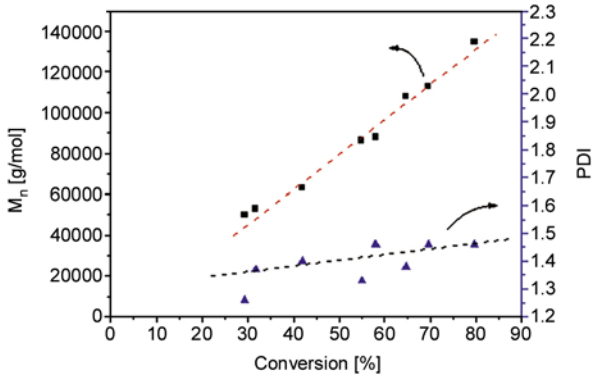

Figure 6. Number-average molecular weight (M_n) and the polydispersity index (PDI) as the functions of monomer conversion for vinyl acetate RAFT polymerization mediated via starch-based xanthate agent, conditions: 2.44·10^{-4} mol/l AIBN, 4.33·10^{-2} mol/l VAc, 0.1 g starch-based xanthate agent, 6ml DMSO, 60°C

To verify starch component of SVAc is removed thoroughly, the structure of acidolysis residue is

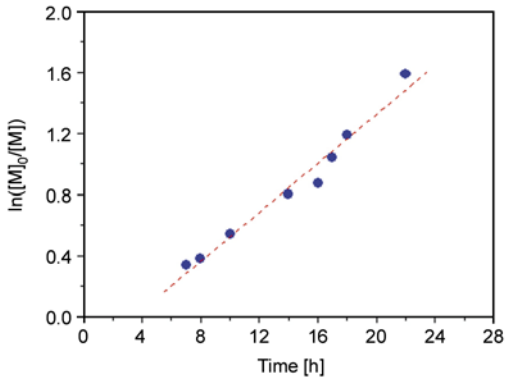

Figure 7. Kinetic curve of RAFT polymerization of vinyl acetate mediated via starch-based xanthate agent (2.44·10^{-4} mol/l AIBN, 4.33·10^{-2} mol/l VAc, 0.1 g starch-based xanthate agent, 6 ml DMSO, at 60°C)

characterized with the ^{1}H NMR spectra (Figure 5). The signals at 3.2–3.7 ppm have disappeared, which suggests starch is removed completely and the structure of PVAc is kept during the acidolysis. GPC analysis results of the hydrolysis products reveal the dependence of the number-average molecular weight (M_n) and PDI on monomer conversions (Figure 6). Mn values increase almost linearly with monomer conversions. PDI ranges from 1.26 to 1.46, which is rather low. The rate plot, ln([M]$_0$/[M]) versus time, is almost linear (Figure 7), which indicates the propagating radical concentration is invariant during the polymerization. These results are consistent with the characteristics of LCP [25–26]. In other words, the reaction has implemented as designed.

3.2. Tunable micellization of SVAc and gelation of SVA

SVAc is composed of hydrophilic starch and hydrophobic PVAc segments, which indicates that SVAc may be amphiphilic. To evaluate the hydrophilic character of SVAc, the films of starch, PVAc and SVAc are prepared by spin coating. The surface of the films is smooth, as observed with scanning electron microscope (data not shown), which suggests the effect of the surface roughness on the contact angle value can be neglected. Thus, the contact angle values of the samples only rely on their structure. The static contact angle values of water on the starch, PVAc and SVAc indicate that the hydrophobicity of SVAc is intervenient between starch and PVAc (Figure 8). Furthermore, the hydrophobicity of the

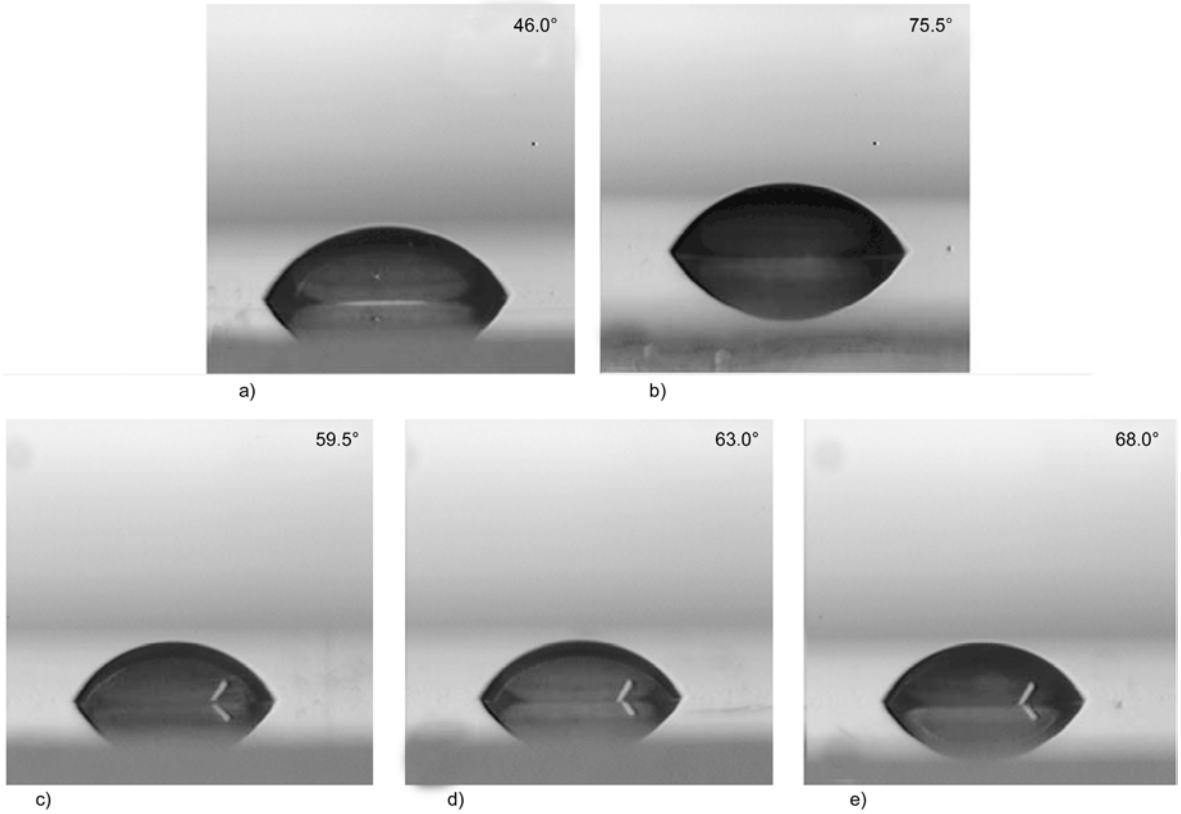

Figure 8. Contact angle of water on (a) starch, (b) PVAc ($M_n = 1.7 \cdot 10^5$), (c) SVAc-I ($M_n = 5.3 \cdot 10^4$, (d) SVAc-II ($M_n = 8.6 \cdot 10^4$) and (e) SVAc-III ($M_n = 1.3 \cdot 10^5$)

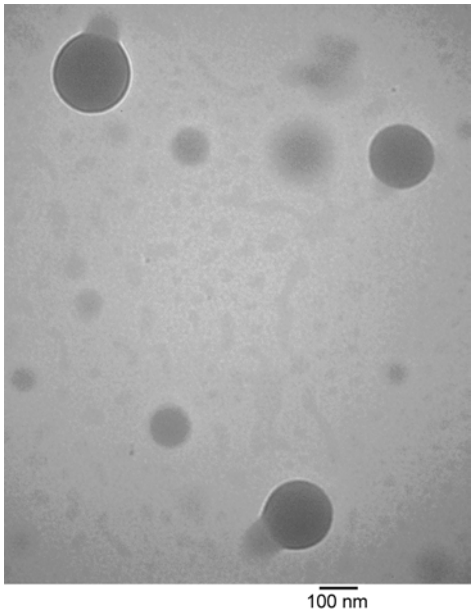

Figure 9. TEM image of SVAc micelle (the solution concentration is $4 \cdot 10^{-4}$ g/ml), and the size distributions of SVAc micelles assembled in aqueous solution: (1) SVAc-I, (2) SVAc-II, (3) SVAc-III

SVAc increases with the chain length of hydrophobic PVAc segment. It can be inferred that the difference in solubility of two segments in water may result in forming core-corona type micelles [27]. As shown in Figure 9, the morphology of SVAc micelles is regular sphere and disperses well without aggregation. The diameter of the micelles is around 100~200 nm. In addition, DLS measurement results narrate that the size of the micelles in aqueous solution increases with the chain length of PVAc segment (Table 1). Evidently, the hydrophobicity and self-assembly behavior of SVAc depend on molecular weight and are controllable.

Table 1. Hydrophobicity and micellar mean size of SVAc with different molecular weight and its distribution

Sample	M_n[a,b] [g/mol]	PDI[b]	Contact angle [°]	Mean diameter [nm]
SVAc-I	53 033	1.37	59.5	137.5
SVAc-II	86 383	1.33	63.0	153.0
SVAc-III	134 659	1.46	68.0	186.1

[a]M_n is the molecular weight of PVAc, the hydrolysis product of SVAc

[b]M_n and PDI are determined with GPC

It is anticipated that the incorporation of PVA segment will improve the properties of starch evidently. SVAc can be readily converted into SVA by the classical saponification reaction [28]. Herein, what we concerned is the capacity of SVA forming hydrogel in mild physical way, as this property is

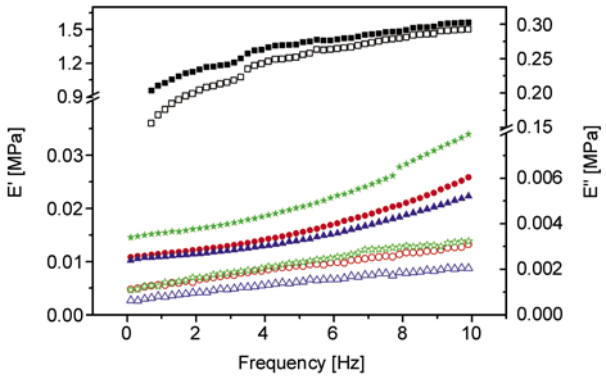

Figure 10. Effect of chain length on the storage modulus and loss modulus of starch and SVA. Storage modulus (E', full symbols), loss modulus (E'', open symbols); starch (■ and □); SVA-I (▲ and Δ); SVA-II (● and ○), and SVA-III (★ and ☆)

quite useful for medical applications such as drug delivery and tissue engineering [29]. To compare the relevant information, DMTA measurements of starch and SVA gels with controlled chain length are implemented. Unlike SVA, starch is difficult to form physically cross-linked hydrogel via freezing/thawing cycles [6]. Noting a starch gel obtained from 16~33% aqueous solution and three freezing/thawing cycles will disaggregate into powder after being kept in the water for twelve hours, the starch gel used for DMTA test in this article is prepared by subjecting a 50% aqueous solution of starch to three freezing/thawing cycles. Figure 10 shows the storage modulus (E') and loss modulus (E'') of starch gel and SVA hydrogels. E' and E'' of starch gel increase with the frequency and level off at last. E' of starch gel is about five times higher than its E''. DMTA analysis results of SVA hydrogels reflect that their mechanical properties are sensitive to the PVA network structure [30]. In the range of 0.1~10 Hz, the relationships between E' (or E'') and frequency of SVA hydrogels are linear. E' of SVA hydrogels are ten times greater than their E'' in value. Moreover, E' and E'' of SVA hydrogels increase as the chain length of PVA segments increases. The crystallinity of the dried SVA hydrogels calculated from the XRD profiles [31] are 29.4, 33.6 and 37.1% for SVA-1, SVA-3 and SVA-5 respectively. This indicates the relationship between the physical crosslink degree of SVA hydrogel and the molecular weight of PVA segment is in direct ratio and interprets the effect of M_n on E' well. These results demonstrate the formation of SVA hydrogels [32]. Noting the concentration of SVA aqueous solution for forming hydrogel is just 10%, it is evident that the incorporation of PVA segment greatly enhance the capability of starch to form physical 3D network structure. Moreover, such ability can be tuned with the molecular weight of PVA.

4. Conclusions

Developing starch-based polymers may offer an effective route to enhance the added-value of natural biopolymers and provide an answer for environmental issue. Integration of starch with synthetic PVA is one of the possible ways to this target. Tailoring the chain length of PVA may offer an approach to modulate the properties of starch-PVA biohybrid. In view of these, the conjugate of starch and well-defined PVAc, is developed by conducting starch-based xanthate agent mediated-RAFT polymerization of vinyl acetate. Another starch-based conjugate, SVA, is obtained from its precursor SVAc subsequently. Two conjugates show some interesting properties: SVAc self-assembling into spheral micelles and SVA forming physically cross-linked hydrogel. Moreover, the characteristics of SVAc and SVA are linear-dependence on the molecular weight of PVAc or PVA segments, and the chain lengths of PVAc or PVA segments are controllable. As starch and PVA are biocompatible, SVA may be a potential candidate for biomedical applications. The presented method may also provide an available way for tailor-making starch-based functional materials.

Acknowledgements

This work was supported by the Natural Science Foundation of Fujian Province of China (No. 2010J01291 or E1010026). The authors were grateful to Mr. S. Liu, H. Z. Zhang and C. H. Yuan for their help to do DLS, NMR and GPC measurements.

References

[1] Gandini A.: Polymers from renewable resources: A challenge for the future of macromolecular materials. Macromolecules, **41**, 9491–9504 (2008). DOI: 10.1021/ma801735u

[2] Lu D. R., Xiao C. M., Xu S. J.: Starch-based completely biodegradable polymer materials. Express Polymer Letters, **3**, 366–375 (2009). DOI: 10.3144/expresspolymlett.2009.46

[3] Chiellini E., Corti A., D'Antone S., Solaro R.: Biodegradation of poly (vinyl alcohol) based materials. Progress in Polymer Science, **28**, 963–1014 (2003). DOI: 10.1016/S0079-6700(02)00149-1

[4] Ricciardi R., D'Errico G., Auriemma F., Ducouret G., Tedeschi A. M., De Rosa C., Lauprêtre F., Lafuma F.: Short time dynamics of solvent molecules and supramolecular organization of poly (vinyl alcohol) hydrogels obtained by freeze/thaw techniques. Macromolecules, **38**, 6629–6639 (2005). DOI: 10.1021/ma0506031

[5] Spiridon I., Popescu M. C., Bodârălu R., Vasile C.: Enzymatic degradation of some nanocomposites of poly(vinyl alcohol) with starch. Polymer Degradation and Stability, **93**, 1884–1890 (2008). DOI: 10.1016/j.polymdegradstab.2008.07.017

[6] Xiao C. M., Yang M. L.: Controlled preparation of physical cross-linked starch-g-PVA hydrogel. Carbohydrate Polymers, **64**, 37–40 (2006). DOI: 10.1016/j.carbpol.2005.10.020

[7] Sumerlin B. S., Vogt A. P.: Macromolecular engineering through click chemistry and other efficient transformations. Macromolecules, **43**, 1–13 (2010). DOI: 10.1021/ma901447e

[8] Xu J. T., Tao L., Boyer C., Lowe A. B., Davis T. P.: Combining thio−bromo 'click' chemistry and RAFT polymerization: A powerful tool for preparing functionalized multiblock and hyperbranched polymers. Macromolecules, **43**, 20–24 (2010). DOI: 10.1021/ma902154h

[9] Boyer C., Bulmus V., Davis T. P., Ladmiral V., Liu J. Q., Perrier S.: Bioapplications of RAFT polymerization. Chemical Reviews, **109**, 5402–5436 (2009). DOI: 10.1021/cr9001403

[10] Angelova N., Hunkeler D.: Rationalizing the design of polymeric biomaterials. Trends in Biotechnology, **17**, 409–421 (1999). DOI: 10.1016/S0167-7799(99)01356-6

[11] Bernard J., Favier A., Zhang L., Nilasaroya A., Davis T. P., Barner-Kowollik C., Stenzel M. H.: Poly(vinyl ester) star polymers via xanthate-mediated living radical polymerization: From poly(vinyl alcohol) to glycopolymer stars. Macromolecules, **38**, 5475–5484 (2005). DOI: 10.1021/ma050050u

[12] Fleet R., McLeary J. B., Grumel V., Weber W. G., Matahwa H., Sanderson R. D.: RAFT mediated polysaccharide copolymers. European Polymer Journal, **44**, 2899–2911 (2008). DOI: 10.1016/j.eurpolymj.2008.06.042

[13] Tizzotti M., Charlot A., Fleury E., Stenzel M., Bernard J.: Modification of polysaccharides through controlled/living radical polymerization grafting – Towards the generation of high performance hybrids. Macromolecular Rapid Communications, **31**, 1751–1772 (2010). DOI: 10.1002/marc.201000072

[14] Xiao C. M., Ye J.: Preparation of the carboxylic derivates of starch with maleic anhydride (in Chinese). Chinese Journal of Applied Chemistry, **22**, 643–646 (2005).

[15] Fleet R., McLeary J. B., Grumel V., Weber W. G., Matahwa H., Sanderson R. D.: Preparation of new multiarmed RAFT agents for the mediation of vinyl acetate polymerization. Macromolecular Symposium, **255**, 8–19 (2007). DOI: 10.1002/masy.200750902

[16] Li Y. G., Zhang Y. Q., Yang D., Feng C., Zhai S. J., Hu J. H., Lu G. L., Huang X. Y.: Well-defined amphiphilic graft copolymer consisting of hydrophilic poly(acrylic acid) backbone and hydrophobic poly(vinyl acetate) side chains. Journal Polymer Science Part A: Polymer Chemistry, **47**, 6032–6043 (2009). DOI: 10.1002/pola.23646

[17] Pan Y. S., Xiong D. S., Gao F.: Viscoelastic behavior of nano-hydroxyapatite reinforced poly(vinyl alcohol) gel biocomposites as an articular cartilage. Journal of Materials Science: Materials in Medicine, **19**, 1963–1969 (2008). DOI: 10.1007/s10856-007-3280-6

[18] Shi R., Zhu A., Chen D. F., Jiang X. J., Xu X. C., Zhang L. Q., Tian W.: In vitro degradation of starch/PVA Films and biocompatibility evaluation. Journal of Applied Polymer Science, **115**, 346–357 (2010). DOI: 10.1002/app.31136

[19] Samaha S. H., Nasr H. E., Hebeish A.: Synthesis and characterization of starch-poly(vinyl acetate) graft copolymers and their saponified form. Journal of Polymer Research, **12**, 343–353 (2005). DOI: 10.1007/s10965-004-7937-2

[20] Barner-Kowollik C., Perrier S.: The future of reversible addition fragmentation chain transfer polymerization. Journal of Polymer Science Part A: Polymer Chemistry, **46**, 5715–5723 (2008). DOI: 10.1002/pola.22866

[21] Coote M. L., Radom L.: Substituent effects in xanthate-mediated polymerization of vinyl acetate: Ab initio evidence for an alternative fragmentation pathway. Macromolecules, **37**, 590–596 (2004). DOI: 10.1021/ma035477k

[22] Barsbay M., Güven O., Stenzel M. H., Davis T. P., Barner-Kowollik C., Barner L.: Verification of controlled grafting of styrene from cellulose via radiation-induced RAFT polymerization. Macromolecules, **40**, 7140–7147 (2007). DOI: 10.1021/ma070825u

[23] Roy D., Knapp J. S., Guthrie J. T., Perrier S.: Antibacterial cellulose fiber via RAFT surface graft polymerization. Biomacromolecules, **9,** 91–99 (2008). DOI: 10.1021/bm700849j

[24] Rimez B., Rahier H., Van Assche G., Artoos T., Biesemans M., Van Mele B.: The thermal degradation of poly(vinyl acetate) and poly(ethylene-co-vinyl acetate), Part I: Experimental study of the degradation mechanism. Polymer Degradation and Stability, **93**, 800–810 (2008).
DOI: 10.1016/j.polymdegradstab.2008.01.010

[25] Perrier S., Davis T. P., Carmichael A. J., Haddleton D. M.: First report of reversible addition–fragmentation chain transfer (RAFT) polymerisation in room temperature ionic liquids. Chemical Communications, **19**, 2226–2227 (2002).
DOI: 10.1039/b206534g

[26] Köllisch H. S., Barner-Kowollik C., Ritter H.: Amphiphilic block copolymers based on cyclodextrin-host–guest complexes via RAFT-polymerization in aqueous solution. Chemical Communications, **9**, 1097–1099 (2009).
DOI: 10.139/b818897a

[27] Podríguez-Hernández J., Chécot F., Gnanou Y., Lecommandoux S.: Toward 'smart' nano-objects by self-assembly of block copolymers in solution. Progress in Polymer Science, **30**, 691–724 (2005).
DOI: 10.1016/j.progpolymsci.2005.04.002

[28] Fanta G. F., Burr R. C., Doane W. M., Russell C. R.: Graft polymerization of vinyl acetate onto starch. Saponification to starch–g–poly(vinyl alcohol). Journal of Applied Polymer Science, **23**, 229–240 (1979).
DOI: 10.1002/app.1979.070230121

[29] Hoffman A. S.: Hydrogels for biomedical applications. Advanced Drug Delivery Reviews, **43**, 3–12 (2002).
DOI: 10.1016/S0169-409X(01)00239-3

[30] Cascone M. G.: Dynamic-mechanical properties of bioartificial polymeric materials. Polymer International, **43**, 55–69 (1997).
DOI: 10.1002/(SICI)1097-0126(199705)43:1<55::AID-PI762>3.0.CO;2-#

[31] Xiao C. M., Geng N. N.: Tailored preparation of dual phase concomitant methylcellulose/poly(vinyl alcohol) physical hydrogel with tunable thermosensivity. European Polymer Journal, **45**, 1086–1091 (2009).
DOI: 10.1016/j.eurpolymj.2009.01.011

[32] Reinicke S., Schmelz J., Lapp A., Karg M., Hellweg T., Schmalz H.: Smart hydrogels based on double responsive triblock terpolymer. Soft Matter, **5**, 2648–2657 (2009).
DOI: 10.139/b900539k

eXPRESS Polymer Letters Vol.5, No.6 (2011) 545–554
Available online at www.expresspolymlett.com
DOI: 10.3144/expresspolymlett.2011.53

Rapid biomimetic mineralization of chitosan scaffolds with a precursor sacrificed method in ethanol/water mixed solution

L. H. Li[1,2], *M. Y. Zhao*[1,2], *S. Ding*[1,2], *C. R. Zhou*[1,2*]

[1]Department of Materials Science and Engineering, Jinan University, Guangzhou, 510630, China
[2]Engineering Research Center of Artificial Organs and Materials, Ministry of Education, Guangzhou, 510630, China

Received 2 November 2010; accepted in revised form 30 December 2010

Abstract. Biomimetic mineralization was performed on a large scale by a rapid and efficient approach. Chitosan scaffolds were placed in a mixed solution of urea, ethanol and distilled water, followed by the introduction of dibasic sodium phosphate (0.1M) and calcium chloride (0.1M) with the molar ratio of 1.67. These mixed solvents was then adjusted to weakly alkaline by adding sodium hydroxide solution. Finally the reaction mixture was sealed and kept at 80ºC for predetermined time. The composition and morphology of the apatite and the hybrid scaffolds were investigated by X-ray diffraction (XRD), transmission electron microscopy (TEM), Fourier Transform Infrared spectroscopy (FTIR) and environmental scanning electron microscopy (ESEM). The mechanism of nucleation and growth of crystals was discussed as well. The results revealed that chitosan scaffolds improved the crystallinity of hydroxyapatite (HAP) crystals. With the extension of mineralization time, the mineral layers on the outer surface and inner section of chitosan scaffolds increased as well. Furthermore, the compressive strength and modulus of the HAP-chitosan scaffolds biocomposites increased to 0.55±0.003 and 29.29±1.25 MPa respectively. Such one-pot approach may be extended to the mineralization of other materials and will have a broad application in the future.

Keywords: *biocomposites, mineralization, chitosan, hydroxyapatite*

1. Introduction

Bone is considered as a nanocomposite of minerals and proteins. Recently nano-sized hydroxyapatite (HAP) and its composites with polymers have been investigated with fascination and demonstrated a good impact on cell–biomaterial interaction [1, 2]. However, the migration of the nano HAP particles from the implanted site into surrounding tissues might cause damage to healthy tissues. Current advances in molecular biomimetics suggest that a biomineral-inspired approach may be of value in new classes of biomaterials [3, 4]. This approach is based primarily on the idea of macromolecules as templates to control inorganic crystal formation, and seeks to reproduce the nanoscopic and hierarchical structures of natural bone through biological principles and the processes of self-assembly or self-organization [5]. Biomimetic mineralization is a powerful approach for the synthesis of advanced scaffold materials with complex shapes, hierarchical organization and controlled size, shape and polymorphism under ambient conditions in aqueous environments.

Chitosan is partially deacetylated chitin, which is found in nature as a major organic component in several biocomposites, and has a crucial role in the hierarchical control of the biomineralization process. Furthermore, chitosan is one of the most important candidates for bone tissue engineering scaffolds, and possesses better mechanical properties than other natural polymers [6, 7]. Therefore, in this study polysaccharide chitosan scaffolds were selected as

*Corresponding author, e-mail: tcrz9@jnu.edu.cn

the porous matrix for mineralization, which control the nucleation, deposition and growth of the nanometer scaled HAP. It will be always very difficult to mimic exactly the calcification process that occurs in bone. This is further complicated by the fact that all mineralization processes are ultimately controlled by the cells directly associated to the tissue formation [8]. In literatures, nanometer scaled HAP powders and coatings can be synthesized using a number of strategies including sol-gel processing [9], co-precipitation [10, 11], emulsion techniques [12], batch hydrothermal processes [13–17], mechano-chemical methods [18] and chemical vapor deposition [19]. However, bio-compatible and environment-friendly pathway to synthesize biocomposites of HAP-biomolecule is also being explored. In this study, authors tried to prepare nanoscopic composite materials with a fast, facile and efficient way in large quantities. An ethanol-water solvent was used to control the formation, morphology and phase transition of HAP under 80ºC. Urea was utilized as a buffer reagent to balance pH value of the system, which decomposes into carbonate ion and ammonia in aqueous solution.

Such one-pot approach was easily manipulated and repeated. Furthermore, large quantity of nano HAP and mineralized scaffolds could be obtained spontaneously. The main aim of our study is not only to emulate a particular biological architecture or system, but to abstract the guiding principles and use such ideas for a broad application. Therefore, this rapid synthesis approach could also be extended to design other mineralized materials and devices.

2. Experimental section

2.1. Materials

Chitosan (MW 150,000, viscosity 200 mPas, 85% deacetylation) was obtained from Fluka Biochemical Ltd (Sigma-Aldrich Chemie GmbH, Buchs, Switzerland) and was purified before use. Hydroxyapatite (HAP, thermal spraying powder) were purchased from Plasma Biotal Limited (Buxton, UK), used as a control. Other chemicals in this study were: acetic acid, ethanol and calcium chloride from Merck GmbH (Darmstadt, Germany); sodium hydroxide from Fluka Biochemical Ltd; urea from Sigma/Aldrich Inc (Sigma-Aldrich Chemie GmbH, Buchs, Switzerland). All the chemicals were analytical reagent grade.

2.2. Preparation of chitosan scaffolds

Chitosan flakes were dissolved in 1 wt% acetic acid solution at room temperature to obtain 1.5 wt% homogeneous solution. The solution was filtered to remove air bubbles trapped in the viscous solution. Afterwards chitosan solution was cast into a polystyrene Petri dish and frozen at –80ºC for 2 h, and then freeze-dried overnight. The chitosan scaffolds (named as CS scaffolds) were washed with sodium hydroxyl/ethanol solution and 85 wt% ethanol to remove acetic acid, and then underwent a second freeze-drying.

2.3. Mineralization of CS scaffolds

CS scaffolds were placed in a wide-mouth bottle containing 0.3 g urea and 20 ml mixed solvents of ethanol and distilled water (3:1, v/v). Afterwards, a certain amount of dibasic sodium phosphate (0.1M) and calcium chloride (0.1M) with the molar ratio of 1.67 were introduced under magnetic stirring. This mixture was adjusted to become weakly alkaline by adding sodium hydroxide solution. Finally, the bottle was closed tightly and kept in the oven at 80ºC for 24 and 48 hours respectively. (The scaffolds were named as BCS-24h and BCS-48h respectively). After mineralization process, the scaffolds were washed with 85% ethanol thoroughly and were freeze-dried. The precipitation in suspension was centrifuged and washed with distilled water and dried at 60ºC for further study (named as apatite-24 h and apatite-48 h respectively).

2.4. Characterization of the scaffolds

The crystal structure of BCS scaffolds and the apatite formed in suspension were determined with a powder X-ray diffractometer (D8 X-ray diffractometer) employing the Cu–K_α line. Data were collected from 10 to 60° (2θ values), with a step size of 0.02°, and a counting time of 1 s per step. The composition of the BCS scaffolds was measured by a Fourier Transform Infrared spectrometer (FT-IR, FTS 6000 Spectrometer, Bio-RAD). Transmission electron microscopy (TEM) was used to evaluate the crystals formed in the solution and on the chitosan matrix which were achieved by ultrasonic dispersion. An environmental scanning electron microscope (ESEM, Quanta 600 FEG, FE-ESEM, FEI Europe) was employed to detect the surface topography and microstructure of the scaffolds. To ana-

lyze the mechanical property improvement of these scaffolds, the compression test was performed at room temperature using a Zwick universal testing machine (Zwick Z010, Zwick GmbH, Germany, software Testexpert V10.11). Three cubic scaffolds (dry state) were tested for each sample. Tests were conducted with a constant strain rate of 2 mm·min^{-1}, either up to failure or until 70% reduction in specimen height. The compressive modulus (E) was determined by linear regression from the slopes in the initial elastic portion of the stress-strain diagram.

3. Results and discussion

3. 1. Determination of crystalline component with XRD

Figure 1 shows the XRD patterns of the BCS scaffolds and the apatite in the suspension. The Bragg peaks observed approximately at 26, 28, 29, 30–35, 39, 46, 49, and 50º (2θ) correspond to the pure phase HAP [20], as the bar graph shows in the bottom of Figure 1. Figure 1a demonstrates that the apatite formed in the suspension was HAP but with poor crystallinity. However apatite on BCS-24h presents the characteristic peaks of HAP and dicalcium phosphate phase (DCP, marked as solid dots in Figure 1b). The non-uniformity of reaction microenvironments in bulk solution and around chitosan scaffolds surface may be responsible for this difference. Generally, the DCP is not stable in alkaline solution at chemistry laboratory [21]. HAP phase always coexisted with other calcium phosphates even in natural bone, such as DCP, TCP (tricalcium phosphate), OCP (octacalcium phosphate), amorphous phases, etc [22, 23]. After 48 h, the XRD peaks of DCP phase disappears in the chitosan composites and all sharp peaks can be indexed as pure phase of HAP with high crystallinity (Figure 1d). And the XRD pattern of apatite-48 h (Figure 1c) has no typical differences from that of apatite-24 h, wherein the broad peaks may be attributed to the small particle size and crystal lattice strains.

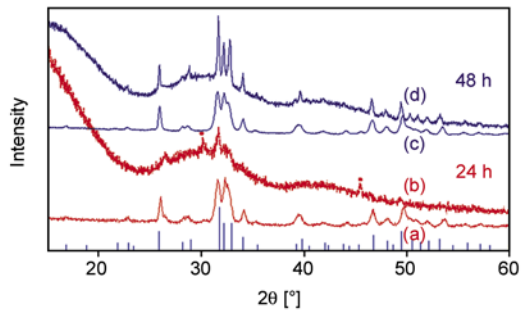

Figure 1. XRD patterns of samples: (a) apatite-24 h; (b) BCS-24h; (c) apatite-48 h and (d) BCS-48h. The bar graph at the bottom is indexed HAP peaks according to JCPDS 9-432. The solid dot marked in (b) is DCP (JCPDS 9-80).

3.2. Determination of phase composition with FT-IR

The spectra of native chitosan (see Figure 2a) exhibited the characteristic bands at 1648 cm^{-1} (amide I), 1590 cm^{-1} (amide II) and 1375 cm^{-1} (amide III). Wave number 1026 cm^{-1} was the primary amino groups (–NH_2) at C_2 position of glucosamine. Stretching of primary alcoholic groups (–CH_2OH) was at 1056 cm^{-1}. The FT-IR spectra of mineralized CS scaffolds (Figure2b and c) showed a strong band at near 1020 cm^{-1} which means that the absorption of –NH_2 and PO_4^{3-} were aligned. Furthermore it could be detected that the three characteristic signals of HAP (1089, 1018 and 961 cm^{-1}) were more intensive in BCS-48h than in BCS-24h. Figure 2d is the spectra of commercial HAP, where the three peaks were assigned as stretching vibrations of PO_4^{3-} ions.

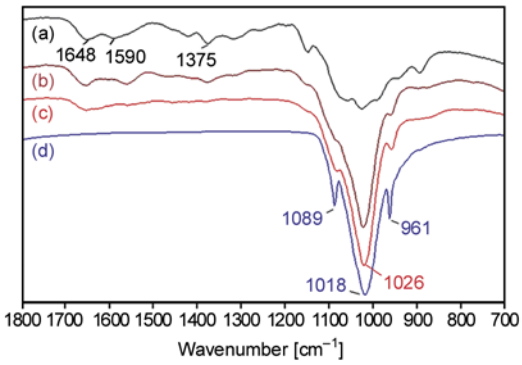

Figure 2. FT-IR spectra of samples: (a) native CS, (b) BCS-24h sponge, (c) BCS-48h sponge and (d) commercial HAP powder, Plasma Biotal Limited, UK

3.3. Morphology of the scaffolds

Figure 3a) is the image of white and soft CS scaffold, which possessed thin, smooth and porous walls. ESEM image of apatite-48 (Figure 3b) showed that the nanorods are uniform and the diameter is about 100 nm. However the apatite deposited on the chitosan scaffolds was different from that suspended in solution. From the previous reports, HAP tends to form one dimensional nanowires or sea-urchin aggre-

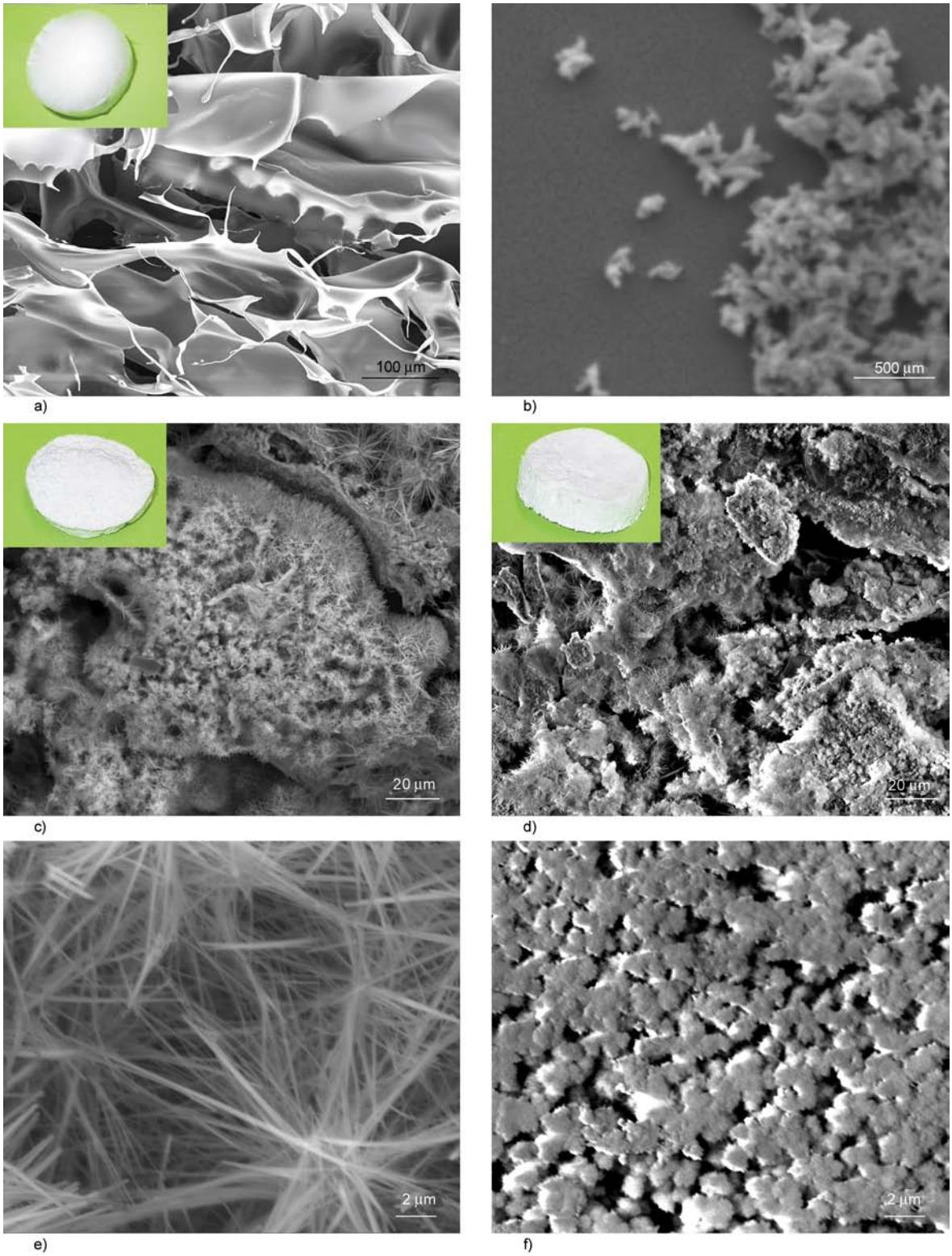

Figure 3. ESEM images of original CS sponge (a), apatite-48 h (b), BCS-24h (c), BCS-48h (d), higher magnification images of the large apatite aggregates (e) and small aggregates (f)

gates consisting of nanorods or nanowires in aqueous solution [24–26]. Here, the interesting point is the different morphologies of HAP formed in solution and on chitosan scaffolds walls. Figure 3c presents one ESEM image of the apatite deposited on the scaffolds for 24 hours (BCS-24h), which shows loose mineral layer of sea-urchin structure with different sizes. From flat areas to the pores of the

matrix, the apatite aggregates become bigger. In the pores of the scaffolds, the aggregates are more than ten times larger than that on the other areas. The HAP mineral layer becomes thicker and tighter on the BCS-48h scaffolds, as shown in Figure 3d. Similar to what happened on BCS-24h scaffolds, large amount of sea-urchin aggregates with bigger sizes in the pores, and the smaller size of the aggregates in flat areas are also visible. More details of HAP aggregates with larger size in the pores were present in Figure 3e. It demonstrates that the diameter of the sea-urchin HAP aggregates are more than 20 μm, which consist of uniform thin nanowires with a length of more than 10 μm and a diameter of less than 150 nm. And these sea-urchin like HAP structures aggregated together to form a network in the pores of the scaffolds. Small sea-urchin aggregates (diameter ca. 2 μm) made a thick deposit on the flat areas (BCS-48h, Figure 3f). Here, it is worth to note that the size of the aggregates in pores is ten times of that on the flat areas by checking most areas on the matrix during the ESEM measurement.

To check the mineralization inside the scaffolds, cryo-fractured cross sections were observed with ESEM as well. Both scaffolds (BCS-24h, 48h) showed plenty of apatite aggregation on the matrix walls (see Figure 4a and 4c). From Figure 4b, nano-sized apatite particles and some spheres adhere on the inside walls of BCS-24h. After 48 hours mineralization, HAP nanopaticles grew bigger and continuously to form a dense film covering on the BCS-48h scaffolds (Figure 4d). Moreover, the amount of micron size spheres increased and joined together. It is obvious that the HAP film became denser and thicker when the chitosan scaffolds were mineralized for 48 hours. Hence, the mineralization of HAP

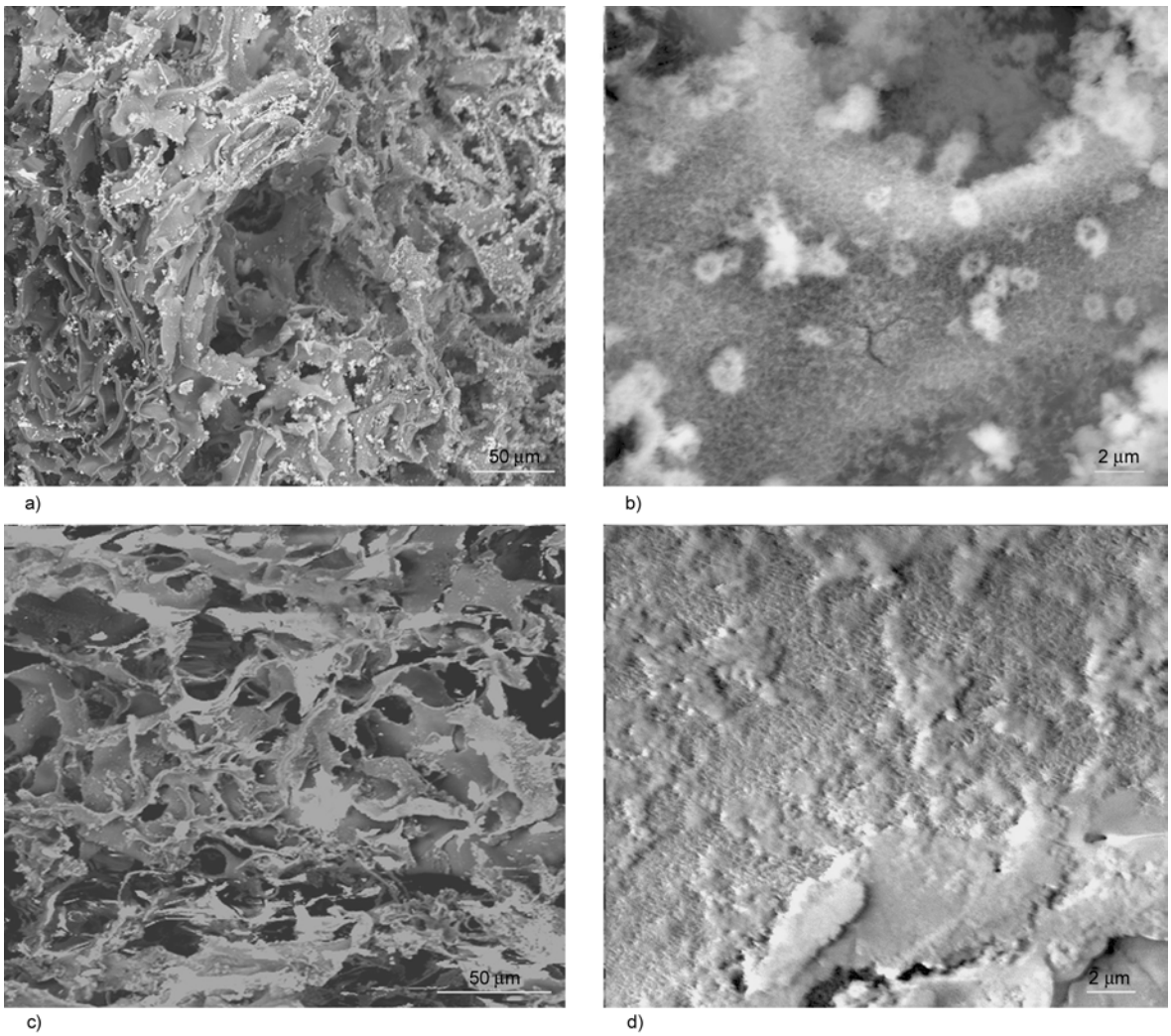

Figure 4. Cross section of the chitosan scaffolds with SEM observation. (a) and (b) BCS-24h scaffolds. (c) and (d) BCS-48 scaffolds with different magnification.

on the chitosan scaffolds is successful, which the dense mineral layer attached on the outside and inside surfaces of the scaffolds.

3.4. TEM micrographs

Transmission electron microscope (TEM) images of the apatite-48 h (Figure 5a) revealed well defined crystalline tapes of ca. 80×15 nm (aspect ratio ca. 5.5). The HAP nanorods are monodisperse and uniform in size, although there is some random aggregation of HAP nanorods. The HAP on BCS-48h scaffolds was collected with ultrasonic vibration. The TEM image demonstrates that the HAP crystals are much larger in size and aggregate into sea-urchin structure (Figure 5b). This observation is accordance with the SEM images.

3.5. Mechanical properties

In nature, bone strength depends on bone matrix volume, micro architecture, and also on the degree of mineralization. The more cancellous tissue is mineralized, the higher stiffness it is [27]. In this study we achieved similar results. The original chitosan sponges were very soft, with compressive strength of 0.09±0.012 MPa. After mineralization, the compression strength of CS scaffolds got a dramatic increase, rising to 0.54±0.005 and 0.55±0.003 MPa respectively. This increase in compression strength can be attributed to the mineralized mineral layer on the chitosan, and thicker mineral layer leads to the higher compression strength of the scaffolds (0.55 MPa, BCS-48h). Moreover, the compressive modulus of BCS-48h (29.29±1.25 MPa) is obviously higher than that of the BCS-24h (24.47±0.45 MPa), which reveals that thick nano HAP layer makes the scaffolds stiffer. Comparing with the data of human bone, the compressive strength of the composite scaffold is still far from that of cortical bone (Strength of 130–180 MPa, modulus of $12–18 \cdot 10^3$ MPa) and cancellous bone (Strength of 4–12 MPa, modulus of $0.1–0.5 \cdot 10^3$ MPa) [28–30], but closer to cartilage (Strength of 4–59 MPa and modulus of 1.9–14.4 MPa [31, 32] or initial soft callus which has modulus closer to 1 MPa. Therefore these materials can be suggested to be used as substitute for cartilage, non-load-bearing bone or initial fracture healing callus substitute, which can remodel and develop into bone tissue.

3.6. Mechanism of mineralization

One of the fundamental aspects controlling the final habit of a growing crystal is the balance between kinetic and thermodynamic control, which plays a key role in crystal growth, determines the final crystal habit, phase, shape, and structure [33, 34]. The precipitation of calcium phosphate from aqueous solution is somewhat complicated due to the possible occurrence of several different calcium phosphates with or without hydrogen/hydroxide group, depending on the solution composition and the pH value [35–37]. These phosphates salts include dicalcium phosphate (DCP), dicalcium phosphate dehydrate (DCPD), tricalcium phosphate

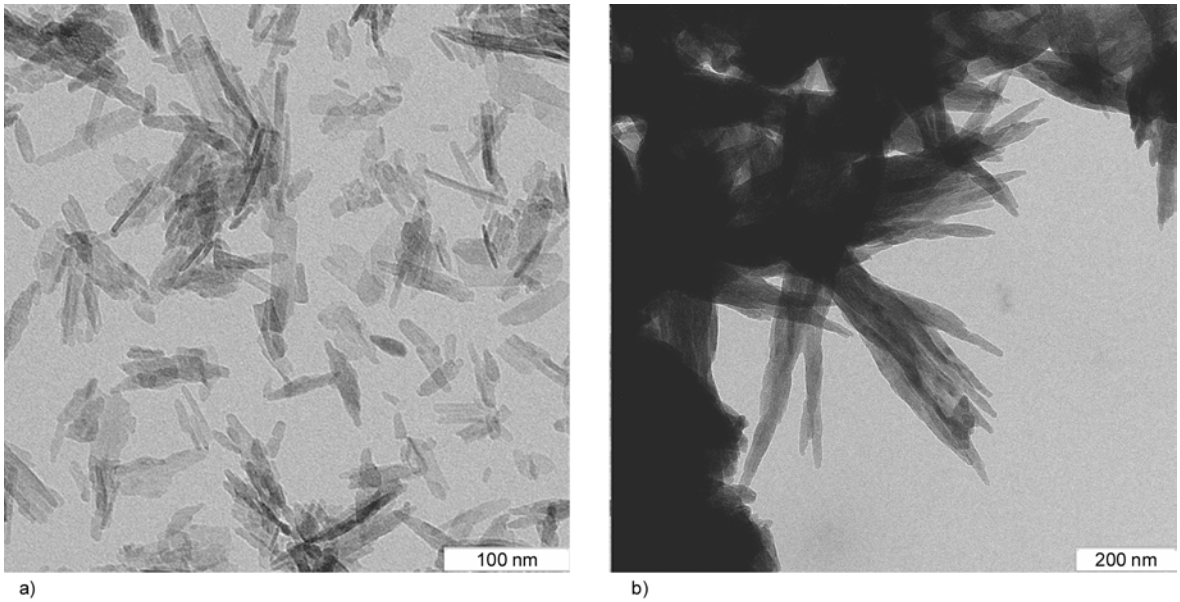

Figure 5. Transmission electron micrographs of hydroxyapatite: (a) apatite-48h and (b) apatite on the BCS-48h scaffolds

(TCP), octacalcium phosphate (OCP), HAP, amorphous calcium phosphate (ACP), and so on [38, 39]. However, HAP phase is more stable than other salts stated above in alkaline aqueous. Hence, some people report that these phosphate salts were used as precursor for preparation of HAP or were observed as transitory by-products in their experiments [21, 40]. In this work, DCP were characterized at the early stage of reaction, which can be regarded as transition phase or precursor. At 80°C, urea decomposed into CO_2 and NH_3, then dissolved in aqueous solution and hydrolyzed to HCO_3^- or CO_3^{2-} and NH_4^+ in solution. These ions kept the solution weakly alkaline for the slow hydrolysis of DCP and crystallization of HAP. The mechanics of the mineralization in this study was analyzed as following.

Crystallization in bulk solution and on chitosan surface

The spatially periodic functional groups $-NH_3^+$ on the surface of the CS substrate interacted with the phosphate anions when the dibasic sodium phosphate solution was introduced into the wide mouth bottle containing urea mixed solvents and CS. Here, it should be noted that one part of the phosphate anions would be stabilized by the $-NH_3^+$ group of CS and the other part of free phosphate anions would stay in bulk solution, as shown in the scheme (Figure 6a and 6b). Then DCP phase formed on CS surface or in bulk solution when the calcium chloride solution was introduced into the bottle by the reaction between the hydrogen phosphate and calcium (Figure 6c). However, the salt was not stable in alkaline solution and especially at 80°C. Then, the hydrolysis was carried on for the formation of the thermodynamic stable HAP phase (Figure 6d) [41]. During the hydrolysis of DCP phase for formation of HAP phase, the free cations and anions in bulk solution crystallized homogenously to form uniform HAP nanorods (Figure3b and 5a). Considering the strong binding between the phosphate ions and CS, it is reasonable to assume that hydrolysis of the DCP on the CS would slow down. With the comparison of XRD patterns of BCS-24h and apatite-24h (Figure 1a and b), it is found that DCP phase is still resident on the CS surface after even 24 hours reaction (Figure 1b), while all of powders suspended in bulk solution were characterized as pure phase of HAP (Figure 1a). In one previous paper for elucidate the residue of DCP phase, the author found that the formation of HAP and the hydrolysis of DCP were competitive [41]. But, in this work, this viewpoint can not be interpreted completely why DCP phase was only resident on the CS surface and no DCP phase mixed in powders outside of the scaffolds. Hence, this phenomenon proved laterally that the DCP crystallized at the interface of phosphate-chitosan, and the interface can stabilize the meta-stable DCP phase for a long time. Moreover, the stabilization of DCP precursor

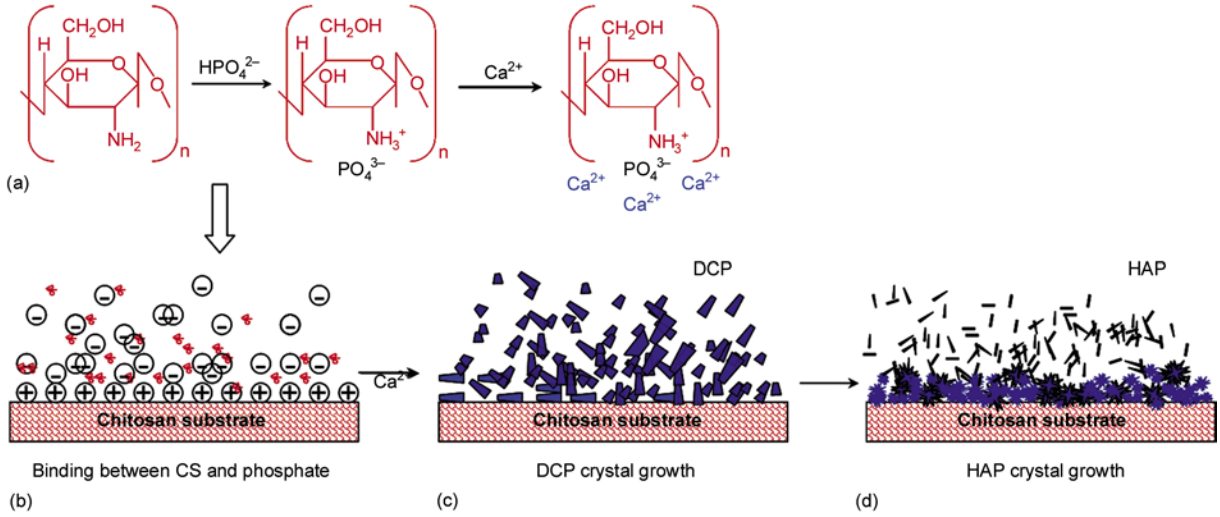

Figure 6. Schematic illustration of the major steps involved in the mineralization on chitosan matrix. (a) a scheme of chitosan molecule role in the mineralization of CS matrix, and scheme of chitosan sponge substrate mineralization: (b) Strong interaction between CS and phosphate, which facilitates the nucleation of crystals. (c) Colloidal cloud of amorphous calcium phosphate forms after addition of Ca^{2+} ions (formation of DCP phase after addition of Ca^{2+} ions) and (d) HAP crystals grow on the substrate.

changed kinetic factors of crystallization of HAP to some extent, leading to the different morphology on the CS surface.

Mechanism of chitosan-HAP bio-composite film

The strong binding of phosphate anions with the positive charge on the chitosan (a linear polysaccharide) will induce a high supersaturation degree near to the chitosan. And this binding was functioned for nucleating DCP firstly (Figure 6c) and then HAP secondly (Figure 6d) by hydrolysis of DCP. As stated above, the $-NH_3^+$ group is periodically arranged in the CS. The nucleuses of HAP were bound by the $-NH_3^+$ group protruding on the CS and covered the scaffolds surface in the process of DCP hydrolysis. The covering of HAP nucleuses on the scaffolds should be responsible for the formation of HAP film and the HAP-biocomposites. Moreover, it was reported that CS bound preferentially to the (100) face of the HAP crystal [42]. So, the HAP nuclei then grew out of CS surface along the c-axis by the Oswald-ripening mechanism [43]. With the time extension, HAP nano crystals grew bigger, and the mineral film become denser and thicker by the hydrolysis of DCP residue, which can be observed from Figure 3c–d.

The similar process also happened in the inside surface of CS. Crystals on the cross section of CS (Figure 4b, 4d) were much smaller than that on the outer surface (Figure3c–f), because the outer surface was surrounded by bulk reaction solution and inside surface of scaffolds not. For the inside surface of CS, the nuclei of HAP were also bound by the positive charge, and then grew bigger by hydrolysis of DCP. But the concentration of cations and anions inside of CS were lower than that in bulk solution, so the HAP crystal was smaller. But, the mineral layer became thicker and denser when the reaction time elongated to 2 days (Figure 4). In a word, the HAP layer covered both outside and inside the surface of CS. It is found that the chitosan improved the crystalline quality of HAP phase which grew on CS (Figure 1c–d), although the exact reason is not clear now.

Mechanical properties of the biocomposites

The mineral layer deposited on the CS scaffolds greatly improved the mechanical properties. In biomineralized tissues such as bone, the recurring structural motif at the supramolecular level is an anisotropic stiff inorganic component reinforcing the soft organic matrix. There would be two aspects to improve the mechanical properties of the composite. The stiff nano HAP crystals covered on the surface of CS film and filled in the micropores of the CS scaffolds, which increased the hardness of the chitosan matrix. At the same time, thick mineral layer limited the conformation of the CS during compression, redistributed effectively the strain energy within materials and improve the toughness [44]. With the elongation of mineralization time, the mineral layer became thicker (Figure 4), therefore composites became stiffer and tougher, resulting in higher compression strength and modulus.

4. Conclusions

In a summary, biomimetic mineralization of CS scaffolds was performed successfully in a rapid and efficient approach. HAP crystals formed in scaffolds possessed higher crystallinity than that in solution. HAP mineral layer densely covered CS both outside and inside surfaces. Moreover, the mineralized HAP layer increased the mechanical properties of HAP-CS bio-composites. A mechanism was proposed to elucidate the formation, and the effects of CS on the nucleation of HAP were analyzed not only from the viewpoint of nucleation kinetics but also from the viewpoint of a molecular level. We can foresee that the one-pot process to form large quantities of mineralized materials and nano HAP. Further work is underway to study the properties of the 3D porous hybrid materials.

Acknowledgements

The work was supported by the National HighTechnology Research and Development Program of China ('863' Program, 2007AA091603). Li L.H. thanks for the financial support by the MPIKG and DAAD exchange fellowship of Germany.

References

[1] Elliot J.: Structure and chemistry of the apatites, and other calcium orthophosphates. Elsevier, Amsterdam (1994).

[2] Webster T., Ergun C., Doremus R., Siegel R., Bizios R.: Enhanced functions of osteoblasts on nanophase ceramics. Biomaterials, **21**, 1803–1810 (2000). DOI: 10.1016/S0142-9612(00)00075-2

[3] Alves N. M., Leonor I. B., Azevedo H. S., Reis R. L., Mano J. F.: Designing biomaterials based on biomineralization of bone. Journal of Materials Chemistry, **20**, 2911–2921 (2010).
DOI: 10.1039/B910960A

[4] Green D., Walsh D., Mann S., Oreffo R.: The potential of biomimesis in bone tissue engineering: Lessons from the design and synthesis of invertebrate skeletons. Bone, **30**, 810–815 (2002).
DOI: 10.1016/S8756-3282(02)00727-5

[5] Li Q-L., Chen Z-Q., Dawell B. W., Zeng Q., Li G., Ou G-M., Wu M-Y.: Biomimetic synthesis of the composites of hydroxyapatite and chitosan–phosphorylated chitosan polyelectrolyte complex. Materials Letters, **60**, 3533–3536 (2006).
DOI: 10.1016/j.matlet.2006.03.046

[6] Li L. H., Kommareddy K. P., Pilz C., Zhou C. R., Fratzl P., Manjubala I.: In vitro bioactivity of bioresorbable porous polymeric scaffolds incorporating hydroxyapatite microspheres. Acta Biomaterialia, **6**, 2525–2531 (2010).
DOI: 10.1016/j.actbio.2009.03.028

[7] Di Martino A., Sittinger M., Risbud M.: Chitosan: A versatile biopolymer for orthopaedic tissue-engineering. Biomaterials, **26**, 5983–5990 (2005).
DOI: 10.1016/j.biomaterials.2005.03.016

[8] Simkiss K., Wilbur K. M.: Biomineralization. Cell biology and mineral deposition. Academic Press, San Diego (1989).

[9] Bigi A., Boanini E., Panzavolta S., Roveri N., Rubin K.: Bonelike apatite growth on hydroxyapatite-gelatin scaffolds from simulated body fluid. Journal of Biomedical Materials Research, **59**, 709–714 (2002).
DOI: 10.1002/jbm.10045

[10] Pang Y., Bao X.: Influence of temperature, ripening time and calcination on the morphology and crystallinity of hydroxyapatite nanoparticles. Journal of the European Ceramics Society, **23**, 1697–1704 (2003).
DOI: 10.1016/S0955-2219(02)00413-2

[11] Phillips M., Darr J., Luklinska Z., Rehman I.: Synthesis and characterization of nano-biomaterials with potential osteological applications. Journal of Materials Science: Materials in Medicine, **14**, 875–882 (2003).
DOI: 10.1023/A:1025682626383

[12] Lim G., Wang J., Ng S., Chew C., Gan L.: Processing of hydroxyapatite via microemulsion and emulsion routes. Biomaterials, **18**, 1433–1439 (1997).
DOI: 10.1016/S0142-9612(97)00081-1

[13] Kothapalli C., Wei M., LeGeros R., Shaw M.: Influence of temperature and aging time on HA synthesized by the hydrothermal method. Journal of Materials Science: Materials in Medicine, **16**, 441–446 (2005).
DOI: 10.1007/s10856-005-6984-5

[14] Wang Y., Zhang S., Wei K., Zhao N., Chen J., Wang X.: Hydrothermal synthesis of hydroxyapatite nanopowders using cationic surfactant as a template. Materials Letters, **60**, 1484–1487 (2006).
DOI: 10.1016/j.matlet.2005.11.053

[15] Riman R., Suchanek W., Byrappa K., Chen C-W., Shuk P., Oakes C.: Solution synthesis of hydroxyapatite designer particulates. Solid State Ionics, **151**, 393–402 (2002).
DOI: 10.1016/S0167-2738(02)00545-3

[16] Zhang F., Zhou Z-H., Yang S-P., Mao L-H., Chen H-M., Yu X-B.: Hydrothermal synthesis of hydroxyapatite nanorods in the presence of anionic starburst dendrimer. Materials Letters, **59**, 1422–1425 (2005).
DOI: 10.1016/j.matlet.2004.11.058

[17] Liu J., Ye X., Wang H., Zhu M., Wang B., Yan H.: The influence of pH and temperature on the morphology of hydroxyapatite synthesized by hydrothermal method. Ceramics International, **29**, 629–633 (2003).
DOI: 10.1016/S0272-8842(02)00210-9

[18] Rhee S-H.: Synthesis of hydroxyapatite via mechanochemical treatment. Biomaterials, **23**, 1147–1152 (2002).
DOI: 10.1016/S0142-9612(01)00229-0

[19] Darr J., Guo Z., Raman V., Bououdina M., Rehman I.: Metal organic chemical vapour deposition (MOCVD) of bone mineral like carbonated hydroxyapatite coatings. Chemistry Communication, **6**, 696–697 (2004).
DOI: 10.1039/b312855p

[20] Danilchenko S., Koropov A., Sulkio-Cleff B., Sukhodub L.: Thermal behavior of biogenic apatite crystals in bone: An X-ray diffraction study. Crystal Research Technology, **41**, 268–275 (2006).
DOI: 10.1002/crat.200510572

[21] Ito H., Oaki Y., Imai H.: Selective synthesis of various nanoscale morphologies of hydroxyapatite via an intermediate phase. Crystal Growth and Design, **8**, 1055–1059 (2008).
DOI: 10.1021/cg070443f

[22] Newman W., Newman M.: The chemical dynamics of bone mineral. The University of Chicago Press, Chicago (1958).

[23] González M., Hernández E., Ascencio J., Pacheco F., Pacheco S., Rodríguez R.: Hydroxyapatite crystals grown on a cellulose matrix using titanium alkoxide as a coupling agent. Journal of Materials Chemistry, **13**, 2948–2951 (2003).
DOI: 10.1039/b306846n

[24] Chen J. D., Wang Y. Y., Wei K., Zhang S. H., Shi X. T.: Self-organization of hydroxyapatite nanorods through oriented attachment. Biomaterials, **28**, 2275–2280 (2007).
DOI: 10.1016/j.biomaterials.2007.01.033

[25] Huang F., Shen Y., Xie A., Zhu J., Zhang C., Li S.: Study on synthesis and properties of hydroxyapatite nanorods and its complex containing biopolymer. Journal of Materials Science, **42**, 8599–8605 (2007).
DOI: 10.1007/s10853-007-1861-x

[26] Choi A., Ben-Nissan B.: Sol-gel production of bioactive nanocoatings for medical applications. Part II: current research and development. Nanomedicine, **2**, 51–61 (2007).
DOI: 10.2217/17435889.2.1.51

[27] Follet H., Boivin G., Rumelhart C., Meunier P.: The degree of mineralization is a determinant of bone strength: A study on human calcanei. Bone, **34**, 783–789 (2004).
DOI: 10.1016/j.bone.2003.12.012

[28] Kerin A., Wisnom M., Adams M.: The compressive strength of articular cartilage. Journal of Engineering in Medicine, **212**, 273–280 (1998).

[29] Seal B., Otero T., Panitch A.: Polymeric biomaterials for tissue and organ regeneration. Materials Science and Engineering R: Reports, **34**, 147–230 (2001).
DOI: 10.1016/S0927-796X(01)00035-3

[30] Keaveny T., Hayes W.: Mechanical properties of cortical and trabecular bone. in 'Bone, Volume VII: A Treatise' (ed.: Hall B. K.) CRC press, Boca Raton, 285–344 (1993).

[31] Zioupos P., Currey J.: Changes in the stiffness, strength, and toughness of human cortical bone with age. Bone, **22**, 57–66 (1998).
DOI: 10.1016/S8756-3282(97)00228-7

[32] Qiu G., Mei X., Hong Z.: The development of artificial articular cartilage–PVA-hydrogel. Bio-Medical Materials and Engineering, **8**, 75–81 (1998).

[33] Cölfen H., Mann S.: Higher-order organization by mesoscale self-assembly and transformation of hybrid nanostructures. Angewandte Chemie International Edition, **42**, 2350–2365 (2003).
DOI: 10.1002/anie.200200562

[34] Chen S., Yu S-H., Yu B., Ren L., Yao W., Cölfen H.: Solvent effect on mineral modification: Selective synthesis of cerium compounds by a facile solution route. Chemistry – A European Journal, **10**, 3050–3058 (2004).
DOI: 10.1002/chem.200306066

[35] Gouveia D. S., Bressiani A. H. A., Bressiani J. C.: Phosphoric acid rate addition effect in the hydroxyapatite synthesis by neutralization method. Materials Science Forum, **530–531**, 593–598 (2006).
DOI: 10.4028/www.scientific.net/MSF.530-531.593

[36] Liu C., Huang Y., Shen W., Cui J.: Kinetics of hydroxyapatite precipitation at pH 10 to 11. Biomaterials, **22**, 301–306 (2001).
DOI: 10.1016/S0142-9612(00)00166-6

[37] Inskeep W., Silvertooth J.: Kinetics of hydroxyapatite precipitation at pH 7.4 to 8.4. Geochimica et Cosmochimica Acta, **52**, 1883–1893 (1988).
DOI: 10.1016/0016-7037(88)90012-9

[38] Suzuki O.: Interface of synthetic inorganic biomaterials and bone regeneration. International Congress Series, **1284**, 274–283 (2005).
DOI: 10.1016/j.ics.2005.06.066

[39] Rudin V., Komarov V., Melikhov I., Minaev V., Orlov A., Bozhevolnov V.: Method for producing nano-sized crystalline hydroxyapatite. U.S. Patent 7169372, USA (2007).

[40] Moon P., Sandí G., Stevens D., Kizilel R.: Computational modeling of ionic transport in continuous and batch electrodialysis. Journal of Materials Science, **39**, 2531–2555 (2004).
DOI: 10.1081/SS-200026714

[41] Fulmer M., Brown P.: Hydrolysis of dicalcium phosphate dihydrate to hydroxyapatite. Materials Science: Materials in Medicine, **9**, 197–202 (1998).
DOI: 10.1023/A:1008832006277

[42] Jiang H., Liu X-Y., Zhang G., Li Y.: Kinetics and template nucleation of self-assembled hydroxyapatite nanocrystallites by chondroitin sulfate. The Journal of Biological Chemistry, **280**, 42061–42065 (2005).

[43] Liu X.: Generic mechanism of heterogeneous nucleation and molecular interfacial effects. in 'Advances in crystal growth research' (ed.: Saito K.) Elsevier, Amsterdam, 42–61 (2001).

[44] Gupta H., Seto J., Wagermaier W., Zaslansky P., Boesecke P., Fratzl P.: Cooperative deformation of mineral and collagen in bone at the nanoscale. PNAS, **103**, 17741–17746 (2006).
DOI: 10.1073/pnas.0604237103

eXPRESS Polymer Letters Vol.5, No.6 (2011) 555–568
Available online at www.expresspolymlett.com
DOI: 10.3144/expresspolymlett.2011.54

Preparation and properties of mesoporous silica/bismaleimide/diallylbisphenol composites with improved thermal stability, mechanical and dielectric properties

J. Hu, A. Gu, G. Liang, D. Zhuo, L. Yuan*

Department of Materials Science and Engineering, College of Chemistry, Chemical Engineering and Materials Science, Soochow University, Suzhou, Jiangsu 215123, China

Received 2 November 2010; accepted in revised form 4 January 2011

Abstract. New composites with improved thermal stability, mechanical and dielectric properties were developed, which consist of 2,2′-diallylbisphenol A (DBA)/4,4′-bismaleimidodiphenylmethane (BDM) resin and a new kind of organic/inorganic mesoporous silica (MPSA). Typical properties (curing behavior and mechanism, thermal stability, mechanical and dielectric properties) of the composites were systematically investigated, and their origins were discussed. Results show that MPSA/DBA/BDM composites have similar curing temperature as DBA/BDM resin does; however, they have different curing mechanisms, and thus different crosslinked networks. The content of MPSA has close relation with the integrated performance of cured composites. Compared with cured DBA/BDM resin, composites with suitable content of MPSA show obviously improved flexural strength and modulus as well as impact strength; in addition, all composites not only have lower dielectric constant and similar frequency dependence, more interestingly, they also exhibit better stability of frequency on dielectric loss. For thermal stability, the addition of MPSA to DBA/BDM resin significantly decreases the coefficient of thermal expansion, and improves the char yield at high temperature with a slightly reduced glass transition temperature. All these differences in macro-properties are attributed to the different crosslinked networks between MPSA/DBA/BDM composites and DBA/BDM resin.

Keywords: *thermosetting resins, bismaleimide, meosoporous silica, dielectric properties, structure-property*

1. Introduction

Advancements in semiconductor miniaturization have propelled an increasing interest in high performance insulating materials, which are characterized with outstanding integrated properties including high mechanical properties, low dielectric constant and loss, good thermal stability, and desirable lower coefficient of thermal expansion (CTE). Thermosetting resins have gained considerable attention owing to their attractive processing characteristics and strong design-ability, so they are considered as the most promising materials for producing insulators [1, 2].

Bismaleimide (BMI), considered as a thermosetting polyimide, has been widespread used in various electronics and advanced technological applications. A few examples of these applications include radar and microwave structural composites, stealth technologies, space-ware composites, circuit boards, interconnects, and adhesives for microelectronics applications (e.g. flexible and rigid die-attach adhesives) [3–5]. However, its thermal stability, mechani-

*Corresponding author, e-mail: ajgu@suda.edu.cn

cal and dielectric properties need to be improved to meet the harsh requirements of future cutting-edge fields.

In fact, developing high performance insulators based on BMI resin has been one of the hottest topics in recent years. Some kinds of inorganic fillers have been used to prepare BMI resin matrix composites [6–9], of them mesoporous silica has attracted considerable interests owing to its highly ordered and uniform mesoporosity [10] as well as extremely low dielectric constant (1.4–2.1) [11–14]. However, present mesoporous silica mainly consists of Si–O–Si like zeolite, showing brittleness and poor interaction with organic polymers, and thus can not significantly improve the integrated performance of original polymers.

This article gives the first presentation of preparing new composites based on a new organic/inorganic mesoporous silica (MPSA) with functional $–NH_2$ groups and 2,2′-diallylbisphenol A (DBA) modified 4,4′-bismaleimidodiphenylmethane (BDM) resin, and systematically investigating the influence of MPSA on the typical properties (curing behavior and mechanism, thermal stability, mechanical and dielectric properties) of composites and their origins. The aim of this article is not only to develop a new kind of high performance insulating composite, but also to provide a new example in evaluating the relationship of structure-property of advanced polymeric composites.

2. Experimental

2.1. Materials

4, 4′-Bismaleimidodiphenol methane (BDM) was obtained from Fengguang Chemical Co., Ltd. (China). 2, 2′-Diallylbisphenol A (DBA) was purchased from Laiyu Chemical Factory (China). γ-Aminopropyltriethoxysilane (analytical grade) was supplied by Jingzhou Jianghan Chemical Co., Ltd. (China). Tetraethoxysilane, tetramethylammonium hydroxide·$5H_2O$, methanol, dimethyldichlorosilane, hexane, and dimethylformamide were commercial products with analytical grades, they were purchased from Sinopharm Chemical Reagent Co., Ltd (China), and purified prior to use.

2.2. Preparation of MPSA

Cubic octameric silicate anion was prepared according to literature [15]. 20.8 g (0.1 mol) tetraethoxysilane was added dropwise into a three-necked bottom flask containing 0.1 mol tetramethylammonium hydroxide and 91 ml water. The reaction mixture was vigorously stirred at 23±2°C for 24 h, and then 60°C for 10 h. After that, the mixture was concentrated by distillation under reduced pressure. The concentrated product was cooled to 4°C, and then microcrystallites were precipitated from the cool solution. The crystal was separated by filtration, washed with acetone and dried in vacuum to afford cubic octameric silicate anion, $(Me_4N)_8Si_8O_{20}$, coded as D4R.

5–10 ml methanolic solution of D4R (2 g) was added dropwise to a mixture of dimethyldichlorosilane (2 ml), hexane (30 ml) and dimethylformamide (50 ml) with vigorous stirring in an ice bath. After the mixture was stirred for 1 h, 100 ml water was added dropwise in 10 min, followed by continuous stirring for 20 min at room temperature. After that, a hexane solution containing the resultant was separated, and hexane was removed at 60°C in vacuum, producing white solid (N-MPS) which was heated to 250°C in air and maintained at that temperature for 1.5 h, and the resultant product is coded as MPS. 10 g MPS were added into 20 ml ethanol solution of γ-aminopropyl triethoxy silane (1.5 g) with ultrasonic agitation for 30 min to form a homogenous suspension. Then distilled water (2.22 g) was poured into the suspension with magnetic stirring for 4 h at 50–60°C. The suspension was separated by filtration, washed with ethanol and dried in air at about 100°C. The resultant material was ground to pass through a 400 mesh sieve for analyses, and was coded as MPSA.

The structure of MPSA is illustrated in Figure 1 and Figure 2.

Solid-state ^{29}Si NMR of MPS (ppm): –50.5 (T_2, $CH_3Si(OSi)_2(O^-)$), –60.7 (T_3, $CH_3Si(OSi)_3$), –13.3 (D_2, $Si(CH_3)_2(O^-)_2$), –96.2 (Q_3, $Si(OSi)_3(O^-)$), –104.6 (Q_4, $Si(OSi)_4$). The existence of T_2, T_3 and Q_3 demonstrates that some D units in MPS are oxidized during the heat treatment.

FTIR of MPSA (KBr, cm^{-1}): 3440 (–OH stretching vibration), 2965 (C–H stretching vibration), 1265 ($Si–CH_3$ deformation vibration), 1083 (Si–O–Si stretching vibration), 1641 ($–NH_2$ deformation vibration), 850, 806 ($Si–CH_3$ stretching vibration).

The specific surface area of N-MPS is 22 m^2/g, while MPSA is 238 m^2/g, indicating that MPSA has

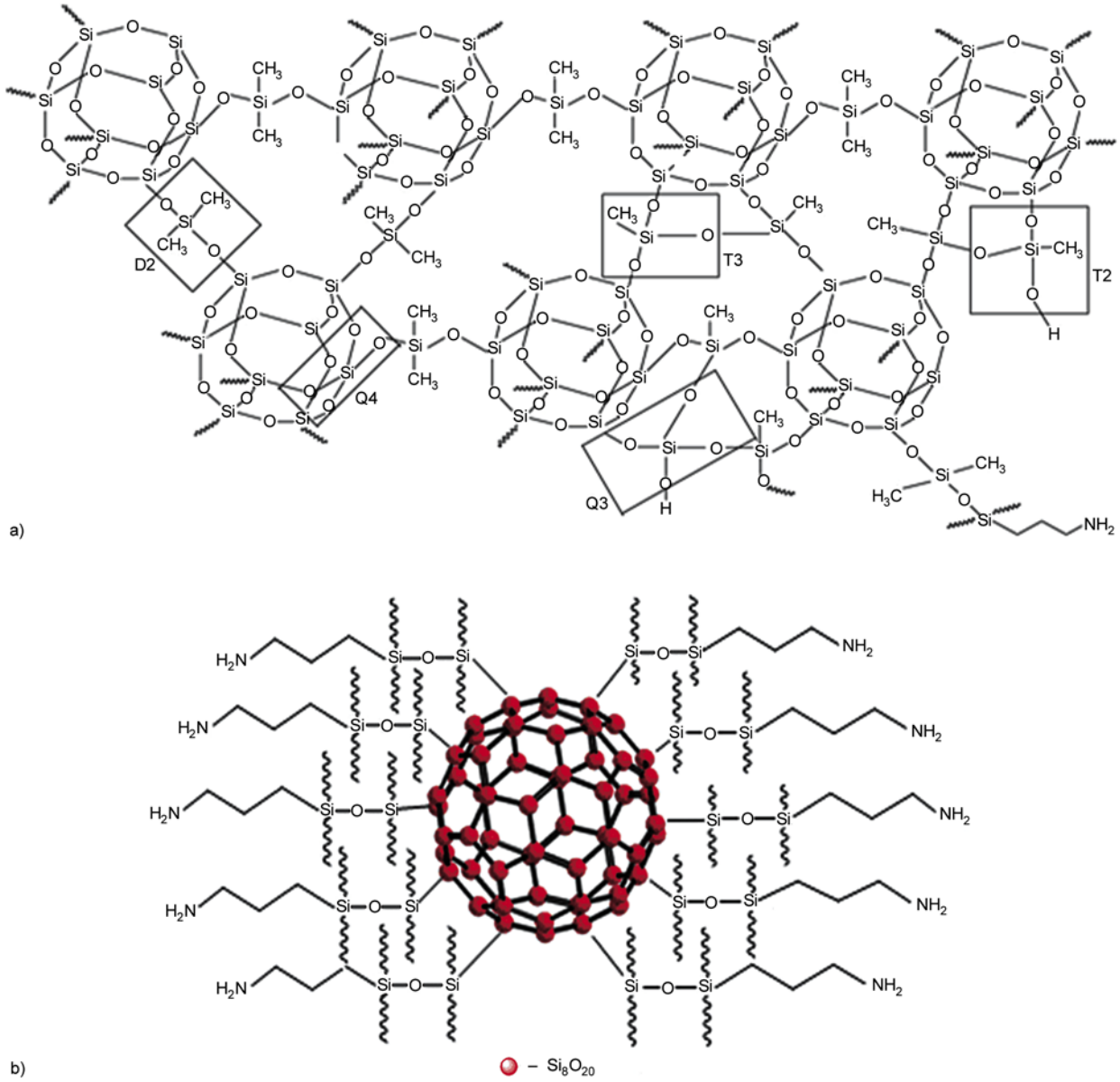

Figure 1. The chemical connection of MPSA (a), and chemical structure of MPSA (b)

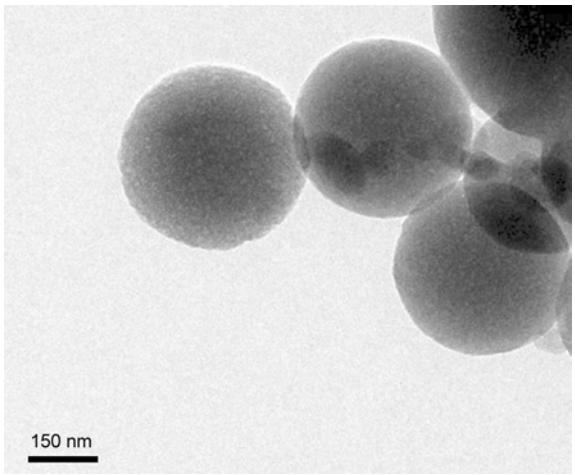

Figure 2. The TEM micrograph of MPSA

a large amount of porosity. Some researchers have used similar method to demonstrate the existence of the 'porous' structure [14, 16–18].

2.3. Preparation of MPSA/DBA/BDM composites

Four formulations (Table 1) were evaluated to see the effect of differing stoichiometry of MPSA on the processing and performance parameters, and also to establish the formulational latitude this system provides.

Appropriate quantities of BDM and DBA were placed in a beaker with a mechanical stirrer and a thermometer. The mixture was heated to 130–135°C,

Table 1. Formulations and typical data from DSC analyses of DBA/BDM resin and MPSA/DBA/BDM composites

Code	Weight ratio DBA:BDM:MPSA	T_{on} [°C]	T_{exo} [°C]	ΔH [w/g]	ρ (E′) [mol/m^3]
DBA/BDM	82: 100:0.00	199	253	18.45	9492
MPSA1/DBA/BDM	82: 100:1.82	193	252	19.31	10895
MPSA3/DBA/BDM	82: 100:5.46	194	250	18.28	14418
MPSA5/DBA/BDM	82: 100:9.10	199	251	17.52	22149
MPSA8/DBA/BDM	82: 100:14.56	196	250	19.16	21919

and maintained within that temperature range with stirring until a clear and brown liquid was obtained. The liquid was maintained at that temperature for additional 15 min to obtain a transparent liquid. Preweighted MPSA was added to the beaker slowly. After that, the mixture was kept at 130–135°C for 10min to obtain MPSA/DBA/BDM prepolymer.

Each prepolymer was thoroughly degassed at 120°C, and poured into a preheated (120°C) glass mold, then cured per the following curing procedure of 150°C/2 h + 180°C/2 h + 200°C/2 h. After that the cured sample was demolded and postcured in an air oven at 230°C for 4 h. The resultant composite was coded as MPSA/DBA/BDM.

2.4. Preparation of DBA/BDM resin

Appropriate quantities of BDM and DBA were placed in a beaker with a mechanical stirrer and a thermometer. The mixture was heated to 130–135°C and maintained within that temperature range with stirring until a clear and brown liquid was obtained. The liquid was maintained at that temperature for additional 25 min to obtain a transparent liquid, which was DBA/BDM prepolymer.

Each prepolymer was thoroughly degassed at 120°C and poured into a preheated (120°C) glass mold, then cured per the following curing procedure of 150°C/2 h + 180°C/2 h + 200°C/2 h. After that the cured sample was demolded and postcured in an air oven at 230°C for 4 h. The resultant product was cured DBA/BDM resin.

2.5. Measurements

Solid-state ^{29}Si NMR spectrum was recorded using TMS as an internal standard on a UNITY INOVA-400 (400 MHz NMR spectrometer, USA).

Fourier Transform Infrared (FTIR) spectra were recorded between 400 and 4000 cm^{-1} with a resolution of 2 cm^{-1} on a Nicolet FTIR 5700 spectrometer (USA), and the sample powder was pressed into a pellet with KBr.

Differential Scanning Calorimetry (DSC) analyses were done using DSC 200 F3 (NETZSCH, Germany) between 80 and 320°C at a heating rate of 10°C/min in a nitrogen atmosphere.

Dynamic Mechanical Analysis (DMA) scans were performed in single-cantilever blending mode using a TA Instruments dynamic mechanical analyzer (DMA Q800, USA) from 50 to 350°C at a heating rate of 3°C/min and a frequency of 1 Hz.

Dielectric property was conducted over a frequency range from 10 to 10^6 Hz at room temperature using a Broad Band Dielectric Spectrometer (Novocontrol Concept 80 Analyzer, Germany). The dimensions of each sample were (25±0.2)×(25±0.2)×(3±0.1) mm^3. The powders of MPSA were pressed into a pellet with a diameter of 20 mm and a thickness of 3 mm.

Thermogravimetric (TG) analyses were performed using PerkinElmer TGA-7 (USA) at a heating rate of 10°C/min in a nitrogen atmosphere from 60 to 780°C. The initial decomposition temperature (T_{di}) was defined as the point of intersection at which the tangent of onset temperature and the tangent of the maximum degradation rate temperature.

Coefficient of Thermal Expansion (CTE) was measured using Diamond TMA (USA) from 60 to 270°C. Each sample was dried to constant weight under 110°C before tests.

Flexural tests were done using a universal tester (China) according to GB2570-95. Impact strength was measured according to GB2571-95. At least five samples for each system were tested, and the average value was taken as the tested value.

The char residues of DBA/BDM resin and MPSA/DBA/BDM composites were observed by an optical microscope (SMZ-T2, China).

The specific surface (BET) was performed with ASAP2020M (USA) automatic surface analyzer.

3. Results and discussion

3.1. Curing behavior of MPSA/DBA/BDM composites

It is known that the curing behavior of a thermosetting resin determines its cross-linking network, and thereby the properties of the cured resin, so curing behavior is the first issue needs to be investigated on developing any thermosetting resin and related composites.

Figure 3 shows the DSC curves of DBA/BDM and MPSA/DBA/BDM prepolymers, each system shows one exothermic peak in the temperature range from 190 to 300°C, the typical data such as the onset temperature (T_{on}), the maximum temperature of exothermic peaks (T_{exo}), and the amount of exothermic heat (ΔH) obtained from these curves are summarized in Table 1. These results indicate that MPSA/DBA/BDM systems have similar curing temperature and exothermic heat as DBA/BDM; hence the addition of MPSA to DBA/BDM resin does not change the curing profile of the resin. This conclusion can be confirmed from the FTIR spectra of MPSA/DBA/BDM systems with different curing processes as shown in Figure 4. For all systems, as the curing time and the curing temperature increase, the peak intensities of C=C bonds at 3098, 1600, 1153, 910, and 686 cm^{-1} gradually decrease, and finally disappear, suggesting that under the curing and postcuring condition developed herein, the curing of all composites is complete [19].

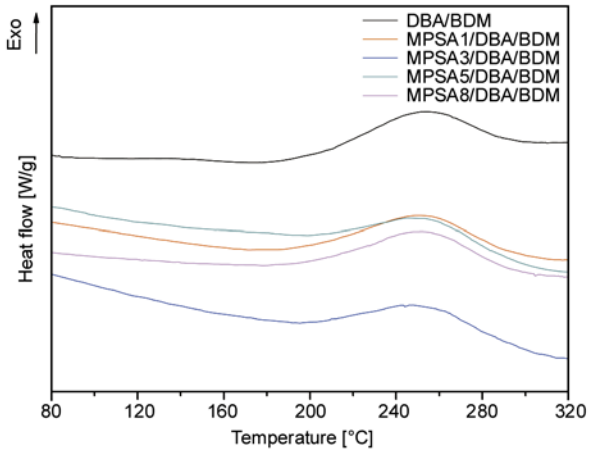

Figure 3. DSC curves of DBA/BDM and MPSA/DBA/BDM prepolymers

Table 2. Coefficient C and CTE values of DBA/BDM and MPSA/DBA/BDM composites

Sample	Coefficient C	CTE [ppm/°C]
DBA/BDM	N/A	93
MPSA1/DBA/BDM	0.91	85
MPSA3/DBA/BDM	0.70	75
MPSA5/DBA/BDM	0.49	80
MPSA8/DBA/BDM	0.52	90

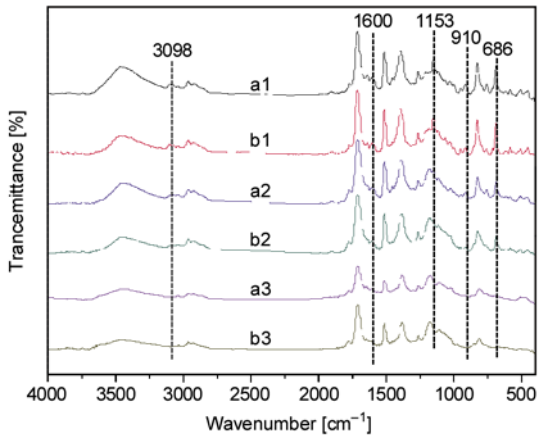

Figure 4. FTIR spectra of DBA/BDM (a) and MPSA5/DBA/BDM (b) after being cured via different procedures (1 – without curing; 2–150°C/2 h; 3 – after postcured)

However, the composites have different curing mechanism from DBA/BDM resin. For DBA/BDM resin, its curing mechanism contains multiple reactions, for example 'Ene' and 'Diels-Alder' reactions between maleimide group of BDM and allyl group of DBA, and the self-polymerization of BDM via C=C bonds (Figure 5a) [20, 21]; while in the case of MPSA/DBA/BDM system, besides above reactions of DBA/BDM, there is a Michael reaction between maleimide and $-NH_2$ groups [22]. This additional reaction not only supplies a chemical bonding between MPSA and DBA/BDM (Figure 5b) to guarantee a good dispersion of MPSA in the matrix, but also leads to a different structure of crosslinked network.

Specifically, the effect of MPSA on the crosslinked structure is complicated, because MPSA is an organic/inorganic hybrid containing flexible Si–O–Si bonds and aliphatic chains, rigid SiO_2 with cage structure as well as functional $-NH_2$ groups. First, because the Michael reaction between BDM and $-NH_2$ takes place at lower temperature than the homopolymerization of BDM does, so the addition of MPSA to DBA/BDM resin will produce flexible segments, and decrease the amount of the rigid polybismaleimide. Second, although the content of MPSA is small, there are a lot of $-NH_2$ groups on the surface of MPSA, meaning that the presence of MPSA tends to shorten the distance between the-crosslinking points, and thus increases the crosslink-

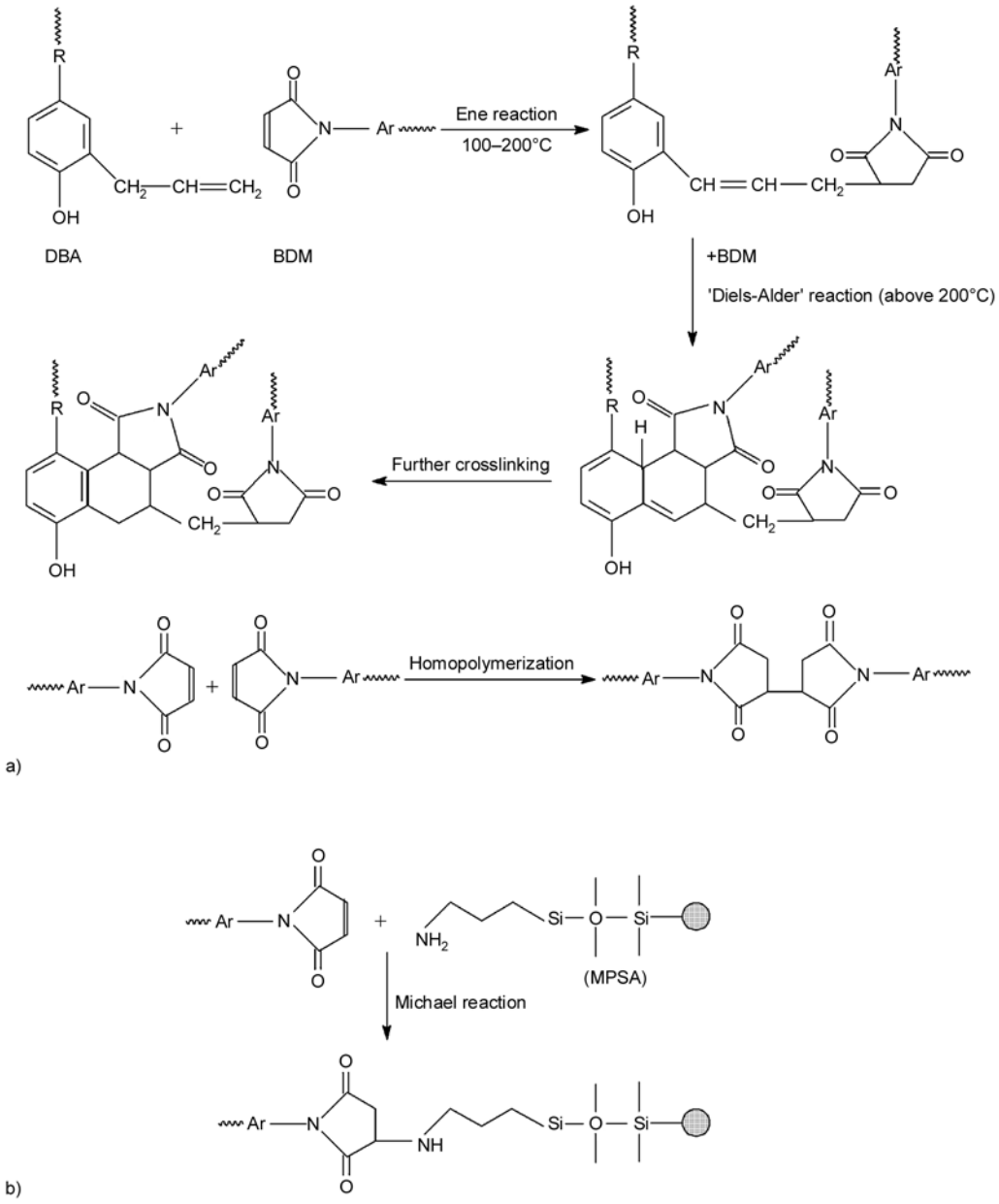

Figure 5. The chemical reactions among BDM, DBA (a) and MPSA (b)

ing density ($\rho_{(E')}$) of the resultant network. Third, the cage units of MPSA connect with each other to form a compact network, as one part of the whole crosslinked network of composites, tending to improve the crosslinking density of the composites. In order to confirm the effect of MPSA on the crosslink density, the $\rho_{(E')}$ values of DBA/BDM resin and MPSA/DBA/BDM composites were calculated. Generally, the $\rho_{(E')}$ values of a highly crosslinked polymer and related particle filled composites can be calculated by the classical equation based on the statistical theory of rubber elasticity [23] as shown in Equation (1):

$$\rho_{(E')} = \frac{G'}{3\Phi RT} \tag{1}$$

where G' is the storage modulus (Figure 6) of the sample at the temperature T from DMA analyses; Φ is the front factor, and assumed to be 1 [23]; T is the absolute temperature at which the sample is in rubbery state, herein T is selected as the temperature which is 40°C higher than the glass transition temperature; R is the gas constant.

According to Equation (1), the calculated $\rho_{(E')}$ values of cured DBA/BDM resin and MPSA/DBA/BDM composites were summarized in Table 1. It can be seen that all composites have bigger crosslink

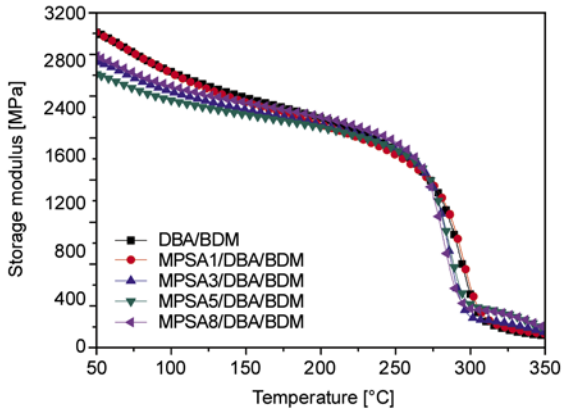

Figure 6. Storage moduli of cured DBA/BDM resin and MPSA/DBA/BDM composites

densities than DBA/BDM resin; moreover, with increasing the content of MPSA, the crosslink density of composite initially increases and then levels off.

3.2. Mechanical properties of MPSA/DBA/BDM composites

Flexural property is usually used for evaluating the mechanical properties of a material because the flexural loading is very complicated and may contain different types of loadings such as tensile, shearing and/or compressive loads [24]. Figure 7 shows the flexural properties of cured DBA/BDM resin and MPSA/DBA/BDM composites. With a small addition of MPSA to DBA/BDM resin, both flexural strength and modulus increase, and then reach their respective maximum values at about 3 wt% of MPSA. Specifically, the maximum flexural strength and modulus are 187 MPa and 4.5 GPa, respectively, which are about 20 and 10% higher than the corresponding values of DBA/BDM resin. Further increasing the content of MPSA, both flexural strength and modulus of composites decrease.

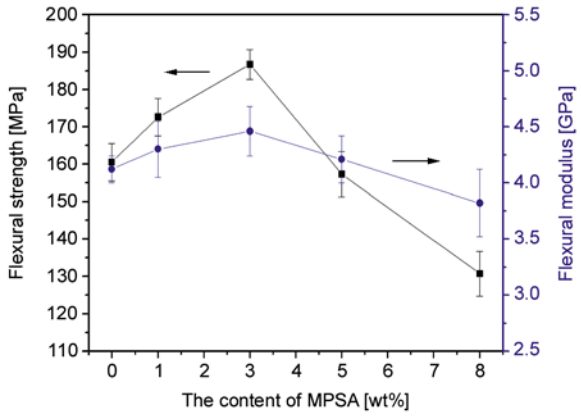

Figure 7. Flexural strengths and moduli of cured DBA/BDM resin and MPSA/DBA/BDM composites

Although some mesoporous silica/polymer composites have been reported [14, 25], the majority of them are in the form of films; hence their flexural properties were almost not investigated. With regard to polyhedral oligomeric silsesquioxane (POSS)/polymer composites, only several pieces of literature report the flexural properties. Liang's group prepared POSS/cyanate ester nanocomposites, and found that the flexural modulus of the nanocomposite with 3 wt% POSS is about 15% higher than that of neat cyanate ester resin, while the composite has the similar flexural strength as the resin does [26]. Li's group also reported similar results in the POSS/epoxy nanocomposites [27]. However, Rashid's group reported a different phenomenon [28], in detail, the addition of POSS to epoxy resin can obviously increase the flexural strength, but does not change the flexural modulus. Comparing these results in literature with the data in this paper, an interesting but preliminary conclusion could be stated that MPSA which consists of a large amount of POSS units and organic chains maybe more effective in improving both flexural strength and modulus than single POSS. A reasonable mechanism is not clear, which is worthy to be intensively investigated.

It is well known that the flexural strength of a material reflects the rigidity and toughness of the material, so those factors which are beneficial to improve the stiffness and/or the toughness can improve the flexural strength. Flexural modulus reflects the co-inherent energy of a material, and the ability to resist strain, so a thermosetting resin with bigger molecular weight and a larger amount of rigid structure generally has higher modulus [29]. For a well-dispersed particle/thermosetting resin composite, the crosslinking density is an important factor of determining the stiffness and toughness, and thus has significant influence on the flexural strength; in addition, the interfacial adhesion determines the stress transfer under an external loading, and thus provides additional contribution to the flexural properties.

As for MPSA/DBA/BDM composites, the co-reaction between MPSA and DBA/BDM resin supplies good interfacial adhesion, and a large amount of aminopropyl chains grafted on the surface of MPSA are expected to constitute a rough particle surface,

which may give rise to a distinct structural difference between the interfacial zone and the bulk, and thus further improve the strength and modulus of MPSA/DBA/BDM composites [30, 31]. In addition, compared with cured DBA/BDM resin, MPSA/DBA/BDM composites have larger crosslink density, leading to the increment of flexural strength and modulus. In detail, the Michael reaction between maleimide and $–NH_2$ groups in composites decreases the amount of the rigid homopolymer of BDM, resulting in decreased flexural properties. Note that the Michael reaction also introduces flexible Si–O–Si chains into the crosslinked network, leading to increased flexural strength but decreased modulus. Obviously these opposite influences play a combined role on the flexural properties, and therefore there is an optimum content of MPSA to get the highest flexural strength and modulus.

Figure 8 shows the impact strengths of cured DBA/BDM resin and MPSA/DBA/BDM composites with different contents of MPSA, it can be seen that the impact strength of MPSA/DBA/BDM composites is closely dependent on the content of MPSA, following the similar trend of flexural properties. Specifically, there exists an optimum content of MPSA to obtain the biggest impact strength, that is, the impact strengths of MPSA3/DBA/BDM is 17.2 kJ/m^2, about 1.4 times of that of DBA/BDM resin.

Similar increment of impact strength owing to the addition of rod-like attapulgite to polyimide resin is observed [30], which is considered as the particle toughening effect. Some other models including crack pinning, crack bridging, and debonding of particles as well as crack deflection have been proposed to explain this effect [32, 33].

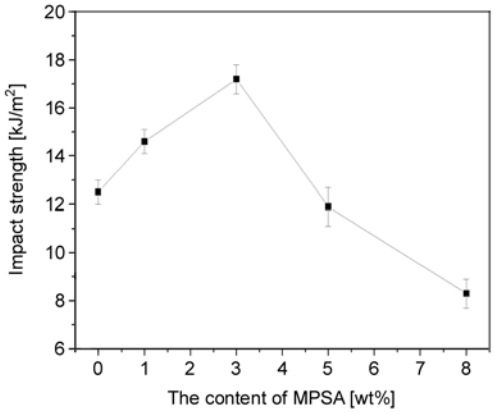

Figure 8. Impact strengths of cured DBA/BDM resin and MPSA/DBA/BDM composites

Besides, two opposite influences are also responsible for the effect of the content of MPSA on the impact strength. In detail, the introduced flexible Si–O–Si chains and decreased amount of rigid homopolymer of BDM are beneficial to increase the impact strength; while oppositely, the increased crosslinking density will decrease the impact strength. As a result, the impact strength of MPSA/DBA/BDM composites exhibit strong composition dependence.

The coefficient (C) is generally used to describe the effectiveness of fillers on the modulus of composite, which can be calculated by Equation (2) [34]:

$$C = \frac{\left(\frac{E'_G}{E'_R}\right)_{composite}}{\left(\frac{E'_G}{E'_R}\right)_{resin}} \tag{2}$$

where E'_G and E'_R are the storage moduli in the glassy and rubbery regions from DMA tests, respectively.

For MPSA/DBA/BDM composites developed herein, the modulus of each composite at 60 or 320°C is regarded as E'_G or E'_R, respectively. Table 2 gives the calculated coefficient C values of all MPSA/DBA/BDM composites, because a small C value reflects a big effectiveness of fillers on the modulus of composite, so it can be concluded that the composition of MPSA/DBA/BDM composites has obvious effect on the C value. The composite with larger content of MPSA tends to have a smaller C value, that is, with the increase of the content of MPSA, the C value obviously decreases; however when the content of MPSA is bigger than 5 wt%, the C value almost levels off.

From the viewpoint of molecular structure, the intensity of the storage modulus below T_g reflects the rigidity of materials. Figure 6 shows that the intensities of storage moduli of MPSA/DBA/BDM composites in glassy state are lower than that of DBA/BDM resin, this phenomenon is different from the common inorganic filler/polymer composites [35], indicating that MPSA is not a rigid filler owing to the presence of a large amount of organic chains between POSS structures as well as the porous.

3.3. Dielectric properties

As described above, one important reason to synthesize and employ MPSA for developing high performance insulators is that MPSA is expected to have extremely low dielectric constant and loss owing to its unique porous structure. Figures 9 and 10 confirm this expectation, so it is easy to understand that the addition of MPSA to DBA/BDM resin decreases the dielectric constant over the whole frequency range, and the larger is the content of MPSA, the lower is the dielectric constant; however, this trend does not fit MPSA8/DBA/BDM composite. Specifically, the magnitude of dielectric constant follows the order of DBA/BDM ≈ MPSA8/DBA/BDM > MPSA1/DBA/BDM > MPSA3/DBA/BDM > MPSA5/DBA/BDM. This is because with the increase of the content of MPSA, the amount of the flexible chains resulting from the Michael reaction between BDM and MPSA increases, at the same time, the amount of the rigid polybismaleimide decreases, so the polarization and relaxation of dipoles are easy to occur, and thus increase the dielectric constant and loss. This influence enhances with the increase of the content of MPSA.

For the binary composites, its dielectric constant can be calculated by Equation (3) [36]:

$$\log\varepsilon_c = Y_1 \cdot \log\varepsilon_1 + Y_2 \cdot \log\varepsilon_2 \quad (3)$$

where ε_c, ε_1, and ε_2 stand for the dielectric constant of MPSA/DBA/BDM composites, DBA/BDM resin and MPSA at 10 Hz, respectively; Y_1 and Y_2 represent the volume fraction of DBA/BDM resin and MPSA, respectively.

The theoretical dielectric constants calculated by Equation (3) and the experimental data of MPSA/DBA/BDM composites are shown in Figure 11. There is obvious deviation between theoretical and experimental values, and the larger is the content of MPSA, the bigger is the deviation. This is because that Equation (3) is developed without considering the interfacial effect on the dielectric constant of a composite. A good interfacial adhesion is beneficial to restrict the polarization and relaxation of dipoles, so it is not surprise to find that the dielectric constant of MPSA/DBA/BDM composites has a deviation from the values calculated by Equation (3), and the composite with larger content of MPSA has bigger difference. In addition, it is expected that MPSA/ DBA/BDM composites have lower dielectric constant than the values calculated from Equation (3). However, MPSA8/DBA/BDM composite does not follow this expectation again, owing to the reason described above.

The dependence of dielectric loss on frequency for DBA/BDM resin and all composites is shown in

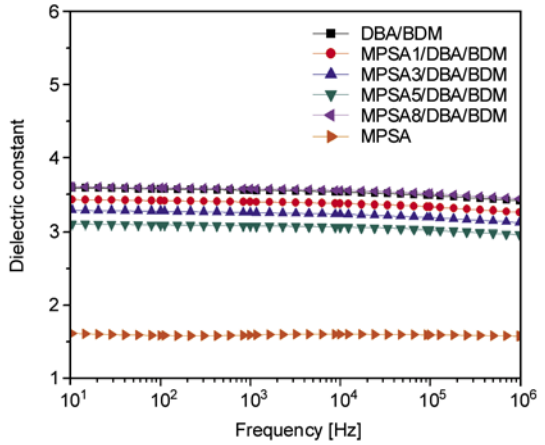

Figure 9. Dependence of dielectric constant on frequency of cured DBA/BDM resin and MPSA/DBA/BDM composites

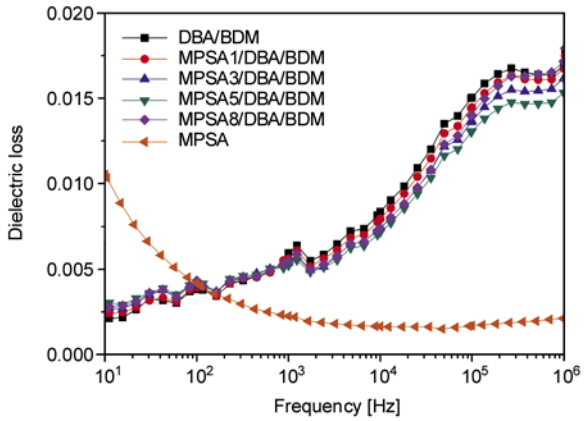

Figure 10. Dependence of dielectric loss on frequency of cured DBA/BDM resin and MPSA/DBA/BDM composites

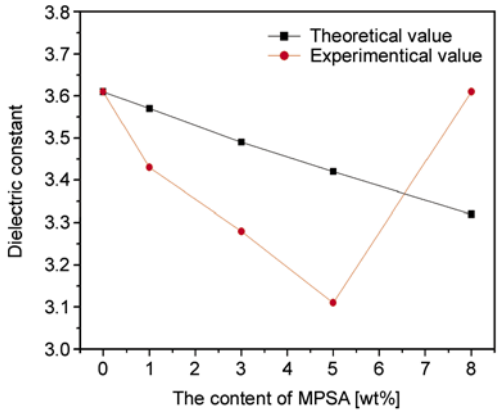

Figure 11. Theoretical and experimental dielectric constants of cured DBA/BDM resin and MPSA/DBA/BDM composites

Figure 10. The dielectric loss of DBA/BDM resin increases with the increase of frequency because the molecule movement can not follow up the variety of frequency of the applied electric field [37]; while that of MPSA shows opposite trend owing to its special structure. MPSA is a kind of organic/inorganic mesoporous silica, the existence of porous structure will lead to big space charge polarization and thus big dielectric loss at low frequency. Therefore, the resultant composites exhibit a combined feature of their separate components. Compared with DBA/BDM resin, MPSA/DBA/BDM composites have slightly bigger dielectric loss at low frequency, and obviously smaller values at high frequency, indicating that these composites have better frequency stability of dielectric loss. This is an important and attractive merit for developing high performance insulators.

3.4. Thermal properties

Heat-resistance of a material can be reflected by many properties, among them the glass transition temperature (T_g), TG behavior and CTE are three most important aspects for high performance insulators.

Several methods can be used to detect the T_g value of a polymer, however, DMA technique is the most effective one [34]. The peak temperature of loss modulus-temperature plot is defined as the glass transition temperature herein. As shown in Figure 12 that DBA/BDM resin shows a sharp peak with a shoulder at higher temperature. By Gaussian fitting [38], each curve can be divided into two peaks, one small peak appears at 296°C, and another big peak appears at 305°C, indicating that DBA/BDM resin has a multi-phase structure, and thus two T_g values. According to the thermal stability, the first damping peak of cured DBA/BDM resin at the lower temperature could be attributed to the T_g of the addition product resulted from the 'Ene' and 'Diels-Alder' reactions between maleimide groups of BDM and allyl groups of DBA; while the second damping peak at higher temperature might be assigned to the homopolymer of BDM and further crosslinked structure between BDM and DBA [19].

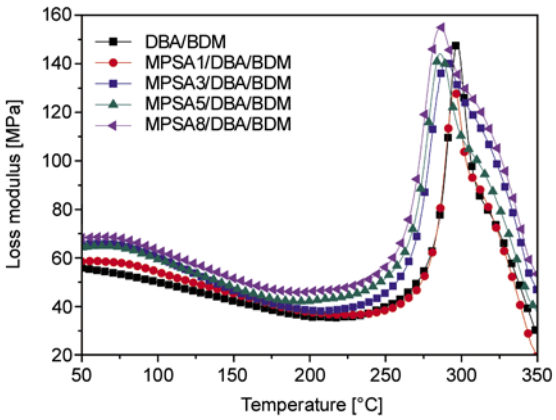

Figure 12. Overlay plots of loss modulus-temperature for cured DBA/BDM resin and MPSA/DBA/BDM composites

MPSA/DBA/BDM composites exhibit similar shapes to those of the DBA/BDM resin, but the first damping peak slightly shifts toward lower temperature, while the second damping peak almost does not change. Obviously, the curing mechanism of composites results in this phenomenon. As discussed above, the curing mechanism of MPSA/DBA/BDM composites not only includes the curing reactions taking place in the DBA/BDM resin, but also contains additional co-reaction between $-NH_2$ groups on MPSA and maleimide groups of BDM, forming flexible Si–O–Si chains, and thus lower T_g value; while oppositely, interfacial confinement effect is conducive to improve the T_g value. Obviously, the above two aspects play a combined role. In addition, the multi-reactions are also responsible for the broadened shapes of damping peaks for composites.

The thermogravimetric behavior can be reflected by TG analyses, Figure 13 shows the TG and DTG curves of all samples, the typical data such as the initial decomposition temperature (T_{di}), the temperature of the maximum degradation rate (T_{max}), and

Table 3. Characteristic data from TG analyses of DBA/BDM and MPSA/DBA/BDM composites

Resin	T_{di} [°C]	T_{max} [°C]	Intensity [%/°C]	$Y_{c\ at\ 780°C}$ [%]	
				Theoretical	Experimental
DBA/BDM	410	450	0.67	29.1	29.1
MPSA1/DBA/BDM	413	449	0.57	30.0	31.8
MPSA3/DBA/BDM	410	449	0.50	31.7	40.7
MPSA5/DBA/BDM	409	449	0.48	33.4	44.3
MPSA8/DBA/BDM	410	449	0.46	35.9	46.1
MPSA	465	534/754	0.04/0.07	86.1	86.1

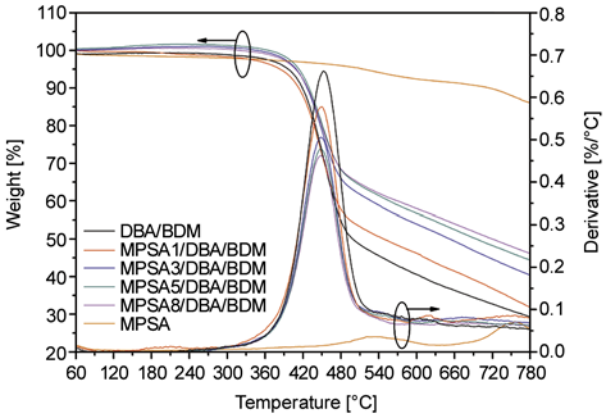

Figure 13. TG and DTG curves of cured DBA/BDM resin and MPSA/DBA/BDM composites

char yield (Y_c) at 780°C obtained from these curves are summarized in Table 3. All composites have similar T_{di} and T_{max} values as DBA/BDM resin, indicating that they have similar thermal degradation mechanism; however, the peak intensity of DBA/BDM resin is significantly higher than that of MPSA/DBA/BDM composites, suggesting that the thermal decomposition is delayed because of the presence of MPSA. It is worth noting that the experimental Y_c of composites is much larger than that of DBA/BDM resin, and even more interestingly, the former is bigger than its theoretical value calculated by the 'Mixture Rule', and this phenomenon is enhanced as the content of MPSA increases, demonstrating that there is a synergistic effect in the composites which is believed to come from the interaction between MPSA and the matrix described above.

Figure 14 shows the micrographs of char residues after TG tests. The char residue of DBA/BDM resin shows loose structure; while that of each composite is dense, and the composite with a larger content of MPSA has denser char residue. That is because a large amount of MPSA will form more amount of inert silica layer, which can act as a thermal barrier to inhibit further degradation of the inner part of the matrix [39]. That is also the reason why the composite with a larger content of MPSA has bigger experimental Y_c than theoretical value.

CTE is a very important property in actual applications, which denotes the dimension stability of a material with the variation of service temperature. For example, heat is produced when a microelectronic product (especially that with high performance) works, so organic resins with a low CTE are needed to reduce the mismatch in thermal expansion among different materials in the product, otherwise the product tends to deform during the service, and may lead to break down [28].

CTE values of DBA/BDM resin and MPSA/DBA/BDM composites over a temperature range from 60–270°C are summarized in Table 2. It is interesting to find that all MPSA/DBA/BDM composites have lower CTE values than DBA/BDM resin. In detail, CTE values of MPSA/DBA/BDM composites are related to the content of MPSA. Specifically, with the initial increase of the content of MPSA, the CTE value decreases, and reaches the minimum value at 3 wt% MPSA; further increasing the content of MPSA, the CTE value gradually increases.

The decreased CTE value for composites is attributed to a combined influence consisting in three aspects. First, the interfacial interaction between MPSA and DBA/BDM resin constrains the movement of the polymer network due to the presence of covalently bonded polymer layers, and thus leads to decreased CTE values; however, second, which also decreases the amount of the homopolymer of BDM, and thus tends to increase the CTE value. Third, the decrement in nanoparticle dispersion at larger loadings, and the effect of decreased interparticle distance which gives rise to the additional loss in configurational entropy at the interface and in density fluctuation in the zone surrounding nanoparticles [40] also increase the CTE value; Obviously, the determining aspect varies with the content of MPSA, the former plays the dominate role when the content of MPSA is small, while the latter becomes the key one when the content of MPSA is big.

4. Conclusions

A new organic/inorganic mesoporous silica (MPSA) is used to develop new high performance bismaleimide/diallylbisphenol A resin matrix composites with improved mechanical and dielectric properties as well as thermal resistance.

The addition of MPSA to DBA/BDM resin does not change the curing profile of DBA/BDM resin, but varies the curing mechanism, leading to different crosslinked networks, and thus the integrated performance of cured composites. Apparently, the content of MPSA exhibits a great influence on the integrated performance of cured composites. The outstanding integrated performance of MPSA/DBA/BDM composites with suitable content of MPSA

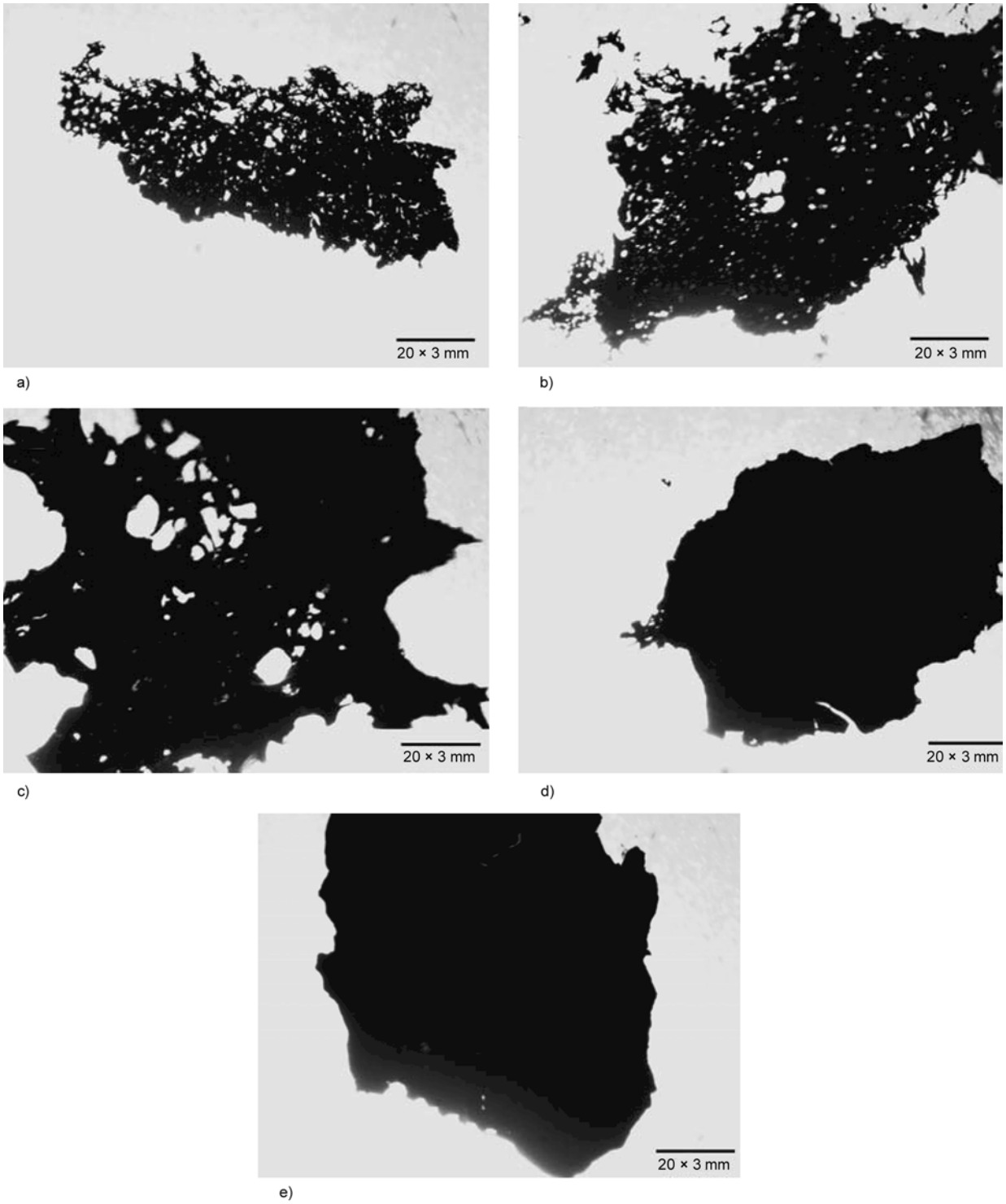

Figure 14. Optical pictures of the char residues of cured DBA/BDM resin (a) and MPSA/DBA/BDM composites (b: MPSA1/DBA/BDM, c: MPSA3/DBA/BDM, d: MPSA5/DBA/BDM, e: MPSA8/DBA/BDM)

show a great potentiality to be used as high performance insulators for applications needing harsh requirements in thermal, mechanical and dielectric properties.

Acknowledgements

The authors thank 'Qing Lan Project' (2008), '333 Talent Project' (2008) and 'Six Talent Peaks' (2009) of Jiangsu Province, and National Natural Science Foundation of China (20974076) for financially supporting this project.

References

[1] Ahner N., Schulz S. E., Blaschta F., Rennau M.: Thermal stability and gap-fill properties of spin-on MSQ low-k dielectrics. Microelectronic Engineering, **84**, 2606–2609 (2007).
DOI: 10.1016/j.mee.2007.06.007

[2] Johnson M., Li Z. J., Wang J. L., Yan Y. S.: Mechanical characterization of zeolite low dielectric constant thin films by nanoindentation. Thin Solid Films, **515**, 3164–3170 (2007).
DOI: 10.1016/j.tsf.2006.01.048

[3] Rajasekaran R., Alagar M., Karikal Chozhan C.: Effect of polyethersulfone and *N*, *N*′-bismaleimido-4,4′-diphenyl methane on the mechanical and thermal properties of epoxy systems. Express Polymer Letters, **2**, 339–348 (2008).
DOI: 10.3144/expresspolymlett.2008.40

[4] Fan S. L., Boey F. Y. C., Abadie M. J. M.: UV curing of a liquid based bismaleimide-containing polymer system. Express Polymer Letters, **1**, 397–405 (2007).
DOI: 10.3144/expresspolymlett.2007.56

[5] Yan H-Q., Wang H-Q., Cheng J.: Interpenetrating polymer networks from the novel bismaleimide and cyanate containing naphthalene: Cure and thermal characteristics. European Polymer Journal, **45**, 2383–2390 (2009).
DOI: 10.1016/j.eurpolymj.2009.04.031

[6] Lu H. B., Shen H. B., Song Z. L., Shing K. S., Tao W., Nutt S.: Rod-like silicate-epoxy nanocomposites. Macromolecular Rapid Communications, **26**, 1445–1450 (2005).
DOI: 10.1002/marc.200500360

[7] Rao Y. Q., Pochan J. M.: Mechanics of polymer-clay nanocomposites. Macromolecules, **40**, 290–296 (2007).
DOI: 10.1021/ma061445w

[8] Liang G. Z., Hu X. L.: Aluminum-borate-whiskers-reinforced bismaleimide composites. 1: Preparation and properties. Polymer International, **53**, 670–674 (2004).
DOI: 10.1002/pi.1401

[9] Yuan L., Ma X. Y., Gu A. J., Yan H. X., Liang G. Z., Wang W., Wu J. Y.: A novel organic rectorite modified bismaleimide/diallylbisphenol A system. Polymers for Advanced Technologies, **20**, 826–833 (2009).
DOI: 10.1002/pat.1328

[10] Park I., Peng H-G., Gidley D. W., Xue S. Q., Pinnavaia T. J.: Epoxy-silica mesocomposites with enhanced tensile properties and oxygen permeability. Chemistry of Materials, **18**, 650–656 (2006).
DOI: 10.1021/cm051768r

[11] Baskaran S., Liu J., Domansky K., Kohler N., Li X. H., Coyle C., Fryxell G. E., Thevuthasan S., Williford R. E.: Low dielectric constant mesoporous silica films through molecularly templated synthesis. Advanced Materials, **12**, 291–294 (2000).
DOI: 10.1002/(SICI)1521-4095(200002)12:4<291::AID-ADMA291>3.0.CO;2-P

[12] Yang C. M., Cho A. T., Pan F. M., Tsai T. G., Chao K. J.: Spin-on mesoporous silica films with ultralow dielectric constants, ordered pore structures, and hydrophobic surfaces. Advanced Materials, **13**, 1099–1102 (2001).
DOI: 10.1002/1521-4095(200107)13:14<1099::AID-ADMA1099>3.0.CO;2-0

[13] Zhao D. Y., Yang P. D., Melosh N., Feng J. L., Chmelka B. F., Stucky G. D.: Continuous mesoporous silica films with highly ordered large pore structures. Advanced Materials, **10**, 1380–1385 (1998).
DOI: 10.1002/(SICI)1521-4095(199811)10:16<1380::AID-ADMA1380>3.0.CO;2-8

[14] Lin J. J., Wang X. D.: Preparation, microstructure, and properties of novel low-κ brominated epoxy/mesoporous silica composites. European Polymer Journal, **44**, 1414–1427 (2008).
DOI: 10.1016/j.eurpolymj.2008.02.022

[15] Hagiwara Y., Shimojima A., Kuroda K.: Alkoxysilylated-derivatives of double-four-ring silicate as novel building blocks of silica-based materials. Chemistry of Materials, **20**, 1147–1153 (2008).
DOI: 10.1021/cm0716194

[16] Hasegawa I.: Building block approach to organic/silica hybrid materials. Journal of Sol-Gel Science and Technology, **5**, 93–100 (1995).
DOI: 10.1007/BF00487725

[17] Ho K. Y., McKay G., Yeung K. L.: Selective adsorbents from ordered mesoporous silica. Langmuir, **19**, 3019–3024 (2003).
DOI: 10.1021/la0267084

[18] Suzuki N., Kiba S., Yamauchi Y.: Low dielectric property of novel mesoporous silica/polymer composites using smart molecular caps: Theoretical calculation of air space encapsulated inside mesopores. Microporous and Mesoporous Materials, **138**, 123–131 (2011).
DOI: 10.1016/j.micromeso.2010.09.020

[19] Gouri C., Reghunadhan Nair C. P., Ramaswamy R.: Reactive Alder-ene blend of diallyl bisphenol A novolac and bisphenol A bismaleimide: Synthesis, cure and adhesion studies. Polymer International, **50**, 403–413 (2001).
DOI: 10.1002/pi.644

[20] Gu A. J., Liang G. Z.: High performance bismaleimide resins modified by novel allyl compounds based on epoxy resins. Polymer-Plastics Technology and Engineering, **36**, 681–694 (1997).
DOI: 10.1080/03602559708000654

[21] Rozenberg B. A., Dzhavadyan E. A., Morgan R., Shin E.: High-performance bismaleimide matrices: Cure kinetics and mechanism. Polymers for Advanced Technologies, **13**, 837–844 (2002).
DOI: 10.1002/pat.230

[22] Liang K. W., Toghiani H., Li G. Z., Pittman Jr C. U.: Synthesis, morphology, and viscoelastic properties of cyanate ester/polyhedral oligomeric silsesquioxane nanocomposites. Journal of Polymer Science Part A: Polymer Chemistry, **43**, 3887–3898 (2005).
DOI: 10.1002/pola.20861

[23] Kimura H., Matsumoto A., Sugito H., Hasegawa K., Ohtsuka K., Fukuda A.: New thermosetting resin from poly(p-vinylphenol) based benzoxazine and epoxy resin. Journal Applied Polymer Science, **79**, 555–565 (2001).
DOI: 10.1002/1097-4628(20010118)79:3<555::AID-APP190>3.0.CO;2-H

[24] Song H. C.: Polymer composites. Beijing University of Aeronautics and Astronautics Press, Beijing (1985).

[25] Lin J. J., Wang X. D.: Novel low-κ polyimide/mesoporous silica composite films: Preparation, microstructure, and properties. Polymer, **48**, 318–329 (2007).
DOI: 10.1016/j.polymer.2006.10.037

[26] Liang K. W., Li G. Z., Toghiani H., Koo J. H., Pittman Jr C. U.: Cyanate ester/polyhedral oligomeric silsesquioxane (POSS) nanocomposites: Synthesis and characterization. Chemistry of Materials, **18**, 301–312 (2006).
DOI: 10.1021/cm051582s

[27] Li G. Z., Wang L. C., Toghiani H., Daulton T. L., Koyama K., Pittman Jr C. U.: Viscoelastic and mechanical properties of epoxy/multifunctional polyhedral oligomeric silsesquioxane nanocomposites and epoxy/ladderlike polyphenylsilsesquioxane blend. Macromolecules, **34**, 8686–8693 (2001).
DOI: 10.1021/ma011117q

[28] Rashid E. S. A., Ariffin K., Kooi C. C., Akil H. M.: Preparation and properties of POSS/epoxy composites for electronic packaging applications. Material and Design, **30**, 1–8 (2009).
DOI: 10.1016/j.matdes.2008.04.065

[29] Karthikeyan C. S., Sankaran S., Kishore: Investigation of bending modulus of fiber-reinforced syntactic foams for sandwich and structural applications. Polymers for Advanced Technologies, **18**, 254–256 (2007).
DOI: 10.1002/pat.828

[30] Li A., Pan Y. Z., Shen X. W., Lu H. B., Yang Y. L.: Rod-like attapulgite/polyimide nanocomposites with simultaneously improved strength, toughness, thermal stability and related mechanisms. Journal of Materials Chemistry, **18**, 4928–4941 (2008).
DOI: 10.1039/B805849K

[31] Starr F. W., Douglas J. F., Glotzer S. C.: Origin of particle clustering in a simulated polymer nanocomposite and its impact on rheology. The Journal of Chemical Physics, **119**, 1777–1789 (2003).
DOI: 10.1063/1.1580099

[32] Pan Y. Z., Xu Y., Li A., Lu H. B., Yang Y. L., Chen W., Nutt S.: Hybrid network structure and mechanical properties of rodlike silicate/cyanate ester nanocomposites. Macromolecules, **41**, 9245–9258 (2008).
DOI: 10.1021/ma800819s

[33] Johnsen B. B., Kinloch A. J., Mohammed R. D., Taylor A. C., Sprenger S.: Toughening mechanisms of nanoparticle-modified epoxy polymers. Polymer, **48**, 530–541 (2007).
DOI: 10.1016/j.polymer.2006.11.038

[34] Ling W., Gu A. J., Liang G. Z., Yuan L., Liu J.: Dynamic mechanical properties of aluminum nitride/cyanate ester composites for high performance electronic packaging. Polymers for Advanced Technologies, **21**, 365–370 (2010).
DOI: 10.1002/pat.1436

[35] Omrani A., Afsar S., Safarpour M. A.: Thermoset nanocomposites using hybrid nano TiO_2–SiO_2. Materials Chemistry and Physics, **122**, 343–349 (2010).
DOI: 10.1016/j.matchemphys.2010.02.073

[36] Malini K. A., Mohammed E. M., Sindhu S., Joy P. A., Date S. K., Kulkarni S. D., Kurian P., Anantharaman M. R.: Magnetic and processability studies on rubber ferrite composites based on natural rubber and mixed ferrite. Materials Science, **36**, 5551–5557 (2001).
DOI: 10.1023/A:1012545127918

[37] Hu G. J., Hong X. K., Sun J. L., Chen J., Chu J. H., Zhu D-M., Dai N.: Peculiar ferroelectric and dielectric properties of quasiperiodic $PbZr_{0.4}$ $Ti_{0.6}O_3$ multilayers. New Journal Physics, **8**, 316–324 (2006).
DOI: 10.1088/1367-2630/8/12/316

[38] Stephen M. A., Granick S.: Image analysis with rapid and accurate two-dimensional Gaussian fitting. Langmuir, **25**, 8152–8160 (2009).
DOI: 10.1021/la900393v

[39] Zhang Z. P., Gu A. J., Liang G. Z., Ren P. G., Xie J. Q., Wang X. L.: Thermo-oxygen degradation mechanisms of POSS/epoxy nanocomposites. Polymer Degradation and Stability, **92**, 1986–1993 (2007).
DOI: 10.1016/j.polymdegradstab.2007.08.004

[40] Rittigstein P., Priestley R. D., Broadbelt L. J., Torkelson J. M.: Model polymer nanocomposites provide an understanding of confinement effects in real nanocomposites. Nature Materials, **6**, 278–282 (2007).
DOI: 10.1038/nmat1870